IN-SITU FORMATION OF BIODEGRADABLE POLYHYDROXYBUTYRATE POLYMER FOR TARGETED OCCLUSION OF SOLID TUMOR NEOVASCULATURE

A Dissertation
Presented to the Faculty of the Graduate School
Of Cornell University
In Partial Fulfillment of the Requirements for the Degree of
Doctor of Philosophy

by
Stephanie Ann Parker
August 2015

COPYRIGHT PAGE

ABSTRACT

IN-SITU FORMATION OF BIODEGRADABLE POLYHYDROXYBUTYRATE POLYMER FOR TARGETED OCCLUSION OF SOLID TUMOR NEOVASCULATURE

Stephanie Ann Parker, Ph. D.

Cornell University 2015

The objective of this work was to develop a novel dual-modal protein for targeted vascular occlusion of solid tumor neovasculature mediated by in-situ polymer synthesis. Towards this aim two novel constructs were designed; a single-chain variable fragment (ScFv), J591 ScFv, that recognizes an extracellular epitope the tumor neovasculature endothelial marker Prostate Specific Membrane Antigen (PSMA) and a fusion protein composed of the J591 ScFv and the polyhydroxyalkanoate (PHA) synthase enzyme, the sole enzyme required to initiate synthesis of the biocompatible polyhydroxybutyrate (PHB) polymer by conversion of (R)-3-hydroxyacyl-CoA thioester (3HB-CoA) substrate to PHB. The dual moiety fusion protein was designed to localize to the solid tumor neovasculature by targeting PSMA via the J591 ScFv. Next, 3HB-CoA monomer substrate will be locally delivered and vascular occlusion will be mediated via in situ growth of PHB polymer catalyzed by the PHA synthase enzyme moiety of the fusion protein. The resulting obstruction of the tumor neovasculature due to PHB polymer accumulation will restrict the blood supply to the tumor, causing in tissue ischemia and tumor necrosis. Further, conjugating the fusion protein with superparamagnetic iron oxide nanoparticles (SPIONs) allows for monitoring via Magnetic resonance imaging (MRI) and potentially provides a means increasing the valency of the fusion protein.

The following chapters detail the design, production, and characterization of the J591 ScFv and J591 ScFv-PHA Synthase proteins. Construction of the J591 ScFv was based on the reported

complementarity-determining region (CDR) of the PSMA specific J591 monoclonal antibody (mAb). The nucleotide sequence encoding the J591-derived ScFv was codon-optimized for expression in *P. pastoris* and a 6X his-tag was added to facilitate affinity purification. The J591 ScFv showed binding affinity and specificity to cell extracts containing PSMA and PSMA-expressing prostate cancer cells. The J591ScFv –PHA Synthase fusion protein was expressed in *Pichia pastoris*. The addition of a linker between the J591 ScFv and PHA Synthase proteins was determined critical to maintain functionality of the ScFv. Our results demonstrate that our J591 ScFv-PHA synthase fusion protein construct is functional and can be produced in *P. pastoris* for use in diagnostic and targeted therapeutic applications.

BIOGRAPHICAL SKETCH

Stephanie Ann Parker grew up in Southern California and attended Eisenhower High School in Rialto, California before beginning her undergraduate studies in Mechanical Engineering at the University of Southern California. The summer before her senior year of undergraduate studies Stephanie was awarded a fellowship sponsored by the National Science Foundation to conduct research at Cornell University with the Nanobiotechnology Center. During that summer Dr. Carl A. Batt, mentored Stephanie in his lab, where she later completed her doctoral studies. This was Stephanie's first introduction to Biomedical Engineering research, particularly nanotechnology for targeted cancer therapeutics, and heavily motivated her decision to continue her education in graduate school.

After earning a Bachelor's of Science Degree Stephanie continued her education earning a Master's of Science degree in Mechanical Engineering from the University of Southern California, Los Angeles, CA while working part-time as a Mechanical Engineering. Following earning her Master's degree she was awarded the Research Internship in Science and Engineering (RISE) professional award administered by The German Academic Exchange Service (DAAD).

Following completion of her internship in the Heat Exchangers group at BASF the Chemical company in Ludwigshafen, Germany, Stephanie then continued her education at Cornell University, Ithaca NY pursuing a doctoral degree in Biomedical Engineering. At Cornell Stephanie joined Carl A. Batt's research group and began working on her thesis research area of targeted cancer therapeutics and developing strategies for high yield protein production.

ACKNOWLEDGEMENTS

I greatly appreciate the guidance and support of my thesis advisor Dr. Carl A. Batt who has provided me with invaluable mentorship for the past ten years and counting. I would like to acknowledge my minor committee members Dr. Neil Bander and Dr. Lawrence Bonassar for their valuable feedback. I am especially indebted to the other members of the Batt lab, who provided me with essential mentorship. I greatly enjoyed getting to know everyone and having the opportunity to collaborate on new and exciting projects.

I have been extremely fortunate to have friends and family who have been very encouraging and supportive during my journey. My close friends have all offered kind words and continued to motivate me during my time away at Cornell. Thank you to Nizeet Aguilar for her support and friendship, as we made through the PhD program together. Special thank you to Cameron Bardliving for being my rock through this journey. My family has been there from the beginning providing immeasurable love and strength. I would like to thank my Uncle Bill who has been a big source of inspiration. Thank you to my Grandmother, for motivating and inspiring me to work towards my goals. Thank you to my Brother who has being there to cheer me on in all my endeavors. I want to especially thank my Mother for providing the foundation for my success and always encouraging my ambitions.

TABLE OF CONTENTS

LIST OF FIGURES

LIST OF TABLES

LIST OF ABBREVIATIONS

AuNPs: Gold Nanoparticles
SPIONs: Superparamagnetic Iron Oxide Nanoparticles
IONPs: Iron Oxide Nanoparticles
HNPs: Gold and Iron oxide Hybrid Nanoparticles
ScFv: Single Chain Variable Fragment

CHAPTER 1 Gold and iron oxide Nanoparticles with Antibody Guides to Find and Destroy Cancer Cells

Reprinted from, Encyclopedia of Molecular Cell Biology and Molecular Medicine, **Stephanie A. Parker**, Isabel A. Soto, Dickson K. Kirui, Cameron L. Bardliving, Carl A. Batt, Gold and iron oxide Nanoparticles with Antibody Guides to Find and Destroy Cancer Cells with permission from Wiley

1.1 Summary

Nanoparticles represent an increasingly important field of theranostic agents that can not only sense but also treat disease. Gold (AuNP) and iron oxide nanoparticles (IONP) functionalized with antibodies (Abs) specific to tumor antigens can detect and treat cancer at the cellular level. These particles are being investigated for clinical applications including imaging contrast, thermal tumor therapy, drug delivery, and radiosensitizing agents. This review will cover the unique properties of these particles which when combined with targeting moieties make them suitable for cancer imaging and therapeutics, as evidenced by the recent preclinical, *in vivo* and *in vitro* studies, conducted with AuNP and IONP Ab conjugates (Figure 1.1).

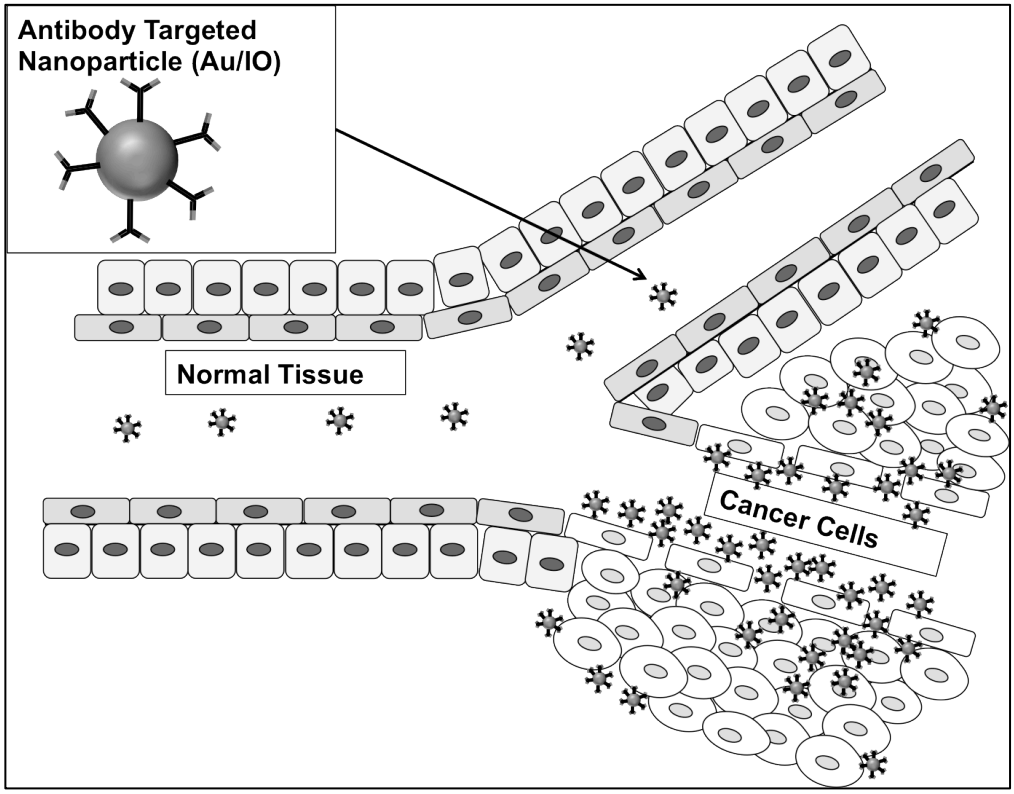

Figure 1.1 Antibody targeted gold (Au)/iron oxide (IO)/Hybrid nanoparticles moving through vascular system of the body to selectively search for and destroy cancerous cells.
Normal cells are portrayed as rectangles while cancer cells are portrayed as oval. Antibody targeted nanoparticles are able to penetrate the endothelial layer and antibodies on the particles

bind to tumor specific antigens on the cancer cells, resulting in the accumulation of nanoparticles at the site of disease.

1.2 Introduction

Despite significant advances in cancer research, treatment, and diagnosis over past two decades, cancer remains a major health problem in the United States and many other parts of the world. Cancer is the second a leading cause of death in the U.S., accounting for 23% of all deaths in 2009, and the leading cause of death for both men and women ages 40 to 79 years [1, 2]. The current standard treatment strategies include surgical resection, chemotherapy and radiotherapy, which are indiscriminate and unnecessarily lead to damage of healthy tissue. Limitations of treatments such as chemotherapy and radiotherapy, can be attributed to resistance to chemotherapeutics [3], physiological barriers, and poor bioavailability [3, 4]. Advances in nanomedicine have lead to the development of immunotargeted nanomaterials, which have the potential to address the limitations of conventional cancer therapeutics by targeting cancer at the cellular level. Gold (AuNPs) and iron oxide (IO) nanoparticles with antibody conjugates are of particular interest for cancer theranostic applications. AuNPs and IONPs possess unique optical and magnetic properties that can be exploited for simultaneous diagnostic, imaging and therapy, including thermal and controlled drug release for cancer therapy [5] (Figure 1.2). Recent *in vitro* and *in vivo* studies conducted with immunotargeted nanoparticles have demonstrated that they exhibit target specificity, improved pharmacokinetics and can deliver drugs via penetration of the leaky tumor vasculature [6].

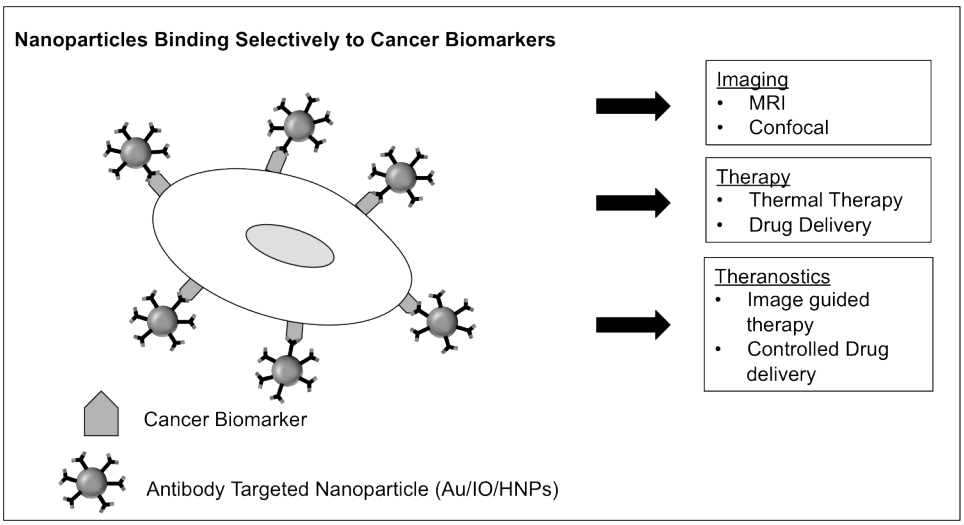

Figure 1.2 Antibody Targeted Nanoparticles Gold (Au), Iron Oxide (IO), Hybrid (Au and IO) Nanoparticles binding selectively to cancer biomarkers located on the surface of a cancer cell. *This selective and specific binding and the unique optical and magnetic properties of the NPs allows for dual imaging and therapy of cancer cells.*

This review will first cover the synthesis and composition of AuNPs, IONPs, and hybrid Au and IO nanoparticles (HNPs) as well as the clinically relevant properties of these nanomaterials. Subsequently, we will give an overview of the functionalization strategies used to couple nanoparticles with cancer targeting antibodies and cover some of the targeting moieties currently available. Then we will examine preclinical studies focused on the development of antibody conjugated AuNPs, IONPs, and HNPs for cancer imaging and therapeutics including; hyperthermia, targeted drug delivery, and radiation therapy.

1.3 Composition

AuNPs, IONPs, and HNPs have been extensively studied and synthesized using a number of methods for use in biomedical applications. The unique characteristics of nanoparticles that have spurred interest in them for clinical applications include: (a) large surface to volume ratio, (b) physical and chemical properties that can be tuned depending on size, composition, and shape, (c) enhanced penetration and preferential accumulation in tumor tissue, (d) high absorption band in the near-infrared (NIR) region [7], and (e) ease of surface functionalization with biomolecules

[8]. Additionally, the nanoscale dimensions of nanoparticles make them suited for targeting cancer at the cellular level [9].

1.3.1 Gold Nanoparticles

The most common method used for AuNP synthesis are chemical or electrochemical reduction of a gold (III) precursor [10]. A variety of shapes and structures can be synthesized, the most prevalent AuNP structures include: nanorods, nanospheres, nanoshells, and composite particles where gold is combined with other elements including silica and iron (see below HNPs Section) [10]. The geometry and composition of AuNPs affects their optical properties, including absorption wavelength, [11] and interactions with biological molecules, including enzyme catalysis [12]. AuNPs can therefore be tuned for specific imaging and thermal therapy applications; the reviews listed here describe the varying properties in more detail [11, 13-15].

AuNPs possess several unique properties that make them attractive for clinical applications, including an easily modified surface chemistry and size dependent electrical and optical properties [16-18]. AuNPs possess intense surface plasmon-resonance (SPR) scattering, which results in an enhanced electromagnetic field at the nanoparticle surface. [19]. Scattered-light from AuNPs can be detected under and used for dark field microscopy and confocal microscopy imaging applications [20-22]. Additionally, due to their high atomic mass, Au nanoparticles absorb significantly more X-ray radiation than soft tissue cells. AuNPs can thus be used to enhance cancer radiation therapy and increase contrast in diagnostic Computed Tomography (CT) Scans [23].

1.3.2 Iron Oxide Nanoparticles

IONPs can be synthesized with precise size, morphology, surface treatment, and magnetic properties [24, 25]. Common methods of synthesis include co-precipitation, micro emulsions,

and high temperature decomposition of organic precursors [25]. Maghemite (Fe_2O_3) and magnetite (Fe_3O_4) iron oxide can be prepared as monodispered surface derivatized nanoparticles [24, 26]. Ferric magnetic materials such as iron oxide also possess unique paramagnetic properties. When the size domain of the nanoparticle is reduced below that of a single magnetic domain [27] the magnetic properties are altered, resulting in superparamagnetic behavior [25]. IONPs with a core diameter of less than 20 nm exhibit superparamagnetic properties at room temperature and are superparamagnetic iron oxide nanoparticles (SPIONs).

SPIONs have a significant ability to reduce the Magnetic Resonance Imaging (MRI) signal thus acting as negative contrast agents and causing darkening of the MR image [28]. SPIO agents, ferumoxides (Feridex IV, Berlex Laboratories. Inc. in the USA and Endorem, Guerbet S.A in Europe), have been approved for clinical applications in the USA [29]. Feridex SPIONs are approved for intravenous administration and have been used as contrast agents to identify liver tumors [30]. Theses superparamagnetic iron oxide nanoparticles (SPIONs) are attractive platforms for targeted drug delivery, magnetic hyperthermia, immunotherapy, tumor visualization, and detection of circulating tumor cells [31]. Preclinical studies in animal models have shown that antibody-conjugated SPIONs retain specificity for antigen-expressing tissues and are effective contrast enhancing agents for MRI.

1.3.3 Hybrid Nanoparticles

The potential benefits of integrating nanomaterials with disparate properties (i.e. magnetism and energy absorption) into HNPs have spurred interest in the development of various synthetic strategies. HNPs retain the optical and magnetic properties of AuNPs and IONPs respectfully [32-36] and can be fabricated by aqueous phase [37] and high temperature organic phase thermal decomposition of respective precursors [37-40]. The addition of an Au coating to IONPs has

been reported to enhance chemical stability by protecting the core from oxidation and corrosion [41, 42]. HNPs with Au cores encapsulated within hollow iron oxide shells and Au decorated with iron oxide have been developed for dual imaging, MRI and X-ray detection, [43] and multifunctional imaging and thermal applications respectively [42, 44, 45].

1.4 Nanoparticle Surface Functionalization

Several strategies have been employed to functionalize AuNPs and IONPs with targeting moieties i.e. cancer specific antibodies. A successful functionalization strategy will not alter the desired properties of the NPs and preserve of the targeting ability of the immobilized antibodies. First NPs must be adequately coated, as bare or surfactant-stabilized AuNPs and IONPs are unstable and cytotoxic in physiological conditions [46-48]. These unmodified nanoparticles are also prone to aggregation and would be rapidly cleared from the body by the reticuloendothelial clearance system (RES) [49]. This shortened blood half-life reduces the efficacy of AuNP and IONP-based theranostic platforms, where longer circulation time increases the probability that particles can find, attach and accumulate in targeted cancer cells.

Fortunately, facile chemistries provide methods to stabilize the nanoparticles and conjugate antibodies to their surface [50]. The most common methods for nanoparticle functionalization include ligand exchange [51-64], coating with amphiphilic polymers [65-78], coating with silica [79-83], and polymer coating, and encapsulation [84-87] (Figure 1.3) [88]. Following surface coating, AuNPs and IONPs have been shown to retain the desired relativities, biocompatibility properties, native optical properties, and can easily be additionally functionalized with biomolecules, i.e. monoclonal antibodies (mAb) and single chain antibodies (ScFv) [89].

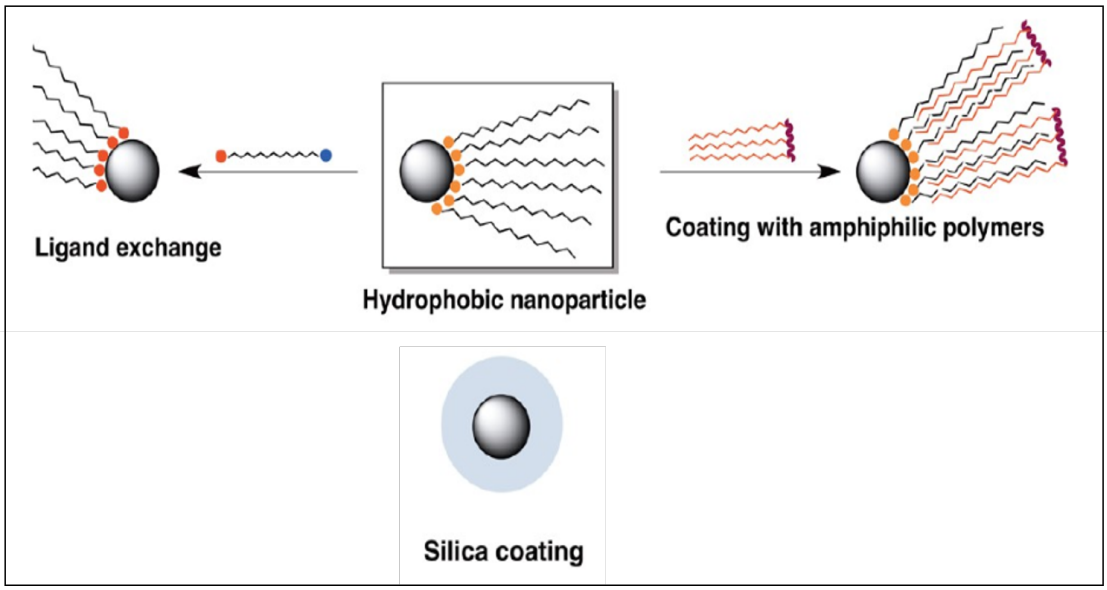

Figure 1.3 Primary coating strategies for engineering the surfaces of nanoparticles. *Depicted above: Ligand exchange, hydrophobic interactions, coating with amphiphilic polymers, and silica coating. Reprinted with permission from Fratila, R. M., S. G. Mitchell, et al. "Strategies for the Biofunctionalization of Gold and Iron Oxide Nanoparticles." Langmuir. Copyright 2014 American Chemical Society [88].*

1.4.1 Antibody Immobilization and Orientation on Nanoparticles

Following stabilization coating, nanoparticles can then be functionalized with antibodies for targeted cancer therapeutic applications. There are five classes of antibodies with immunoglobulin G (IgG) being the most abundant in human serum, thus the most widely used for biomedical applications[88]. Monoclonal antibodies (mAb) consist of four polypeptide chains with a molecular weight of 150 kDa, which complicates their conjugation to nanoparticles due to their large size. Smaller Ab fragments including single chain variable fragments (ScFv) and fragment antigen binding (Fab) antibodies have been investigated in preclinical studies for tumor targeting nanoparticle treatment applications. Strategies used to functional nanoparticles with Abs include: i) physical adsorption [90], ii) covalent binding via amine groups or carbohydrate groups on Ab [91], iii) use of adapter biomolecules (streptavidin-biotin, Protein G); and v) ionic adsorption. However, a drawback to streptavaidin-biotin is that streptavidin is a

bacterial protein without a mammalian analog and may cause an immunogenic response in patients [92, 93]. The selection of coupling method depends on the type and amount of functional groups present on the surface-coating layer of the nanoparticles.

It is also important to note that immobilization of biologically active molecules requires proper steric availability of the active binding sites to avoid reducing or completely eliminating binding capacity. The orientation of Abs on the nanoparticle surface must be such that antigen-binding sites are well exposed without compromising the function of the protein. Steric hindrance of antigen-recognition sites due to randomly oriented Abs can result in 100-fold decrease in binding affinity [94]. End-on or flat-on orientation have been found to yield higher antigen binding capacities compared to random (head on and sideways) orientations [88]. Typically, to retain full biological activity of the immobilized antibody, the recognition sites, the Fab regions should be oriented away from surface of the nanoparticle. Directed immobilization of antibody fragments, Fabs and ScFvs, has been achieved via the addition of functionalities to the terminal regions of ScFv [95] and Fabs [96]. Also, modification of the internal linker regions of ScFvs have been reported for site-specific immobilization on the surface of nanoparticles [97].

1.4.2 Cancer Targeting Antibodies

Tumor stromal and vascular endothelial cells express specific antigens that distinguish them from normal tissue [98]. Identification of these antigens has led to the clinical development of therapeutic monoclonal antibodies (mAbs) that recognize cancer cells as compared with normal tissue [99, 100]. These cancer antigen specific antibodies are among the most successful targeted cancer therapeutic strategies for patients with hematological malignancies and solid tumors [98, 101, 102]. There are currently 15 unmodified antibodies approved by the Food and Drug Administration for cancer therapy [103]. Tumor associated antigens recognized by therapeutic

antibodies are cell surface differentiation antigens. Hematopoietic differentiation antigens are generally associated with antibodies that target cluster of differentiation (CD) groups; including CD20, CD20, CD33, and CD52. Other cell surface antigens are glycoproteins and carbohydrates found on the surface of both normal and tumor cells, but are overexpressed in tumor cell populations. Table 1.1 outlines the unmodified monoclonal antibodies currently approved for solid tumor and hematological malignancies.

FDA Approved Monoclonal Antibodies			
Therapeutic Antibody	**Target**	**FDA Approved Indication**	**Mechanism of action**
Solid Tumor Malignancies			
Trastuzumab (Herceptin; Genentech); Humanized IgG1	HER2/ neu	• HER2-overexpressing Breast Cancer • HER2-overexpressing Metastatic Gastric or Gastroesophageal junction Adenocarcinoma	Inhibition of HER2/neu signaling and ADCC
Cetuximab (Erbitux; Bristol-Myers Squibb); Chimeric human-murine IgG1	EGFR	• Colorectal Cancer that has metastasized • Squamous cell carcinoma of the head and neck	Inhibition of EGFR signaling and ADCC
Bevacizumab (Avastin; Genetech/ Roche); Humanized IgG1	VEGF	• Colorectal Cancer that has metastasized • Glioblastoma in patients not responding to other treatments • Non-small cell lung that is locally advance, cannot be surgically removed, has metastasized, or has recurred. • Renal cell cancer that has metastasized.	Inhibition of VEGF signaling
Panitumumab (Vectibix; Amgen); Human IgG2	EGFR	• Colorectal cancer (certain types) in patients whose disease has not responded with other chemotherapy and has metastasized.	Inhibition of EGFR signaling
Ipilimumab (Yervoy; Bristol-Myers Squibb); IgG1	CTLA 4	• Melanoma that cannot be surgically removed or has metastasized.	Inhibition of CTLA4 signaling
Pertuzumab (Perjeta; Genentech); Humanized IgG1	HER2/ neu	• Neoadjuvant treatment of HER2 positive breast cancer in combination with trastuzumab and docetaxel (chemotherapeutic). • HER2-overexpressing metastatic Breast Cancer.	Inhibition of HER2/neu signaling
Hematological malignancies			
Rituximab (Mabthera; Roche); Chimeric human-murine IgG1	CD20	• For treatment of CD20-positive B-cell non-Hodgkin's Lymphoma CLL.	ADCC, induction of apoptosis and CDC
Alemtuzumab (Campath; Genzyme); Humanized IgG1	CD52	• Approved for single agent treatment of B-cell CLL.	Induction of apoptosis and CDC
Ofatumumab (Arzerra; Genmab); Human IgG1	CD20	• For treatment of patients with CLL no longer controlled by other forms of chemotherapy.	ADCC and CDC
Obinutuzumab (Gazya; Genetech/ Roche); Humanized IgG1	CD20	• For patients with previously untreated CLL	ADCC and CDC

Table 1.1 FDA Approved Unmodified Monoclonal Antibodies for Solid Tumor and Hematological Malignancies.

Abbreviations: Antibody-dependent cellular cytotoxicity (ADCC), and complement-dependent cytotoxicity (CDC), chronic lymphocytic leukemia (CLL).

ScFv, Ab fragments, have also been explored for use as targeting ligands for cancer therapeutics [104, 105]. ScFvs are recombinant proteins generated from monoclonal antibodies. ScFv fragments contain the highly specific variable domains of monoclonal antibodies, however are smaller in size. Cancer targeting ScFvs conjugated to nanoparticles have been used for site-specific therapeutic delivery and imaging [106]. This reduction in size also facilitates direct and dense immobilization of the antibodies on the surface of nanoparticles [107].

1.5 Au and IONP with Antibody Conjugates for Cancer Imaging and Detection

The first step in the process of treating cancer with an antibody conjugated Au and IONPs is to find the cancer. Immunotargeted Au and IONPs are particularly of interest as these nanoparticles, selectively targeted to diseased sites, increase signal to noise ratio of traditional imaging technologies making it possible to visualize antigen-expressing cancer cells [108]. The ability to image cancer at the cellular level would provide a significant improvement over traditional methods by helping to diagnose cancers earlier than is currently feasible with unaided imaging techniques.

The current standard optical technologies for cancer detection are optical coherence tomography (OCT) and reflectance confocal microscopy (RCM). These technologies image micro-anatomical features of diseased tissue and cannot distinguish cancers based specifically on molecular biomarkers associated with carcinogenesis [109]. The image is generated via reflected light from the endogenous chromophores present in the tissue [110]. The resulting optical signal is weak and results in poor intracellular contrast and subtle spectral differences between malignant and benign cells. To overcome these limitations, exogenous chemicals have been explored to function as contrast agents. However, organic dyes are subject to rapid photo-

bleaching, biological and chemical degradation, and their signal quickly decreases upon exposure to excitation light source [111, 112].

AuNPs, IONPs, and HNPs would be an improvement over dyes as they are photo-stable [113, 114] and can be carry fluorescent dyes for Near-infrared imaging (NIR) [112, 115]. Preclinical studies have employed several imaging techniques to examine the capacity of antibody conjugated Au, IO, and HNPs for cancer imaging including: NIR, confocal reflectance[116], dark field, optoacoustic [117], X-ray microtomography (Micro CT)[118], optical coherence tomography (OCT) [119], and MRI [76, 120] contrast agents [121]. Table 1.2 outlines some recent antibody targeted imaging studies conducted with Au, IO, and HNPs. The objective of preclinical studies has been to demonstrate the selectivity and quantify the improved imaging as a result of using antibody conjugated NPs, demonstrating feasibility for clinical studies. The following are highlights from recent *in vivo* imaging studies with Au and IONPs conjugated with cancer targeting antibodies. The variety of targeting agents and the subsequent imaging modalities shows the robust nature of the approach for the detection of a variety of cancers.

Gold and Iron Oxide Antibody Conjugate Cancer Imaging Studies			
Nanoparticle Type	**Cancer Type(s)**	**Antibody Conjugate**	**Imaging Technique**
AuNPs, AuNRs	Lung Cancer, Solid Tumor Malignancies	Anti-EGFR	Confocal [122] Dark Field Microscopy [123]
AuNRs	Breast Cancer	Herceptin (Anti-HER2/neu)	Micro CT [118]
AuNRs	Prostate Cancer	Anti-PSMA	Optoacoustic imaging [117]
AuNPs	Colorectal Cancer	anti-β-catenin and anti-E-cadherin	Confocal [110]
AuNPs, HNPs	Solid Tumor Malignancies	Anti-CD105	PET Imaging [18] MRI [76]
IONPs	Breast Cancer	Anti-HER2/neu,	MRI [19, 124]

Table 1.2 Cancer imaging studies conducted with antibody functionalized gold and iron oxide nanoparticles.
Abbreviations: Gold Nanoparticles (AuNPs), Gold Nanorods (AuNRs), Hollow Gold Nanospheres (HAuNSs), Iron Oxide Nanoparticles (IONPs), Magnetic Resonance Imaging (MRI), X-ray microtomography (Micro CT), and Positron Emission Tomography (PET) imaging.

1.5.1 Imaging Studies

Specific examples of imaging studies using antibody-directed nanoparticles demonstrate the utility of the approach. For example, in a recent study by Karmani et. al., AuNPs conjugated with the anti-CD105 mAb, specific to tumor angiogenesis and tumor progression, were investigated for theranostic, dual imaging and therapeutic applications in an *in vivo* mouse model [125]. The antibodies were radiolabeled labeled with ^{89}Zr to facilitate PET imaging before conjugation to 5 nm AuNPs. Male mice bearing melanoma xenografts where intravenously injected with the radio-labeled antibody conjugated AuNPs, as well as radiolabeled CD-105 antibody alone and non-targeted AuNPs for comparison. Whole-body PET images and inductively coupled plasma mass spectrometry (ICP-MS) analysis of blood and tumors where used to assess *in vivo* distribution of the NPs. High tumor contrast and selective tumor targeting

were observed with the immunotageted AuNPs, as compared to the antibody-target radio-isotope alone or the non-targeted AuNPs. The major finding of this study was that conjugation of the anti-CD105 antibody with AuNPs did not inhibit tumor uptake or efficacy of tumor targeting of the antibody.

In another recent study, nanoparticles targeting HER2/neu demonstrated effective MRI imaging of HER2 expressing cells in xenograft mice [126], shown in FIGURE 1.4. In this study, SPIONs were first surface modified with dextran, followed by the addition of primary amine functional groups, and then functionalized with Herceptin in the presence of coupling agents. Targeting of the Herceptin-SPIONs to HER2/neu receptor positive breast cancer cell lines was detected via *in vitro* and *in vivo* MRI. *In vitro* MRI signal enhancement increased proportionally as a function of the relative HER2/neu expression level. For *in vivo* studies the Herceptin-SPIONs were administered intravenously to tumor-bearing mice prepared by subcutaneous injection of KB cells (human nasopharyngeal epidermal carcinoma cells lacking HER2/neu receptors) and SKBR-3 (HER2/neu expressing breast cancer) cells. The tumor site was detected via T2-weighted MRI and administration of the Herceptin-SPIONs produced a 45% enhancement drop in the HER2/neu positive tumor compared with the control, indicating a high level of accumulation within the tumor, Figure 1.4. Results of this study demonstrate the potential of SPIONs to be used as MRI contrast agents for the detection of HER2/neu-expressing breast cancer.

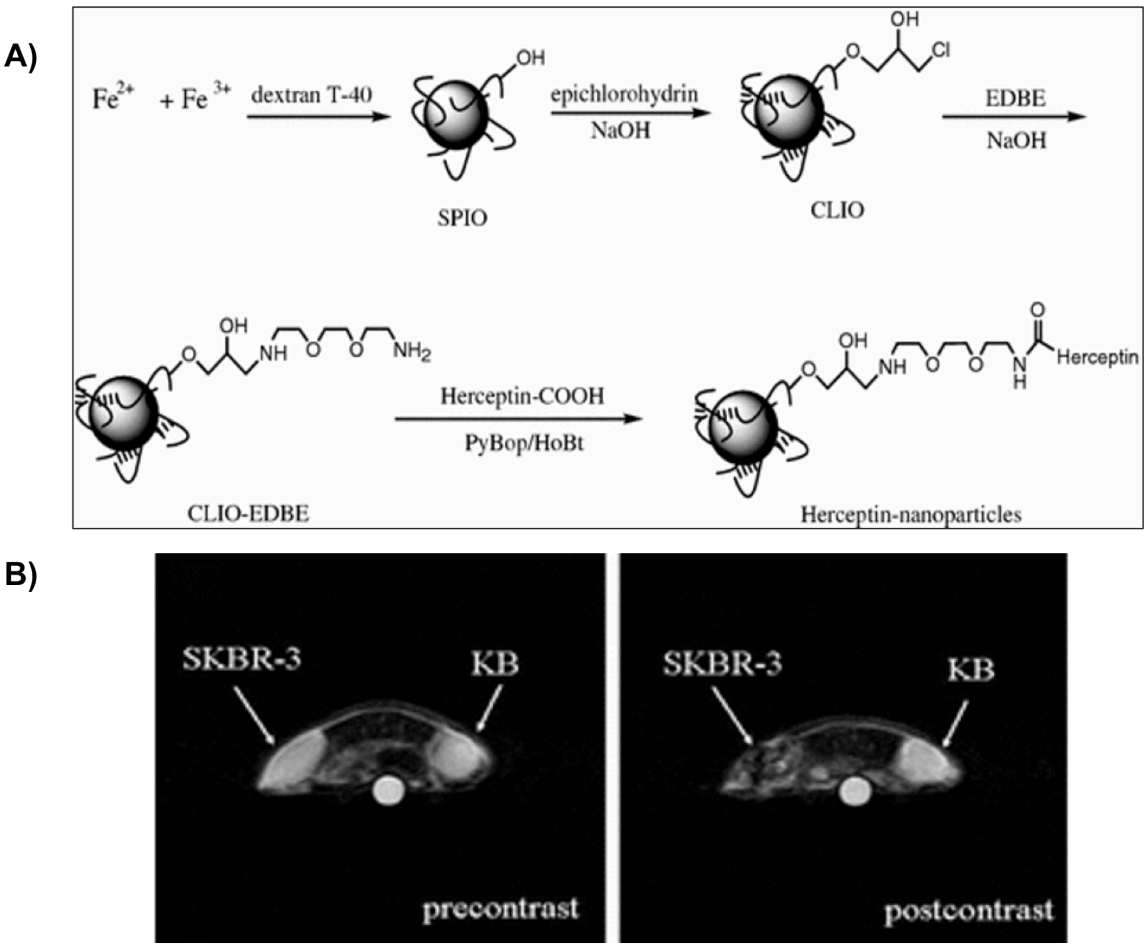

Figure 1.4 SPION Conjugation Scheme and Enhanced MRI Images.
A: The synthetic scheme of Herceptin-nanoparticles. SPIO Superparamagnetic iron oxide, CLIO cross-linked iron oxide, 2,2'-(ethylenedioxy)bisethylamine, PyBop (benzotriazol-1-yloxy) tripyrrolidinophosphonium hexafluorophosphate, HoBt 1-hydroxybenzotriazole. B: T_2-weighted MRI before (left) and after (right) injection of Herceptin-Iron Oxide Nanoparticles. The cell lines used here are SKBR-3 HER2/neu expressing breast cancer cells and KB non-HER2/neu expressing epidermal carcinoma cells. Reprinted from Journal of Biological Inorganic Chemistry, Chen, T. J. et. al. "Targeted Herceptin–dextran iron oxide nanoparticles for noninvasive imaging of HER2/neu receptors using MRI," Copyright 2009, with permission from Wiley.

1.6 Antibody Conjugated Au and IONPs for Cancer Therapeutics

NPs can serve as theranostic agents allowing the clinician to initially image and diagnose the cancer then follow-up with a target specific therapy. The advantage is the simplicity of the coupled approach and ability to initiate treatment only when the diagnostic indicates the need for treatment. Therapeutic strategies for the treatment of cancers employing antibody conjugated

AuNPs and IONPs include hyperthermia, targeted drug delivery, and enhancement of radiation therapies. These therapeutic methods can be combined with imaging modalities for theranostics; including image-guided hyperthermia and drug delivery. The advantage of the theranostic approach would be that before administration of therapeutics, a physician would be able to track the particles and direct treatment at the site of disease. This technology presents a powerful tool that could be used to discover cancer cells and provide treatment immediately, in a potential combined screening and treatment strategy. This section provides a brief overview of recent developments in the area of AuNPs and IONPs for cancer therapeutics.

1.6.1 Targeted Hyperthermia

One example of a targeted therapeutic approach that utilizes NPs is the exogenous application of energy, which is then concentrated by the NPs resulting in a region-specific increase in temperature and hyperthermia. Hyperthermia is the elevation of temperature up to 42-46°C, usually by photon flux of 5-48 W/cm^2[127], for an extended period of time to damage and kill cancer cells cancer cells by DNA denaturation [128-130]. Hyperthermia has been widely used for cancer treatment [131] to enhances cancer treatment by directly causing cell death, sensitizing cells to chemotherapy [127] and radiotherapy [132] by promoting tumor reoxygenation [133, 134]. Major technical impedances of traditional hyperthermia treatment are difficulty of heating the local tumor region without damaging normal tissue [135] and inability to create hyperthermia uniformly throughout the tumor leaving cancerous cells resulting in regrowth of tumor [136].

Targeted Au and IONP mediated hyperthermia has been explored to enhance treatment specificity and increase heating uniformity [137] and can be initiated via magnetic or light induction. Magnetic hyperthermia is induced through exposing magnetic nanoparticles to an

alternating magnetic field (AMF) [31, 138]. Light-induced hyperthermia, Photothermal therapy (PTT), is the use of electromagnetic radiation (infrared wavelengths) to convert NIR light energy into heat [139, 140]. The objective of preclinical work in this area has been to determine the feasibility of administering antibody conjugated Au and IONPs directed to the disease site by tumor antigen targeting antibodies followed by initiation of thermal activation by either magnetic or light induction. The following are overviews of some of the recent *in vitro* and *in vivo* studies in this area.

1.6.1.1 In vitro Hyperthermia Studies

Nanoparticle mediated hyperthermia with bioconjugated antigen-targeted photothermal therapeutic agents have been of particular interest for breast cancer theranostic applications [141]. Loo et. al. reported dual gold nanoshells conjugated with anti-HER2 mAb via attachment with a PEG linker for imaging and photothermal therapy of breast cancer cells. The gold nanoshells were incubated with SKBr3 breast cancer cells for binding studies. Results of the study showed significantly increased scatter-based on optical contrast due to nanoshell selective binding to breast cancer cells as compared to control cell groups [142]. The anti-HER2 nanoshells also exhibited a targeted photothermal effect, as cell death occurred as a result of as treatment with a NIR laser after exposure to anti-HER2 nanoshells. The effect was not seen with nanoshells labeled with a non-specific control antibody and unconjugated nanoshells. This study demonstrated the bioimaging and cancer therapeutic potential of mAb conjugated gold nanoshells with a clinically relevant biomarker, HER2.

Hybrid nanoparticles (HNPs) have also been investigated for use in MRI guided PTT. Melancon et. al. reported HNPs for use in MRI guided laser ablation of head and neck cancer as a minimally invasive alternative for patients who are not candidates for surgery [34]. In this study a SPIO core covered in amorphous silica was coated with a gold nanoshell (SPIO@Au). The

particles were conjugated with anti-EGFR Cetuximab (C225) and tested for their capacity to selectively ablate human squamous carcinoma cell lines overexpressing EGFR *in vitro*. The results of the study showed that the C225-SPIO@Au conjugates could produce temperature in excess of 65 °C and cell death was only apparent with cells incubated with C225-SPIO@Au nanoshells after exposure to NIR laser light for 3 minutes. MRI detection was carried out using cells inoculated with the HNP conjugates and then suspended in agar. Cells inoculated with C225-SPIO@Au nanoshells showed darker contrast than the non-targeted control samples and the antibody blocked control. The biodistribution of these nanoshell conjugates showed selective uptake into tumors in comparison to PEG coated SPIO@Au. However, a majority of the conjugates localized to the liver, spleen, and kidneys. In addition, the authors did not demonstrate *in vivo* ablation of tumors using the C225 functionalized nanoshells.

1.6.1.2 In vivo Hyperthermia Studies

Preclinical *in vivo* studies for targeted hyperthermia have investigated the potential for antibody-conjugated nanoparticles to improve hyperthermia treatment. In one study, multifunctional gold-iron oxide HNPs targeted with humanized single chain antibody conjugates (A33ScFv) were studied in SW1222 cells (antigen-expressing colorectal cancer cell line) for use in laser assisted photothermal therapy using near-IR irradiation and MRI contrast agents *in vivo*. The HNPs in this study were effective MRI contrast agents reducing the post-contrast phase T_2 value by 50%. The HNPs showed localization to SW1222 tumor xenographs within 12 hours of systemic injection. The efficacy of photothermal treatment was confirmed by a significant reduction in tumor volume in samples treated with targeted HNPs exposed to NIR laser, Figure 1.5. Histological analysis further confirmed degradation of the extracellular matrix, cell necrosis, and nucleus damage/shrinkage in the treatment group. PTT resulted in necrosis in ~65% of tumor tissue [143].

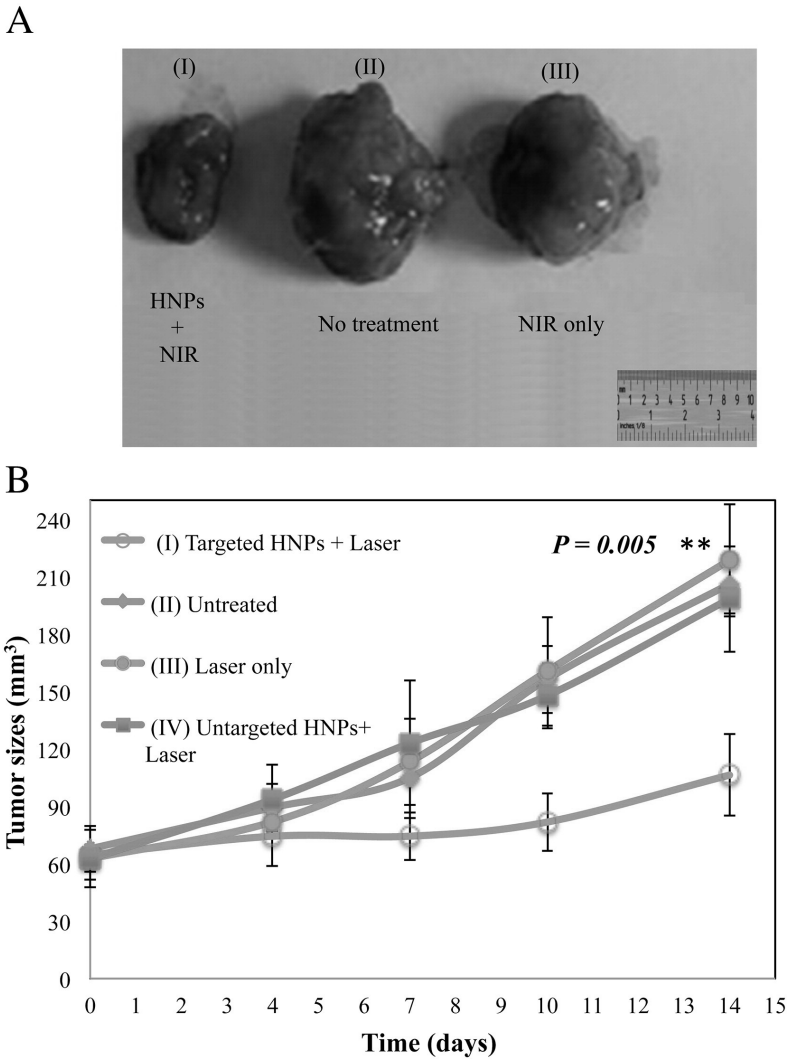

Figure 1.5 Photothermal therapy (PTT) response on subcutaneous colorectal tumors.
A) Tumor masses harvested after treatment with HNPs and NIR laser (group I), untreated control (group II), or PBS plus NIR laser (group III). B) Tumor growth curves after PTT. Tumor size calculated as $a*b^2/2$ (a=length and b=width), measured 24 h after irradiation and the duration of therapy, (n=5 mice per group). Reprinted from Nanomedicine, 9(5), Kirui, D. K., I. Khalidov, et al., "Targeted near-IR hybrid magnetic nanoparticles for in vivo cancer therapy and imaging", Copyright 2013, with permission from Elsevier.

1.6.2 Targeted Drug Delivery

Current cancer drug therapies are limited by inefficient delivery due to insolubility, toxicity and non-specificity [144]. Using nanoparticles as the delivery platform for many of these therapies

has the potential to overcome these limitations. Nanoparticles provide a large surface area-to-volume ratio, which allows them to bind, absorb, and carry a large variety of chemical compounds [145]. Coupling chemical compounds with nanoparticles has shown to increase the aqueous stability of many insoluble drugs and provide specificity, which leads to lower dosage requirements reducing harmful side effects [144, 146].

The use of AuNPs and IONPs as a drug delivery system has been shown to increase the effectiveness of several anti-cancer drugs. Several mechanisms are attributed to this increase in efficiency including: increased solubility of the active therapy, nanoparticle mediated cellular uptake, and prolonged circulation and receptor wrapping time [147]. For example, AuNPs have been shown to increase the efficacy of the chemotherapy drugs Doxorubicin (DOX) and Gemcitabine (Gemzar) [148, 149]. The stability in solution and cytotoxicity of the originally hydrophobic chemotherapy drug, Paclitaxel, was also significantly increased after its conjugation to AuNPs [144, 145]. Optimization of this system using pegylated AuNPs with biotin receptors has further enhanced the cytotoxic effects of Paclitaxel [145]. For IONPs, there is an increase in cellular uptake of drugs when they are carried by drug coated IONPs, and in certain cases even in cells experiencing drug resistance [150, 151]. Methotrexate, an antimetabolite used in the treatment of various cancers has been successfully conjugated with IONPs, resulting in increases cytotoxicity to target cells due to an increase in cellular uptake [146].

AuNPs and IONPs can not only carry drugs to target locations, but also can be used for controlled drug release. Triggered drug release from AuNPs and IONPs has been achieved with various activators including X-rays, glutathione and changes in environmental pH [67, 147, 152-154]. Notably, local irradiation of gold nanorods bound to a therapeutic via a thiol group has been shown to result in detachment of the drug in the local area, reducing non-specific dispersion

of standalone drugs which can lead to toxicity in non-targeted organs [155]. Preliminary studies also show that radiofrequency electromagnetic field (EMF) activation can also be an effective trigger for the independent release of multiple drugs on a single nanoparticle using nucleic acid tethers [156]. The following are highlights of recent *in vitro* and *in vivo* preclinical studies in this area.

1.6.2.1 In vitro Targeted Drug Delivery Studies

Bisker *et al.* conducted a controlled release study with AuNPs conjugated with Rituximab, an anti-CD20 mAb, for treatment of leukemia, Figure 1.6 [157]. 20 nm AuNPs were conjugated with PEGylated anti-CD20 via thiol chemistry. The functionalized AuNPs were incubated with Human CD-20 positive B-cell line for controlled release studies. Controlled release of anti-CD20 was activated upon irradiation by a femtosecond pulse train whose wavelength was tuned to match the plasmon resonance of the AuNPs. Released anti-CD20 retained functionality, inducing complement-dependent cytotoxicity, where complement proteins in blood serum act to induce necrosis of cells marked by Rituximab [157]. In addition, plasmonic shock waves emanating from the AuNPs, as a result of irradiation, initiated cell death. Advantages of this system include high specificity and efficiency, low toxicity, and high repeatability and consistency due to the morphological stability of the nanoparticles.

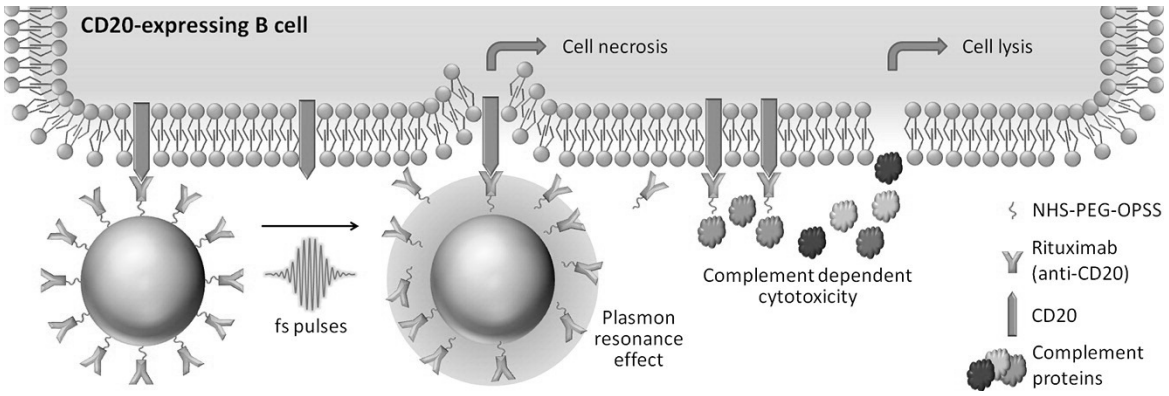

Figure 1.6 Controlled release of Rituximab from Gold Nanoparticles.
Targeted nanoparticles bind to CD20 expressing cells and are laser irradiated to release Rituximab, which recruits complement proteins to induce complement-dependent cytotoxicity CDC mediated cell death. Reprinted from the Journal of Controlled Release, Bisker, G., et al., Controlled release of Rituximab from gold nanoparticles for phototherapy of malignant cells, 2012. ***162****(2): p. 303-9 with permission from Elsevier.*

Dilnawaz et. al. conducted an *in vitro* study with HER2 antibody conjugated glycerol monooleate (GMO) coated IONPs loaded with different anticancer chemotherapeutic drugs (paclitaxel, rapamycin, alone or combination) and for use as active cancer therapeutics, Figure 1.7 [158]. Approximately 95% drug entrapment was achieved via absorption in the GMO coating and sustained release occurred over a two-week period. Conjugation to the HER2 antibody increased cellular uptake of GMO-IONPs by human breast cancer carcinoma cell lines (MCF-7) cells 3 fold compared with non-targeted GMO-IONPs. The targeted drug loaded GMO-IONPs were 55 times more effective than the native drug and 7 times more effective than the unconjugated NPs indicating potential anti-proliferation effect in MCF-7 [158]. Thus demonstrating the potential for drug-loaded antibody conjugated IONPs as potential drug carriers for improved drug efficiency and selectivity that would reduce unwanted side effects caused by damage to normal healthy tissue.

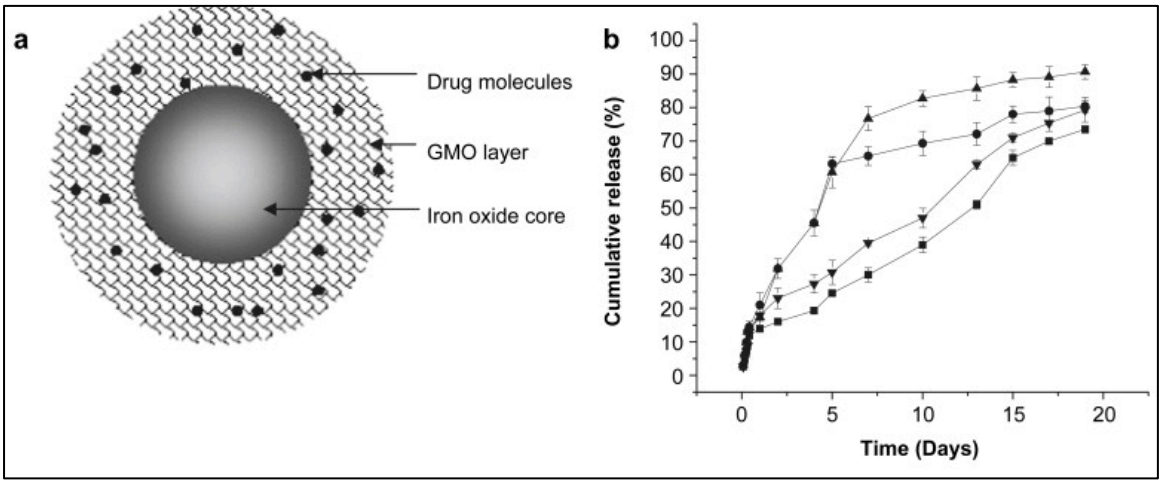

Figure 1.7 Drug Adsorption and Drug release of GMO coated Drug loaded Magnetic Iron Oxide Nanoparticles (IONPs).

(a) Schematic representation of drug adsorption in the GMO coating surrounding the iron oxide nanoparticle core. (b) Release of rapamycin from rapa-GMO-IONPs (•), paclitaxel (*) from pac-GMO-IONPs, rapamycin (▲) from combo-GMO-IONPs, and paclitaxel (▼) from combo-GMO-IONPs under in vitro conditions. Reprinted from Biomaterials, 31(13), Dilnawaz, F et. al., "Dual drug loaded superparamagnetic iron oxide nanoparticles for targeted cancer therapy" Copy right 2010, with permission from Elsevier [158].

1.6.2.2 In vivo Imaging and Targeted Drug delivery

Multifunctional IONPs have been developed for combined targeted imaging and drug delivery. Of particular interest are IONPs as nanocarriers for MRI imaging and drug delivery, conjugated with anti-HER2 trastuzumab and DOX [124]. In a recent in vivo study by Zolata et. al. polymer coated IONPs were Inium-11 labeled and conjugated with Trastuzumab-Doxorubicin for tumor targeting, drug deliver, controlled release, and dual-modal tumor imaging [159]. The theranostic effect of the immunotargeted and drug loaded IONPs were evaluated in HER2 positive breast tumor model bearing BALB/c mice via biodistribution, molecular imaging, and tumor morphology measurements. Antibody conjugated NPs from this study accumulated at very high concentrations in tumors due to targeting specificity, when compared with non-targeted NP controls. Imaging results via Single photon emission computed tomography (SPECT) and MRI studies showed that tumor region was clearly contrasted by the antibody

conjugated IONPs. Additionally, tumor volumes were up to 50% lower than control groups, indicating a significant therapeutic effect. The findings support multifunctional modified SPIONs for cancer theranostics, i.e. imaging and drug delivery applications.

1.7 Targeted SPIONs for Solid Tumor Vascular Occlusion

The work presented in the following chapters will detail a novel approach to solid tumor therapy, via selectively occluding the neovasculature of tumors with multimodal SPIONs. Our modular nanoparticle design combines three components to create targeted occlusion of solid tumor vasculature; (1) SPIONs conjugated with a fusion dual modal protein consisting of the (2) Polyhydroxyalkanoates (PHA) Synthase enzyme and (3) Prostate Specific Membrane Antigen (PSMA) specific J591 ScFv. The PHA synthase enzyme initiates the conversion of (R)-3-hydroxyacyl-CoA thioester (3HBCoA) substrate, monomer units, to Polyhydroxybutyrate (PHB) polymer with the concomitant release of CoA [160]. The J591 ScFv is recognizes an extracellular epitope of PSMA. PSMA is a unique tumor neovasculature target as it is limited to and consistently expressed in non-prostatic neovasculature of malignant neoplasms [161, 162].

The PSMA targeted SPIONs will discriminately deliver the primary PHB polymer-synthesizing enzyme, Polyhydroxyalkanoate (PHA) synthase, to the endothelia of solid tumor neovasculature and once there, 3HBCoA substrate will be administered, and the enzyme will initiate the synthesis of PHB polymer occluding the vessels, as outlined in Figure 1.8.

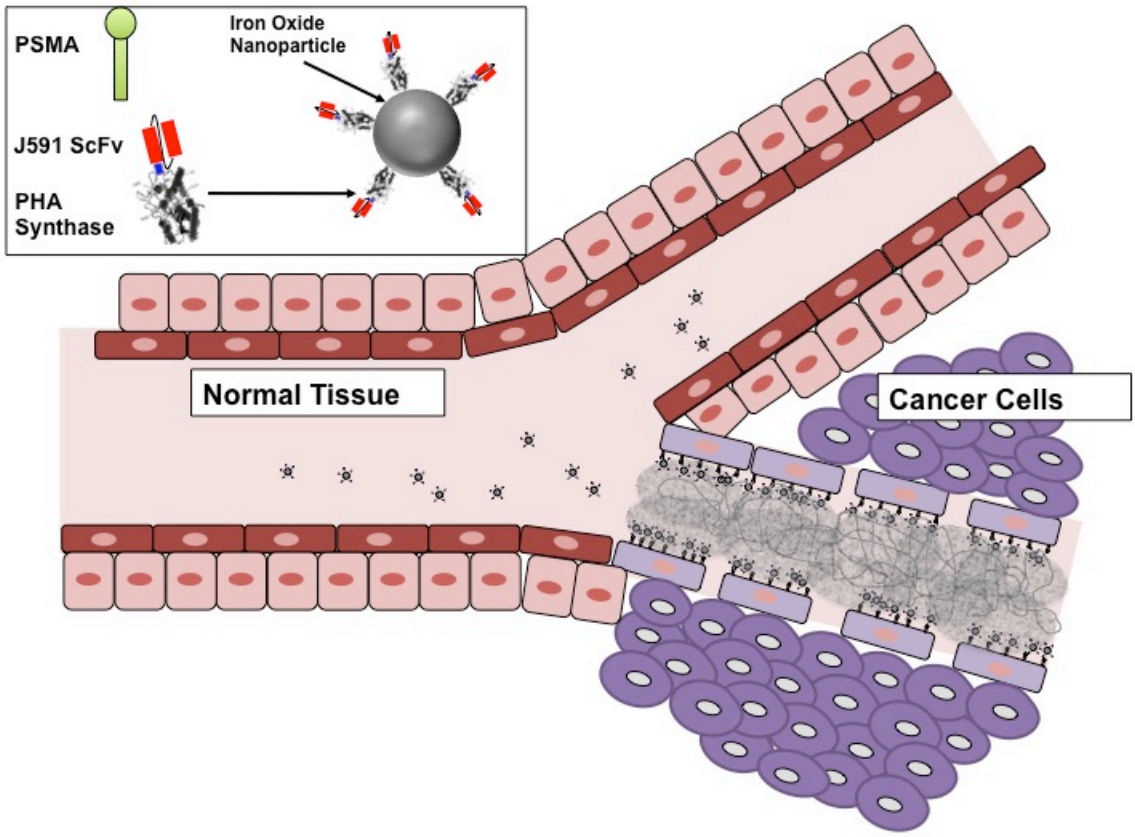

Figure 1.8 Schematic of PHB granule induced vascular occlusion of the tumor neovaculature as a method for targeted solid tumor therapy.
The PSMA targeted SPIONs will discriminately deliver the primary PHB polymer-synthesizing enzyme, Polyhydroxyalkanoate (PHA) synthase, to the endothelia of solid tumor neovasculature and once there, 3HBCoA substrate will be administered, and the enzyme will initiate the synthesis of PHB polymer occluding the vessels.

The following work details the development of the Nanoparticle platform for: **in situ growth of PHB polymer catalyzed by PHA synthase from the 3HBCoA monomer substrate, distributed within solid tumor microvasculature by targeted antibody-conjugated SPIONs, to cause tissue ischemia, resulting in tumor necrosis (Figure 1.8)**.

1.7.1 PSMA and J591 mAb

Prostate specific membrane antigen (PSMA; folate hydrolase 1, glutamate carboxypeptidaase II) is a 100 kDa type II integral membrane glycoprotein that is highly expressed in prostate cancers. PSMA functions as a folate hydrolase, providing PSMA expressing cells with a selective growth

advantage since PSMA may convert extracellular poly-γ-glutamated folate to a form that cells can import [163, 164]. PSMA is a solid tumor neovasculature marker for multiple non-prostatic solid tumors, including gastric and colorectal cancer, without expression by the tumor or normal vascular endothelium [161, 162, 165-169]. Evidence suggests that PSMA expression in associated neovasculature may be related to the degree and nature of angiogenesis, and that PSMA expression is greatest in high-grade and hormone-insensitive cancers [162, 170].

PSMA was first characterized in prostate cancer by the monoclonal antibody (mAb) 7E11. The stable clone of murine hybridoma 7E11-C5 was obtained following immunization with human prostate cancer LNCap cells [171]. The specificity of the 7E11 mAb was found to be restricted to normal and malignant human prostatic epithelium [171]. PSMA has been targeted successfully in vivo with the 7E11 mAb, which is specific to an intracellular epitope of PSMA [172]. There is currently an FDA approved ^{111}In-labeled 7E11 mAb for clinical diagnosis of recurrent and metastatic prostate cancer in soft tissue [172].

Several anti-PSMA mAbs were characterized to the internal domain (7E11 and PM2J004.5) and external domain (J591, J415, E99, J533, PEQ226.5) of PSMA. However, the mAbs to the intracellular domain of PSMA do not bind to viable PSMA expressing cell, whereas mAbs to the external domain do bind live cells [162, 173]. The IgG J591 mAb is well characterized and has the same nanomolar affinity to PSMA as 7E11 mAb [174-176]. J591 mAb detects a distinct extracellular epitope of PSMA ($PSMA_{ext1}$) [167, 177]. The findings of two phase I clinical trials demonstrated that mAb J591 specifically targets PSMA on the vascular endothelium of metastases in patients with multiple solid tumor types with minimal toxicity [165, 178].

J591 mAb thus is potentially suitable for use in the development of tumor-targeted cancer treatment, allowing for the preservation of healthy tissue. Further, recent studies have

investigated the use of the J591 mAb to facilitate targeted prostate cancer therapy. One study found adenovirus vectors retargeted with J591 mAb to increase the effectiveness of viral gene-therapy targeting adenovirus vectors to PSMA [179]. Another study by Liu *et al.* found that the insertion of a J591 single-chain Fv cloned from the J591 mAb hybridoma cDNA as a C terminal extension to a measles virus specifically targeted PSMA expressing prostate cancer cells *in vitro* and *in vivo* resulting in a cytopathic effect [180].

1.7.2 PHA Polyhydroxyalkanoates and PHA Synthase

Polyhydroxyalkanoates (PHAs) are polyesters of hydroxyalkanoates that represent a complex class of aliphatic polyesters synthesized by a majority of bacteria and members of the Halobacteriaceae family of the Archaea. When one or more nutritional elements such as nitrogen, phosphate, sulfur, iron, oxygen, potassium, or magnesium is limited in the presence of excess carbon bacteria synthesize and accumulate non-crystalline PHA granules as carbon and energy storage compounds [181, 182]. Typical granule size is between 0.2 to 0.5 μm, and depends on the bacteria cell forming the polymer granules [181]. As much as 90% of the dry cell weight can be composed of the PHA polymer [183]. PHAs are natural polymers and are currently being investigated for use in biomedical applications [184]. Interest in PHA is due to its biodegradable, thermoplastic, and elastomer material properties. PHA is biocompatible and has a low degradation rate, in biological environments, degrading to carbon dioxide and water. PHA polymer composites have been used to develop devices for bone and tissue repair including sutures, tacks, staples, slings, bone plates, adhesion barriers, stents, articular cartilage repair devices, wound dressing, and hemostats [185]. Further recent *in vivo* animal studies have demonstrated the potential for the use of PHB microspheres for embolisation [186] and PHB polymer for bowel repair [187].

Polyhydroxybutyrate (PHB) was the first PHA to be discovered and PHA synthase from *W. eutropha* H16 (64kD) is the most characterized [182, 188, 189]. PHA synthases are the key enzymes of PHA biosynthesis and are the sole enzymes required for the biosynthesis of PHA granules [190]. PHA synthase will initiate the formation of PHA polymer either *in vivo* or *in vitro* to create macroscopic granules [184, 191]. *In vitro* production of PHA polymer requires purification of PHA synthase enzyme from bacteria. In *E. coli* soluble forms of the enzyme are purified from recombinant strains[192, 193]. .= PHA synthase initiates the conversion of (R)-3-hydroxyacyl-CoA thioester substrate to PHAs with the concomitant release of CoA [160]. Synthesis of PHB from PHA synthase by recombinant *E. coli* does not require nutrient limitations; instead it is dependent on the amount of actetyl-CoA substrate available [182, 194].

1.7.3 Novel Proteins for Vascular Occlusion

The following chapters detail the design, production, and characterization of two novel proteins necessary for the achievement of our targeted vascular occlusion approach: the (1) J591 ScFv and (2) J591 ScFv and PHA Synthase enzyme fusion protein. The J591 ScFv, is a single chain variable fragment (J591 ScFv) that recognizes the extracellular glyco-protein prostate specific membrane antigen (PSMA). Construction of the J591 ScFv was based on the reported complementarity-determining region (CDR) of the PSMA specific J591 monoclonal antibody (mAb). The J591 ScFv and PHA Synthase enzyme fusion protein combines the PSMA targeting J591 ScFv and PHB polymer synthesizing PHA Synthase enzyme to create a means of systematically targeting tumor neovasculature and delivering the PHA Synthase enzyme via the a single protein. Both proteins were expressed in the *Pichia pastoris* expression system.

1.8 Conclusion

Gold, iron oxide, and hybrid nanoparticles functionalized with cancer specific antibodies provide attractive platforms for potent next-generation cancer theranostics, which couple diagnostics with therapies. Preclinical studies with immunotargeted nanoparticles have demonstrated more specific therapies with the potential to result in reduced side effects in comparison to convectional treatment strategies. Further, treatment at the nanoscale allows for cellular level cancer detection, providing a means to eliminate cancer at the cellular level and thus reduce cancer reoccurrence. Thus gold and iron oxide nanoparticles conjugated with antibodies enhance optical signal and provide a sensitive strategy for detection and destruction of cancer cells that could potentially lead to paradigm shift in cancer treatment strategies.

CHAPTER 2 Design, production, and characterization of a single-chain variable fragment (ScFv) derived from the prostate specific membrane antigen (PSMA) monoclonal antibody J591

Reprinted from, Protein Expression and Purification 89 136-145, **S.A. Parker**, I.L.-C. Diaz, K.A. Anderson, C.A. Batt, Design, production, and characterization of a single-chain variable fragment (ScFv) derived from the prostate specific membrane antigen (PSMA) monoclonal antibody J591, 136-145, (2013), with permission from Elsevier

2.1 Abstract

A single chain variable fragment (J591 ScFv) that recognizes the extracellular glycoprotein prostate specific membrane antigen (PSMA) was designed, constructed, and expressed in *Pichia pastoris*. Construction of the J591 ScFv was based on the reported complementarity-determining region (CDR) of the PSMA specific J591 monoclonal antibody (mAb). The nucleotide sequence encoding the J591-derived ScFv was codon-optimized for expression in *P. pastoris* and a 6X his-tag was added to facilitate affinity purification. A down-scale 2 L methanol-induced *P. pastoris* fermentation yielded 330 mg of total protein following a 96 h induction. Following Immobolized Metal Affinity Chromatography, functionality of the J591 ScFv was confirmed via Western blot, immunoblot, binding studies, and flow cytometry analysis. The J591 ScFv showed binding affinity and specificity to cell extracts containing PSMA and PSMA-expressing prostate cancer cells. Our results demonstrate that functional J591 ScFv can be produced in *P. pastoris* for use in diagnostic and targeted therapeutic applications.

2.2 Introduction

Monoclonal antibodies as therapeutics are an integral part of clinical regimens. Currently there are over 25 antibodies approved for human therapy and over 240 antibodies in development worldwide for a wide range of diseases, including cancer [195]. Antibodies developed for use in cancer therapy are specific for antigens expressed by the tumor. Among these is the IgG J591 monoclonal antibody (J591 mAb), a well-characterized antibody that binds to the extracellular domain of prostate specific membrane antigen (PSMA) [196-198].

PSMA is a type II integral membrane glycoprotein produced by the prostatic epithelium [199]. PSMA is over-expressed at all stages of prostate cancer [200]. Further, PSMA is a solid tumor neovasculature marker for multiple non-prostatic solid tumors, including gastric and colorectal cancer, without expression by the tumor cells or normal vascular endothelium [169, 199, 201-204]. These characteristics render PSMA a prime candidate for use in tumor-targeted cancer therapy [201, 205, 206]. J591 mAb is reactive to a distinct extracellular epitope of PSMA ($PSMA_{ext1}$) [204, 207]. The findings of two phase I clinical trials demonstrated that J591 mAb specifically targets PSMA on the vascular endothelium of metastases in patients with multiple solid tumor types with minimal toxicity [201, 208]. Additionally, recent studies have investigated the use of the J591 mAb to facilitate targeted prostate cancer immunotherapy. One study found adenovirus vectors retargeted with J591 mAb increased the effectiveness of viral gene-therapy targeting adenovirus vectors to PSMA [205]. Additionally, clinical trials where ^{111}indium-labeled mAb J591 was administered to patients with advanced tumor malignancies suggest a J591 mAb dose of 40 mg be considered for future clinical trials [201]. The promising results of these studies provide evidence for PSMA targeting via the J591 mAb as a viable option for solid tumor therapy.

However, monoclonal antibodies are large complex molecules and can present immunogenicity concerns [209]. Protein-engineering technology has allowed for the development of single chain variable fragments of full antibodies to address these obstacles. ScFv fragments are the smallest active antigen-binding unit of immunoglobin molecules and have been combined with antibody domains and protein domains to generate bispecific antibody fragment formats [195, 210, 211]. These new class of

molecules which simultaneously target epitopes on tumor cells as well as molecules expressed by immune effector cells, have recently led to successful clinical results and have potential for use in development of novel cancer immunotherapeutics in a near future [212-214]. ScFvs are thus an attractive antibody format for tumor targeting and have been investigated for radioimmunoimaging and specific delivery of cytotoxic agents [215-217].

In this study we report the construction, purification, characterization, and *in vitro* testing of a novel anti-PSMA single-chain variable fragment of the J591 monoclonal antibody, with added features for ease of production and purification. The J591 ScFv was optimized for expression in a *P. pastoris expression* platform and a 6X his-tag was introduced to allow for immobilized metal affinity chromatography purification. A 17-amino acid linker was used to connect the variable heavy (V_H) and variable light (V_L) regions of the ScFv and was specifically designed for stability in *P. pastoris*. The robust design of our ScFv construct resulted in production of a biochemically active ScFv in *P. pastoris*. The features added to our ScFv construct, its down-scale production, and its reactivity to PSMA have been demonstrated. This is the first reported J591 ScFv expressed in *P. pastoris*.

2.3 Materials and Methods

2.3.1 Organisms

Escherichia coli DH5α and TOP10F' *E. coli* cells (C303006, Life Technologies, Carlsbad, CA USA) were used for cloning of the J591 ScFv nucleotide sequence in the pPIC9K plasmid (V17520, Life Technologies, Carlsbad, CA USA). The His Strains *P.*

pastoris GS115 and KM71 were used for expression of the J591 ScFv (Pichia Expression Kit, Version M, Life Technologies, Carlsbad, CA USA).

2.3.2 Cell lines and Cultures

The LNCaP prostate cancer cell line and PC3 cell lines (PC3-PIP, PC3-Flu, and PC3) were generously provided by Dr. Neil Bander (Weill Medical College of Cornell University, New York, NY USA). The cell lines were cultured in RPMI 1640 medium F12-K (Life Technologies, Carlsbad, CA USA) supplemented with: 10% (v/v) fetal bovine serum (FBS) and 1% penicillin–streptomycin (P/S, 100 units mL^{-1} penicillin, and 100 μg/mL streptomycin) and Minimum Essential Media (Life Technologies, Carlsbad, CA USA) supplemented with: 1% penicillin–streptomycin respectively at 37^{o}C and 5% CO_2 in a humidified incubator.

2.3.3 Construction of the J591 ScFv

Genes encoding the V_H and V_L chains of the J591 mAb were synthesized by IDT (Integrated DNA Technologies, Inc., Coralville, IA USA). A 17-amino acid linker sequence fused the V_H and V_L chains to generate a single 0.7 kb peptide. PCR amplification of the V_H and V_L was used to introduce N-terminal 6X histidine tag, kex2 recognition site, and flanking restriction sites *XhoI* and *NotI*.

2.3.4 Cloning

The PCR amplified J591 ScFv fragment was sub-cloned with the pCR2.1 Life Technologies TOPO TA kit following the manufacturers protocol (Life Technologies, Carlsbad, CA USA). Subsequently, the pCR2.1-J591 ScFv vector was simultaneously digested with *XhoI* and *NotI* restriction enzymes. The 0.7 kb digestion product

containing the J591 ScFv was then cloned into the *XhoI-NotI* restriction sites of the pPIC9K vector to generate the pPIC9K-J591 ScFv construct. The J591 ScFv was cloned in frame with the initiation codon of the secretion signal (α-factor mating signal) open reading frame of the pPIC9K vector, a 9.6 kb *P. pastoris* expression vector.

The pPIC9K-J591 ScFv vector was then cloned by electroporation into TOP10F' *E. coli* cells. Transformants were selected by growth on LuriaBertani (LB) agar plates supplemented with 100 μg/mL of ampicillin. Transformed colonies from the plate were cultured overnight at 37°C in 5 mL of medium containing LB and 100 μg/mL of ampicillin. Transformant plasmid DNA was isolated by miniprep (Zyppy Plasmid Miniprep kit, Zymo Research Group, Irvine, CA USA) for DNA sequencing, performed at the Cornell University Life Science Core Laboratories Center (Cornell University Ithaca, NY USA), to verify assembly of the single chain.

Preparation of competent cells and transformation of *P. pastoris* was performed in accordance with Lin-Cereghino's previously reported condensed protocol [218]. Briefly the transformation was as follows: Approximately 4 μL (50-100 ng) of linearized plasmid was mixed with 40 μL of electrocompetent *P. pastoris* GS115 (His^+Mut^+) or KM71 (His^+Mut^S) cells. Plasmid and cells were transferred to a 0.2-cm electroporation cuvette. Electroporation was carried out in a Bio-Rad Gene Pulser with charging voltage of 1500 V, capacitance of 25 μF, and resistance of 200 Ω. Immediately after electroporation, 1 mL of ice-cold 1 M sorbitol was added to the cuvette, and 200, 100, 50 and 10 μL aliquots were spread onto minimal dextrose (MD) plates lacking histidine. The plates were incubated for 2 days at 30°C for selection of His+ transformants.

2.3.5 J591 ScFv Expression

The pPIC9K-J591 ScFv construct expressed the J591 ScFv under the control of the strong methanol-inducible alcohol oxidase (AOX1) promoter [219]. Four His^+Mut^+ transformants and four His^+Mut^S transformants were screened for the production of J591 ScFv. Single colonies of GS115 and KM71 were used to inoculate 5 mL Yeast Extract Peptone Dextrose (YPD) [1% (w/v) yeast extract (EMD Millipore Chemicals, Darmstadt, Germany), 2% (w/v) peptone (Difco Laboratories Inc., Franklin Lakes, NJ USA), and 2% (w/v) dextrose (VWR Chemicals, West Chester, PA, USA)] and grown overnight at 25ºC with vigorous shaking. Each 5 mL culture was used to inoculate 25 mL of Buffered Minimal Glycerol Histidine (BMGH) [1% (w/v) yeast extract, 2% (w/v) peptone, 100 mM potassium phosphate pH 6.0, 1.34% (w/v) YNB (Becton, Dickinson and Co., Franklin Lakes, NJ, USA), 4 x 10^{-5} % (w/v) biotin (Sigma-Aldrich, St. Louis, MO, USA), 1% (v/v) glycerol (VWR Chemicals, West Chester, PA, USA), and 0.004% histidine (Sigma-Aldrich, St. Louis, MO, USA)] at pH 6.0 in a 250 mL baffled flask adjusting them to an OD_{600} of 1.0. They were then grown at 15°C in a shaking incubator (250–300 rpm) until the culture reached an OD_{600} of 2-4. Cells were then harvested by centrifuging at 3500 x g for 10 min at room temperature. To induce expression, the supernatant was decanted and the cell pellet was resuspended in 10 mL of Buffered Minimal Methanol Histidine (BMMH) [100 mM potassium phosphate pH 6.0, 1.34% (w/v) YNB, 4 x 10^{-5} % (w/v) biotin, 0.5% (v/v) methanol, and 0.004% histidine] at pH 6.0 and grown at 15°C for 24 h. 0.5% methanol was added for induction every 24 h. Following 36 h of induction the optical density and protein concentration of the cultures were measured and supernatants were analyzed through SDS-PAGE Coomasie and Western blotting.

2.3.6 Down-Scale J591 ScFv Expression Fermentation

Fermentations were performed following our previously published protocol for single-chain Fv production in *P. pastoris* [220]. A single *P. pastoris* GS115 His^+Mut^+ transformant was used to inoculate 5 mL YPD. The culture was grown overnight at 30°C. A 24 μL aliquot of the overnight culture was used to inoculate 100 mL BMGY [1% (w/v) yeast extract, 2% (w/v) peptone, 100 mM potassium phosphate, pH 6.0, 1.34% (w/v) YNB, 4 x 10^{-5} % (w/v) biotin, and 1% (v/v) glycerol] in a 250 mL baffled flask and incubated at 30°C until the culture reached an OD_{600} of approximately 20. This culture was used to inoculate 1.1 L of fermentation media.

A 2 L working volume was used to conduct fermentations using a Bioflo 300 (New Brunswick Scientific, Edison, NJ USA) interfaced with AFS-Biocommand Bioprocessing software version 2.6 (New Brunswick Scientific) for data acquisition and operational control. A 1.1 L starting volume of modified basal salts medium [221] [0.23 gL^{-1} $CaSO_4 \cdot 2H_2O$, 4.55 gL^{-1} K_2SO_4, 3.73 gL^{-1} $MgSO_4 \cdot 7H_2O$, 1.03 gL^{-1} KOH, 6.68 mLL^{-1} H_3PO_4, and 5 % (v/v) glycerol] and 0.5 mL Antifoam 204 (Sigma-Aldrich, St. Louis, MO) was sterilized inside the reactor. Ammonium hydroxide [15% (v/v)] was used as a pH control agent and nitrogen source. The pH was measured with an Accumet pH electrode (Fisher Scientific). Prior to inoculation 4.35 mL L^{-1} of PTM_1 trace salts (24 mM $CuSO_4$, 0.53 mM NaI, 19.87 mM $MnSO_4$, 0.83 mM Na_2MoO_4, 0.32 mM boric acid, 2.1 mM $CoCl_2$, 0.14 mM $ZnCl_2$, 0.23 M $FeSO_4$, and 0.82 mM biotin) were added aseptically.

The fermentation was inoculated with the 100 mL overnight culture in BMGY. The fermentation was maintained at 25°C and a pH value of 4.0 throughout the batch and induction stages. Dissolved oxygen (DO) levels were maintained at 40% of saturation

and controlled by a DO cascade of agitation (maximum of 1000rpm) and supplemented with pure oxygen as required. Oxygen concentration was measured with an InProb6110/220 electrode (Mettler-Toledo GmbH, Germany).

The batch phase was continued until the glycerol was consumed, indicated by a sharp increase in the DO. Following the batch phase the culture was induced with a methanol feed (100% methanol with 12 mL PTM_1 L^{-1} methanol) initiated by a closed loop Proportional-Integral-Differential (PID) control scheme. The control scheme consisted of the BioFlo 3000, a methanol probe (Raven Biotech, Vancouver, Canada), a PID controller Cni852-C4EI (Omega Engineering, Stanford, CT USA), and a Masterflex variable speed pump head (Cole-Parmer Instruments, Vernon Hills, IL USA). The methanol sensor was interfaced with Windmill Logger software (Windmill Software, Manchester, UK) for data acquisition. The methanol value was maintained at a value of 0.1 g/L for the entire 96 h induction phase. Samples were taken at 24 h intervals and the wet cell weight and protein concentration was measured for each time point.

2.3.7 Immobilized metal affinity chromatography

The fermentation supernatant was collected after induction and clarified through a 0.22 µm vacuum membrane filter (Nalgene Labware Thermo Scientific, Rockford, IL USA). Buffer exchange into the chromatography buffer system (50 mM sodium phosphate buffer, pH 7.4) was carried out using a tangential flow filtration system equipped with a 10 kDa membrane. All chromatography steps were done on an ÄKTA Explorer (GE Healthcare Bio-Sciences Corp. Piscataway, NJ USA). Immobilized metal affinity chromatography (IMAC) was performed using a HisTrap™FF 5 mL nickel column for poly-histidine tag binding. The purification scheme involved step gradient elution. The

equilibration, wash, and elution buffers were prepared by adding variable concentrations of imidazole (10 mM, 20 mM and 300 mM, respectively) to a buffer containing 50 mM NaH_2PO_4 (pH 7.4).

For purification first the 5 mL HisTrap column was equilibrated with 5 column volumes of equilibration buffer pH 7.4. Next a 150 mL volume of buffer exchanged (pH 7.4) clarified fermentation supernatant was loaded in the HisTrap Ni column on the ÄKTA. Then the column was washed with 20 mM imidazole elution buffer pH 7.4 to remove weakly bound proteins. The product was then eluted off of the column with 5 column volumes of the elution buffer pH 7.4. The elution fraction was automatically collected and imidazole was eliminated by buffer exchange into 50 mM NaH_2PO_4 (pH 7.0) using an Amicon Ultra-15 10 kDa centrifugal filter unit (Millipore, Billerica, MA USA).

2.3.8 SDS-PAGE, Western blotting, and Immunoblotting

Culture supernatant samples were analyzed by electrophoresis on 12% SDS–polyacrylamide gels (SDS-PAGE) under denaturing conditions following the standard protocols. The gels were stained with a Coomassie-based stain (SimplyBlue SafeStain, LC6060, Life Technologies, Carlsbad, CA USA) and the separated proteins using SDS-PAGE were transferred to a nitrocellulose membrane for Western blotting. The J591 ScFv was detected using Monoclonal Anti-polyHistidine−Alkaline Phosphatase antibody produced in mouse (Sigma-Aldrich, St. Louis, MO USA), in accordance with the manufacturer's protocols.

For immunoblotting two cells lines were used: PC3-PIP (PSMA+) /PC3-Flu (PSMA-). Cells were lysed, centrifuged, the cell supernatant was run on an SDS-PAGE, and transferred by electrophoresis to nitrocellulose paper. The J591 ScFv was used as the

primary antibody to detect PSMA (~100 kDa [199]) and the Monoclonal Anti-polyHistidine−Alkaline Phosphatase antibody produced in mouse (Sigma-Aldrich, St. Louis, MO USA) was used as the secondary antibody for detection of the histidine tagged ScFv.

2.3.9 Immunofluorescence ScFv Binding Assays

The purified J591 ScFv at a concentration of 1 mg/mL was fluorescently labeled with the Alexa Fluor 488 Monoclonal Antibody Labeling Kit according to the manufacturers protocol (A-20181, Life Technologies, Carlsbad, CA USA), for immunofluorescence assays. The labeled ScFv was purified via a Pierce slide-A-lyzer dialysis cassette 10K Molecular Weight Cut-Off (Thermo Scientific, Rockford, IL USA) following the manufacturers protocol. The J591 mAb was previously described and generously provided by Dr. Neil Bander (Weill Medical College of Cornell University, New York, NY USA [204]). The J591 mAb was fluorescently labeled and purified with Life Technologies' Alexa Fluor 488 Monoclonal Labeling Kit (Life Technologies, Carlsbad, CA USA) according to the manufacturer's instructions.

LNCaP cells were cultured, as previously described in RPMI medium, overnight on poly-lysine coated glass microscope cover slips in a 12-well plate, media was suctioned from the cultures, cell were fixed with 2% formaldehyde for 30 min, and then washed with phosphate buffer in preparation for the assays.

For immunofluorescence studies fixed LNCaP cells were permeabilized with 0.2% saponin in PBS for 30 min and incubated with either 10 μg/mL of the Alexa Fluor 488 labeled ScFv or J591 mAb in 2% BSA in PBS for 1 hr, washed three times with PBS, and fluorescence was observed at 800ms.

Fixed LNCaP cells were first incubated with concentrations of the purified ScFv: 0 and 50 μg/mL J591 ScFv in 2% BSA for 1 h and then washed three times with PBS, for competitive binding studies. Following washing the cells were incubated with 2 μg/mL of the Alexa Fluor 488 labeled J591 mAb in 2% BSA for 1 hr, washed, and fluorescence was observed at 400 ms and 5.60x gain. As a positive control the LNCaP cells were incubated with 10 μg/mL of unlabeled J591 mAb in 2% BSA for 1 h and then washed and incubated with 2 μg/mL of Alexa Fluor 488 labeled J591 mAb following the same protocol as described above.

Image Processing and Analysis in Java (ImageJ) (National Institutes of Health, Bethesda, MD USA) software was used to measure the fluorescence intensity of the images, the "mean gray value" in ImageJ. The background fluorescence was subtracted to obtain mean fluorescence for three cells in each image; the average of the three means was taken for each image. This measure was used to quantify the changes in fluorescence intensity in the competitive binding experiments.

2.3.10 Flow Cytometry analysis of J591 ScFv binding specificity for PSMA

LNCaP (PSMA+) and PC3 (PSMA-) cells were cultured to 80% confluence for flow cytometry analysis. The cells were then collected and resuspended in phosphate buffer (PBS) pH 7.5. The purified J591 ScFv at a concentration of .92 mg/mL was fluorescently labeled with the Alexa Fluor 488 according to the manufacture's protocol (Life Technologies, Carlsbad, CA USA). Unconjugated fluorophore was removed using Zeba™ spin desalting columns, 7K MWCO following the manufacture's protocol (Thermo Scientific, Rockford, IL USA). The degree of labeling was calculated as the moles of dye per mole of protein in accordance with the manufactures' prescribed

protocol using the molecular weight of the protein and the extinction coefficient calculated using the ProtParam software (ExPASy Bioformatics Resource Portal). Absorbance measurements of the labeled protein at 494 nm and 280 nm were taken using a Nanodrop ND-1000 (Thermo Scientific Waltham, MA USA). The calculated degree of labeling of the J591 ScFv was 2 moles of dye per mole of ScFv. 500,000 cells of either LNCaP or PC3 cells in PBS were incubated with 10 μg of labeled J591 ScFv for 30 mins at 4°C. The cells were then washed twice with 1 mL PBS via centrifugation at x 300 g, and then resuspended in 500 μL PBS with 1% paraformaldehyde. Flow cytometry was carried out using a Beckman Coulter Epics XL-MCL Flow Cytometer (Beckman Coulter, Brea, CA USA). Flow cytometry data were analyzed using WinMDI software version 2.9 (Scripps Research Institute, La Jolla, CA, USA).

2.3.11 Flow Cytometry Protein Blocking

Cells were stained with the J591 Fab labeled with the Alexa Fluor 488, as previously described, for protein blocking as analyzed by flow cytometry. The J591 Fab was prepared from the J591 mAb using a Fab Preparation Kit (Thermo Scientific, Rockford, IL USA) and was generously provided by Dr. Neil Bander (Weill Medical College of Cornell University, New York, NY USA). 500,000 LNCaP cells were first incubated with 0, 25, 50, or 100 μg of the unlabeled J591 ScFv for 30 mins at 4°C and then washed with 1 mL PBS via centrifugation at x 300 g. The cells were then incubated with either 5 or 10 μg of the labeled J591 Fab, washed with 1 mL PBS at x 300 g, and resuspended in 500 μL PBS with 1% paraformaldehyde. Flow cytometry was carried out using a BD FACSCanto II flow cytometer and analyzed using WinMDI software version 2.9.

2.3.12 Enzyme-Linked Immunosorbent Assay (ELISA)

Specific binding of the J591 ScFv to PSMA was measured by enzyme-linked immunosorbent assay (ELISA). Wells within a 96-well plate were coated with 100 µL of 1µg/mL of Human PSMA (R&D Systems, Minneapolis, MN) overnight at 4°C. Following incubation the wells were washed three times with Phosphate Buffer (PBS) containing 0.5% Tween, then the unbound sites were blocked with PBS containing 3% Bovine Serum Albumin (BSA) for 1 h at 37°C, and various dilutions of J591 ScFv in PBS containing 0.1% BSA were added for 1 h at room temperature. Unbound protein was removed by washing with PBS containing 0.5% tween three times and 0.25 ug/ml Peroxidase conjugated Protein L (Thermo Scientific, Rockford, IL) in PBS containing 0.1% BSA was added for 1 h. The wells were washed and TMB substrate was added and the optical density was measured at 450 nm (OD450). All experiments were conducted in triplicate.

2.4 Results and Discussion

In this study, we designed, constructed, and characterized the J591 ScFv derived from the J591 mAb and expressed in *P. pastoris* for down-scale production. One of the chief advantages of the *P. pastoris* expression system is its ability to secrete recombinant proteins in their active form simplifying downstream purification [222]. Recombinant proteins produced by *P. pastoris* are usually properly folded and this organism is devoid of immunogenic cell wall pyrogens found in *Escherichia coli* [223]. The *P. pastoris* expression system also lacks potentially oncogenic or viral nucleic acids, sometimes found in mammalian cells [223].

2.4.1 ScFv Design, Construction, and Cloning

The 0.7 kb J591 ScFv amino acid sequence was derived from the variable light and variable heavy chains of the J591 monoclonal antibody. To efficiently express the ScFv in *P. pastoris* we reduced possible translation and ScFv production limitations due to poor codon usage by codon optimizing the protein sequence for expression in *P. pastoris*. Preferred *P. pastoris* codon usage has been reported [224-226]. The Graphical Codon Usage Analyzer website (www.gcau.de) with the built in *P. pastoris* codon bias table was used to develop the codon optimized ScFv sequence [227]. The genetic code of the J591 mAb V_L and V_H regions were altered manually to closely match the *P. pastoris* codon bias. Adjustments made to the mAb coding sequence included changing the codons for Aspartic Acid from GAC to GAT and Arginine coded as AGG, CGC, and CGG in the mAb sequence was changed to AGA for the ScFv, in favor of the *P. pastoris* codon bias (www.gcau.de).

The variable light and variable heavy chain sequences were fused with a 17-aa linker sequence. This linker peptide sequence was developed for use in our previous ScFv expression work and has been shown to improve the stability of ScFvs expressed in *P. pastoris* [220]. Flanking restriction sites (*XhoI* and *NotI*) were added to aid in cloning (Figure 2.1A). An N-terminal 6X histidine tag was added as the primary method of protein purification as well as to facilitate immunodetection. The histidine tag can also serve as a mechanism to attach the ScFv to surfaces functionalized with Ni-NTA.

The J591 ScFv V_H and V_L chain oligonucleotides were synthesized by IDT (Integrated DNA Technologies, Inc., Coralville, IA). PCR amplification of the V_H and V_L was used to join the chains together via the 17–aa linker sequence, introduce N-terminal 6X

histidine tag, kex2 recognition site, and flanking restriction sites. The resulting peptide sequence was subcloned into the Life Technologies Topo 2.1 vector, utilizing the flanking restriction sites, and was further cloned into the pPIC9K *P. pastoris* expression vector in frame with the AOX1 methanol inducible promoter region (Figure 2.1B). Sequencing confirmed proper insertion of the 765 bp ScFv construct.

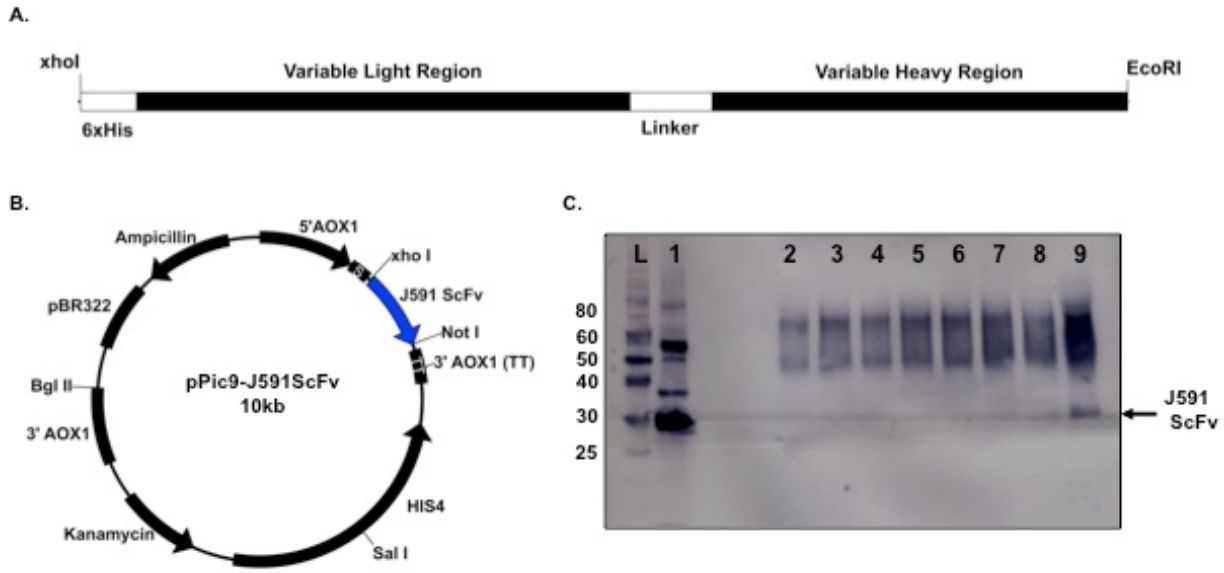

Figure 2.1 J591 ScFv Construct and Expression Screening.
A. The J591 ScFv construct (top) and B. pPIC9K-J591 ScFv plasmid map (bottom). The exploded view of the ScFv above the plasmid map displays the N terminal 6X his tag, variable light chain, variable heavy chain, and 17 amino acid linker region. C. Western Blot analysis of P. pastoris transformant supernatants screened for J591 ScFv secretion. Eight transformants were screened four KM71 His^{+}Mut^{S} (Lanes 2-5) and four GS115 His^{+}Mut^{+} (Lanes 6-9). Lanes: L) Ladder (Novex Sharp Standard) and 1) positive control poly his-tag GFP (27 kDa).

2.4.2 J591 ScFv Secretion in P. Pastoris

After transformation the resulting GS115 and KM71 *P. pastoris* transformants were screened for expression of the J591 ScFv as described previously. The 26 kDa J591 ScFv was secreted in the supernatant of methanol-induced *P. pastoris* as shown in the Western blot in Figure 2.1C. A GS115 His^{+}Mut^{+} with the highest secretion level measured via

absorbance at 595 nm was selected for further studies, among the eight transformants screened.

Following initial screening, taking advantage of the scalable expression capabilities of the *P. pastoris* expression system, the production of the J591 ScFv was scaled-up in a 2 L methanol-induced fermentation following our previously published protocol for *P. pastoris* fermentation for single-chain Fv expression [220]. The wet cell weight and protein concentration were taken every 24 h during the induction phase of the fermentation and are plotted in Figure 2.2A. As seen in Figure 2.2A the final wet cell weight is 0.43 g/mL and the protein concentration is 0.33 mg/mL after the 96 h induction. The resulting cell density from the fermentation based on the wet cell weight was 528 g/L after 220 h. The final volume of the supernatant collected after the fermentation was 1 L and had a protein concentration of 0.33 mg/mL resulting in a total protein of yield of 330 mg.

A.

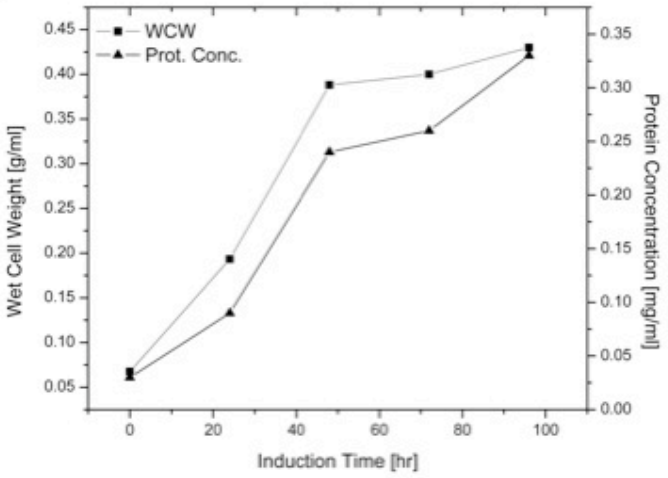

B.

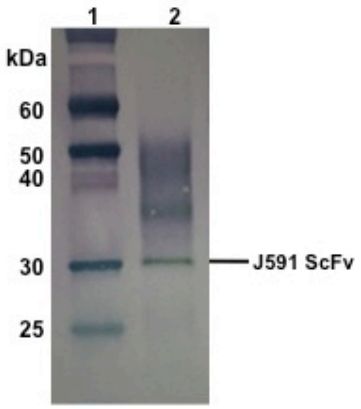

C.

J591 ScFv Mass Spectrometry Identified Peptides	
Sequence of Mass Match	**Position**
LLIYWASTR	52-60
STDTAYMELSSLR	205-21
ATLTVDK	198-204

Figure 2.2 J591 ScFv Fermentation Analysis.
A. P. pastoris cell growth and protein concentration during the induction phase of the J591 ScFv GS115 P. pastoris fermentation. Biomass was measured in wet cell weight and the protein concentration was determined by measuring the OD_{595} of the fermentation supernatant using the Bradford method. B. Western blot of fermentation supernatant probing for the poly his-tag. Lanes: 1) Protein standard and 2) J591 fermentation supernatant, the location of J591 ScFv is indicated in the figure. C. Mass Spectrometry analysis of 26 kDa SDS-PAGE gel band from the fermentation supernatant.

Western blot analysis was performed on the fermentation supernatant to confirm the presence of a 26 kDa his-tagged protein (Figure 2.2B). To confirm that the protein was the J591 ScFv, the 26 kDa band was excised from an SDS-PAGE gel and submitted for mass spectrometry analysis by the Cornell University Life Science Core Laboratories Center (Cornell University Ithaca, NY USA). Mass Spectrometry analysis positively identified three (LLIYWASTR, STDTAYMELSSLR, and ATLTVDK) of eleven tryptic peptides from the target, J591 ScFv, protein (Figure 2.2C).

2.4.3 J591 ScFv Purification

The fermentation supernatant was buffer exchanged by tangential flow filtration into 50 mM phosphate buffer pH 7.4 before IMAC purification. The purification was a three step chromatographic process (shown in Figure 2.3A): protein loading (flow thru), wash, and elution steps. Fractions were collected for each step and analyzed by SDS-PAGE (Figure 2.3B) and Western blot (Figure 2.4A). The protein concentration at each step is also given in the purification table in Figure 2.3C. The purified 26 kDa ScFv was verified by Western blot analysis probing for the his-tag shown in Figure 2.4A. As seen in the purification table in Figure 2.3C the protein concentration after purification was 0.09 mg/mL, which resulted in 2 mg of purified protein. Following purification the protein was collected and buffer exchanged into 50 mM phosphate pH 7.0 buffer for subsequent binding assays to a concentration of 1 mg/mL.

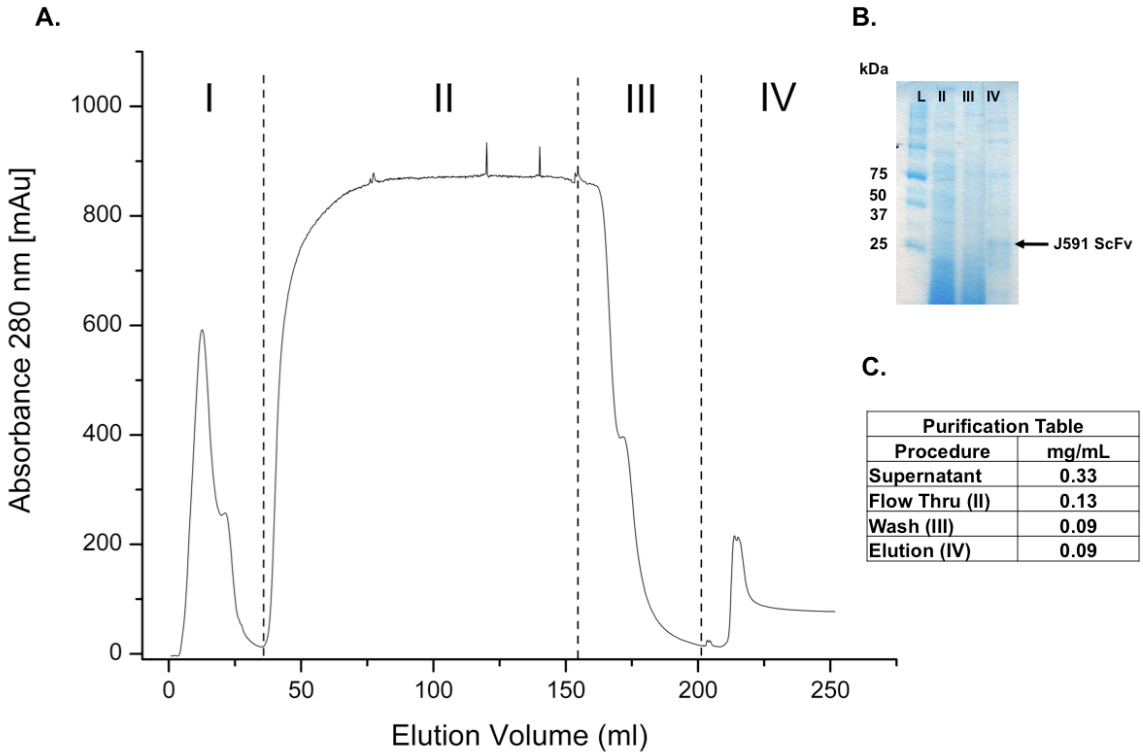

Figure 2.3 J591 ScFv Purification.
A*. IMAC chromatography profile of culture supernatant on a HisTrap Ni column at pH 7.4. Purification was completed in steps: I) Equilibration, II) protein loading (Flow Thru), III) wash, and IV) elution of J591 ScFv, protein elution took place at the peak of IV.* ***B****. SDS-PAGE Coomassie stained gel of the collected fractions of the purification. Lanes: L) standard, II) flow thru, II) wash, and IV) elution.* ***C****. Purification table with the protein concentrations of the supernatant and at each step of the purification process.*

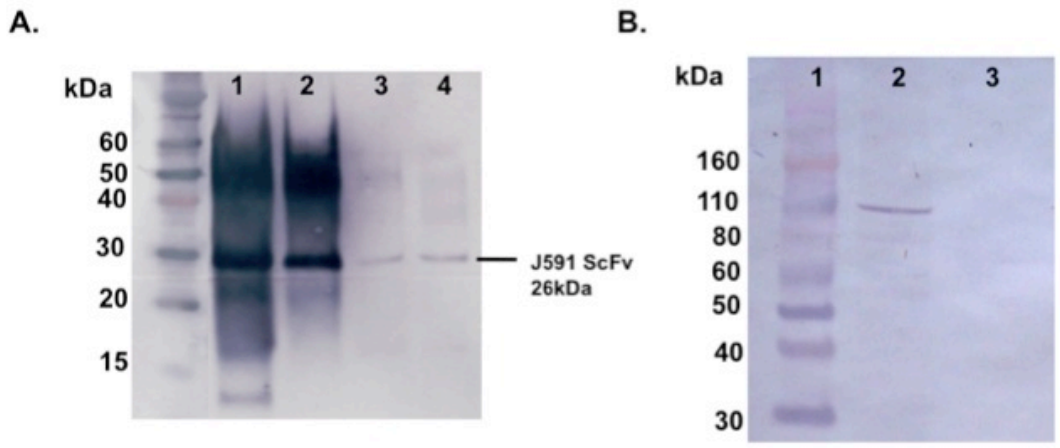

Figure 2.4 J591 Purification Western Blot and PSMA Immunoblot.
A*. Western Blot, probing for the 26 kDa his-tagged J591 ScFv, of the IMAC purification results Lanes: unlabeled: Novex protein standard, 1) buffer exchanged supernatant, 2) protein loading flow thru, 3) wash, and 4) eluted J591 ScFv (location indicated in figure).* ***B****. Immunoblotting assay of purified ScFv J591 and PSMA+/- cell lines. Lane 1) Ladder (Novex Sharp Standard LC5800 Life Technologies, Carlsbad, CA), Lane 2: PC3 PIP (PSMA+), and Lane 3: PC3 flu (PSMA-). 100 kDa PSMA detected and labeled by ScFv in lane 2.*

2.4.4 J591 ScFv Binding to cellular PSMA

Confirmation of the reactivity and specificity of the J591 ScFv to PSMA was conducted through an immunoblot analysis where J591 ScFv was used as the primary antibody. The immunoblot analysis was conducted on the cell lysate of PC3-PIP (PSMA+) and PC3-Flu (PSMA-) cells. The J591 ScFv detected a protein at 100 kDa in the PC3-PIP lysate, which corresponds to the molecular weight of PSMA (Figure 2.4B). The J591 ScFv identified a 100 kDa band in the PC3-PIP lysate but not from the PSMA-negative PC3-Flu lysate (Figure 2.4B). The positive detection in comparison to the negative control cell line establishes qualitatively the capability of the J591 ScFv to detect and bind to PSMA as seen in Figure 2.4B.

2.4.5 Binding J591 ScFv by LNCaP cells

The purified J591 ScFv was examined for its ability to bind PSMA expressed by LNCaP prostate cancer cells. An immunofluorescence assay was conducted towards this aim. The ScFv was labeled with Alexa Fluor 488 and was then incubated with permeabilized LNCaP prostate cancer cells for 1 h, to allow access to the intra- and extracellular PSMA. As seen in Figure 2.5A, LNCaP cells incubated with 10 μg/mL of ScFv showed intracellular staining. The ScFv labeling pattern indicates binding of the ScFv to PSMA. However the labeling of the ScFv is of lower intensity than that of the monoclonal antibody (Figure 2.5B), possibly due to a lower degree of labeling (4-9 moles of dye per mole of antibody for full IgG, compared to 2 moles of dye per mole of the J591 ScFv).

The J591 mAb showed more intracellular staining after 1 h than the ScFv indicating that the ScFv may not be internalized as efficiently as the mAb (Figure 2.5A&B). However, the immunoreactivity, as visualized by the membrane and internal cell membrane staining, of the ScFv with the LNCaP cells suggests that the J591 ScFv detects and is reactive to extracellular PSMA.

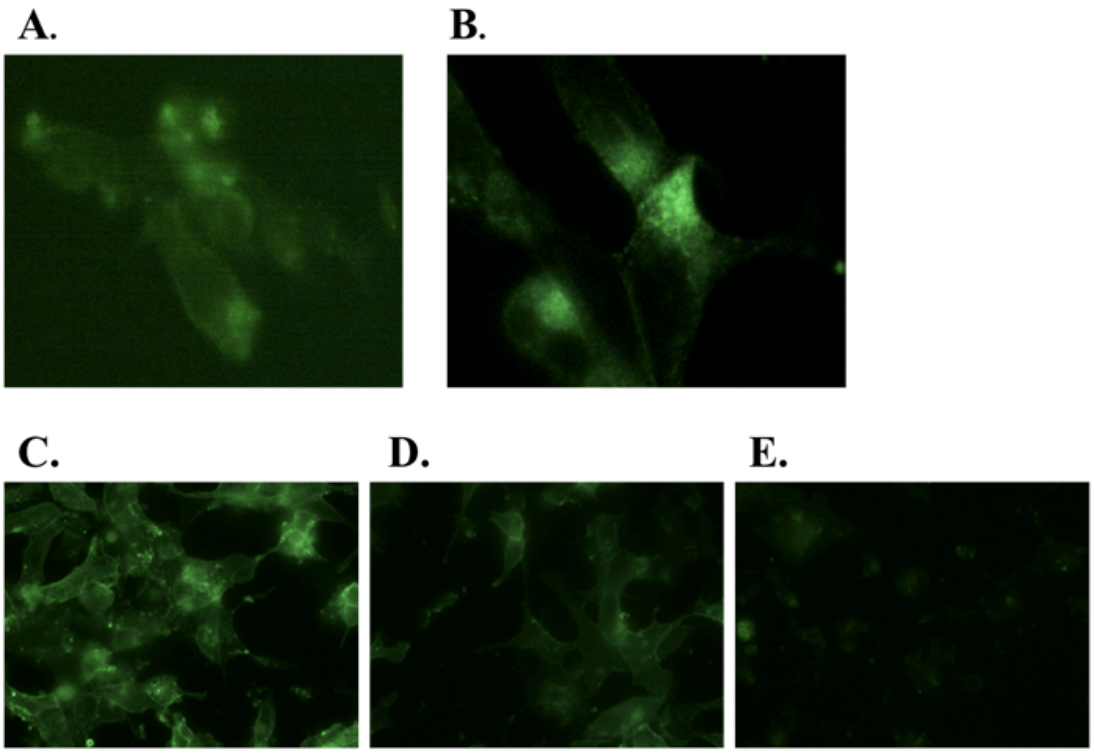

Figure 2.5 J591 ScFv Immunoflourescence and Competitive binding Assays.
Immunoflourescence (A&B): Internalization of ScFv in LNCaP cells. LNCaP cells incubated with 10 μg/mL of Alexa 488 labeled J591 ScFv (A) and 2 μg/mL of Alexa 488 labeled J591 mAb (B). Competitive binding Assay (C-E): Blocking the binding of the Alexa 488 labeled monoclonal J591 antibody with the ScFv version of the antibody. C. LNCaP cells stained with Alexa Flour 488 labeled monoclonal J591 (2 μg/mL). D. LNCaP cells incubated with 50 μg/mL of J591 ScFv followed by incubation with 2 μg/mL of labeled J591 mAb. E. LNCaP cells incubated with 10 μg/mL of unlabeled J591 mAb followed by incubation with 2 μg/mL of labeled J591 mAb.

2.4.6 Competitive Binding Assay

Characterization of the specificity and binding affinity of the J591 ScFv was carried out with a competitive binding assay with the fluorescently labeled monoclonal J591 antibody and the unlabeled J591 ScFv. To confirm that the J591 ScFv recognizes the same extracellar PSMA epitiope as the J591 mAb, the ScFv was used to block the binding of the J591 monoclonal antibody. The cells were permeabilized due to the PSMA+ cell lines (LNCaP/PC3-PIP) expressing PSMA both intra- and extracellularly.

First the fixed LNCaP cells were incubated with the single chain at 50 μg/mL, followed by incubation with 2μg/mL of the Alexa Fluor 488 labeled J591 mAb. As a positive control another assay was conducted in which the LNCaP cells were incubated with 10 μg/mL of unlabeled J591 mAb before incubation with the 2μg/mL of the labeled J591 mAb.

As shown in Figure 2.5D, when LNCaP cells were incubated with the 50 μg/mL of the J591 single chain for 1 h and then stained with 2 μg/mL of the J591 mAb, there is a reduction in fluorescence in comparison to the cells incubated with labeled J591 mAb alone (Figure 2.5C). As expected, the unlabeled mAb also blocked binding of the labeled mAb antibody and resulted in reduced staining of the PSMA expressing LNCaP cells (Figure 2.5E). Analysis of the fluorescence intensity found that blocking binding of the J591 mAb to the LNCaP cells with 50 μg/mL of ScFv caused a 52.4% decrease in fluorescence intensity as shown in Figure 2.6A&B. This reduction in fluorescence in the competitive binding assay indicates that the ScFv competes for the same extracellular PSMA epitope as the mAb; since the ScFv prevented the labeled mAb from binding to the LNCaP cells. In addition, the binding assay results demonstrate that the J591 ScFv can be expressed and purified from down-scale *P. pastoris* fermentation while maintaining its functionality in terms of PSMA binding *in vitro*.

(A)

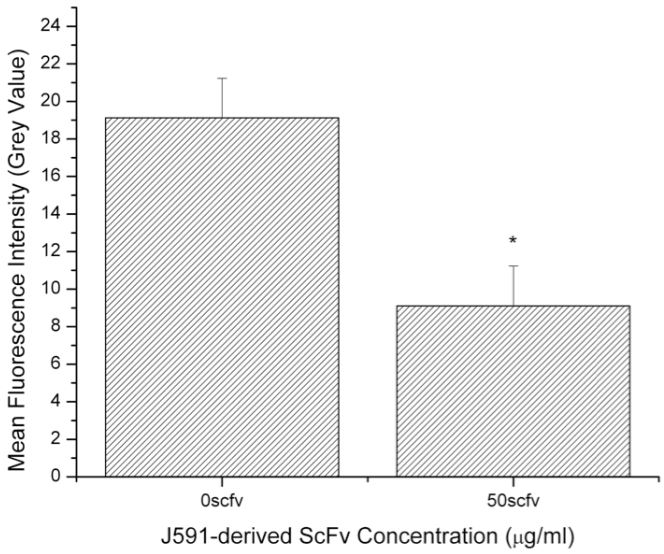

(B)

Image	ScFv concentration (μg/ml)	Mean Fluorescence Intensity (Gray Value)
A	0	19.13 ± 3.64
B	50	9.10 ± 3.70
Difference in Intensity		**10.03**
Magnitude Difference in Intensity		**2.10**

Figure 2.6 Competitive binding image analysis of J591 ScFv blocking binding of the fluorescently labeled J591 mAb.

*The mean gray values of the images were measured with the ImageJ software and used to determine the mean fluorescence intensity of images A and B from Figure 2.5, and the results are presented in the table (**B**) and graphically (**A**). The P value based on unpaired two-tailed t-test of the fluorescence data is 0.0285. The measured values were used to calculate the incremental change in intensity and the magnitude of difference in intensity between the two images.*

2.4.7 Flow Cytometry analysis of J591 ScFv binding specificity for PSMA expressing LNCaP cells

Flow cytometry analysis was used to confirm that the J591 ScFv is specific to PSMA. Two prostate cancer cell lines; the PSMA expressing LNCaP and non-PSMA expressing

were used for flow cytometry analyis. The J591 ScFv was conjugated with Alexa fluor 488 and incubated with the samples at a concentration of 10 µg/mL. As shown in Figure 2.7, flow cytometry analysis indicated that the ScFv binds selectively to PSMA expressing LNCaP cells, as shown by the shift in fluorescence in comparison to the negative control non-PSMA expressing PC3 prostate cancer cell line. These results further indicate that our J591 mAb derived J591 ScFv produced in *P. pastoris* is biologically functional and specific to PSMA.

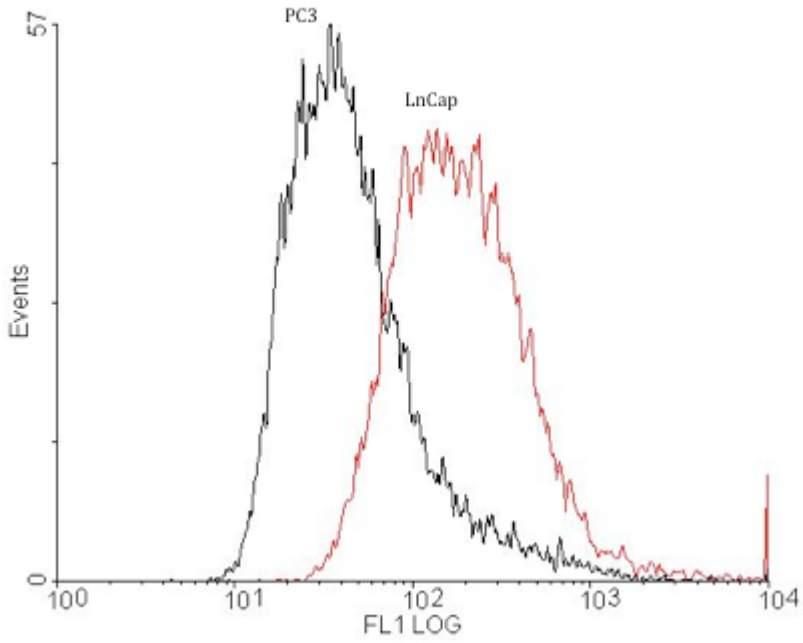

Figure 2.7 Flow cytometry binding analysis of J591 ScFv binding using PSMA expressing LNCaP cells (red) and non-PSMA expressing PC3 cells (black).
The J591 ScFv binds preferentially to the PSMA expressing cell line as shown by the shift in fluorescence value with the LNCaP cells compared to lower value of the fluorescence intensity measured from the PC3 cells.

We then examined whether the J591 ScFv could block the J591 Fab from binding to extracellular PSMA epitope. Protein blocking studies were conducted with the Alexa Fluor labeled J591 Fab and unlabeled J591 ScFv. LNCaP cells that were incubated first with the ScFv and then with the labeled Fab showed a reduction in fluorescence resulting

from reduced labeling of the Fab compared to the cells that were incubated with the Fab only (Figure 2.8). This is shown in Figure 2.8 as a shift to the left in the peak of the fluorescence intensity and a reduction in the number of positively stained cells. Compared with the positive control the pre-incubation of LNCaP cells with the J591 ScFv reduced the percentage of LNCaP cells labeled with the J591 Fab. In the absence of the ScFv 93.2% and 88.7% of the cells were stained with 5 μg and 10 μg Fab respectfully. However for the cells pre-incubated with the 25, 50, and 100 μg ScFv the percentages reduced to 34.7%, 31.4%, and 16.4% respectfully for cells incubated with 5 μg J591 Fab and 51.1%, and 45.1%, and 30.9% respectfully for cells incubated with 10 μg J591 Fab. Increasing the concentration of J591 ScFv during pre-incubation increases the inhibitory binding effect. For cells labeled with 5 μg J591 Fab pre-incubation with 25 μg ScFv reduced the percentage of positively stained cells by 58.5% compared with 61.8% and 76.7% reduction with 50 μg and 100 μg J591 ScFv pre-incubation respectfully. For cells labeled with 10 μg J591 Fab pre-incubation with 25 μg ScFv reduced the percentage of positively stained cells by 37.6% compared with 40.6% and 57.8% reduction with 50 μg and 100 μg J591 ScFv pre-incubation respectfully. The flow cytometry results indicate that the J591 ScFv is able to block binding of the J591 Fab, and thus detects the same extracellular epitope as the J591 mAb and is specific to PSMA. Further the inhibitory ability of the ScFv to block binding of the J591 Fab related to the concentration of the J591 ScFv.

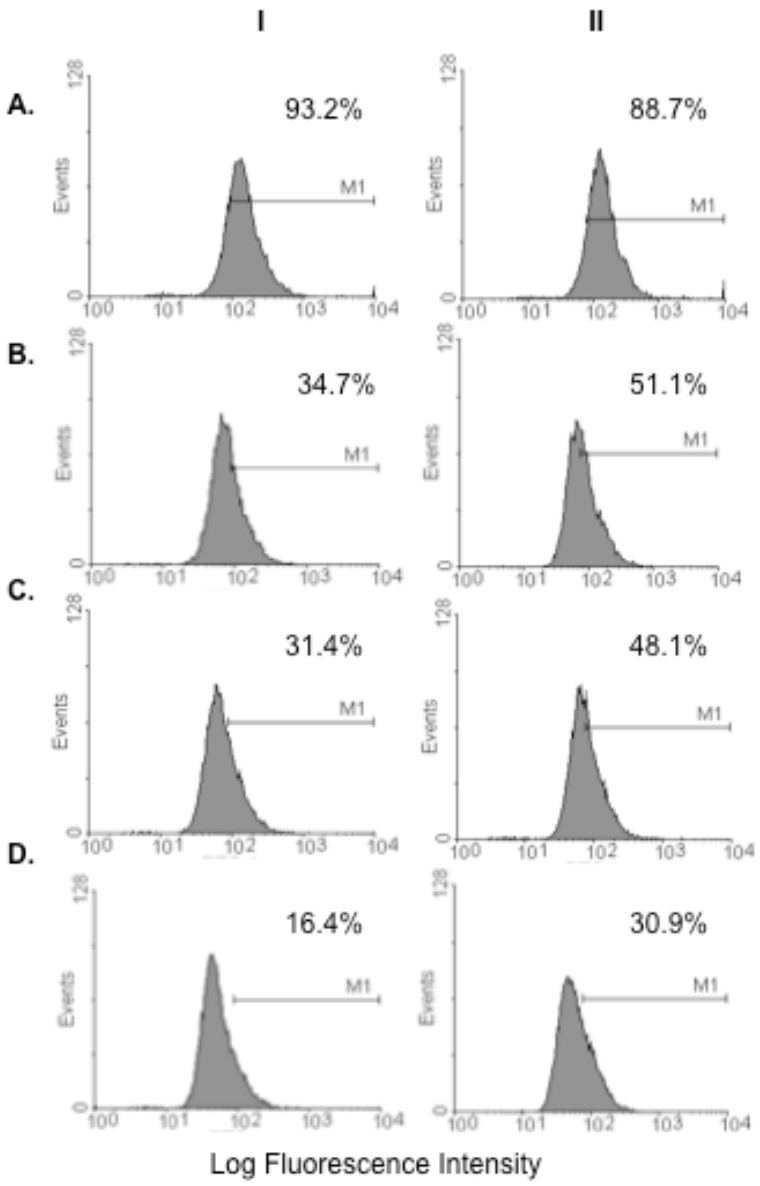

Figure 2.8 J591 Fab Binding Blocked by the J591 ScFv Flow Cytometry Studies.
The J591 ScFv was used to block binding of the J591 Fab and analyzed with flow cytometry. The assay was performed on LNCaP cells incubated with three concentrations of the J591 ScFv: A. 0, B. 25, C. 50, and D. 100 μg and then incubated with either 5 or 10 μg of Alexa Fluor 488 labeled J591 Fab. Results are presented as histograms of the log fluorescence intensities from 10^3 cells. The percentage of positively stained cells is indicated in each histogram.

2.4.8 Enzyme-Linked Immunosorbent Assay (ELISA)

Results of ELISA showed that the J591 ScFv bound to immobolized PSMA in a dose-dependent manner (Figure 2.9). The absorbance at 450 nm was plotted against the molar concentration of J591 ScFv added to each well and sigmaplot software (Systat Software, Inc., San Jose, CA) was used to fit the values to a sigmoidal curve Figure 2.9. The Kd value was calculated from the half maximal effective concentration (EC_{50}) as previously described [228, 229]. The affinity of eight individual J591 samples plates was described by a dissociation constant (Kd) that was determined to be 0.7 μM.

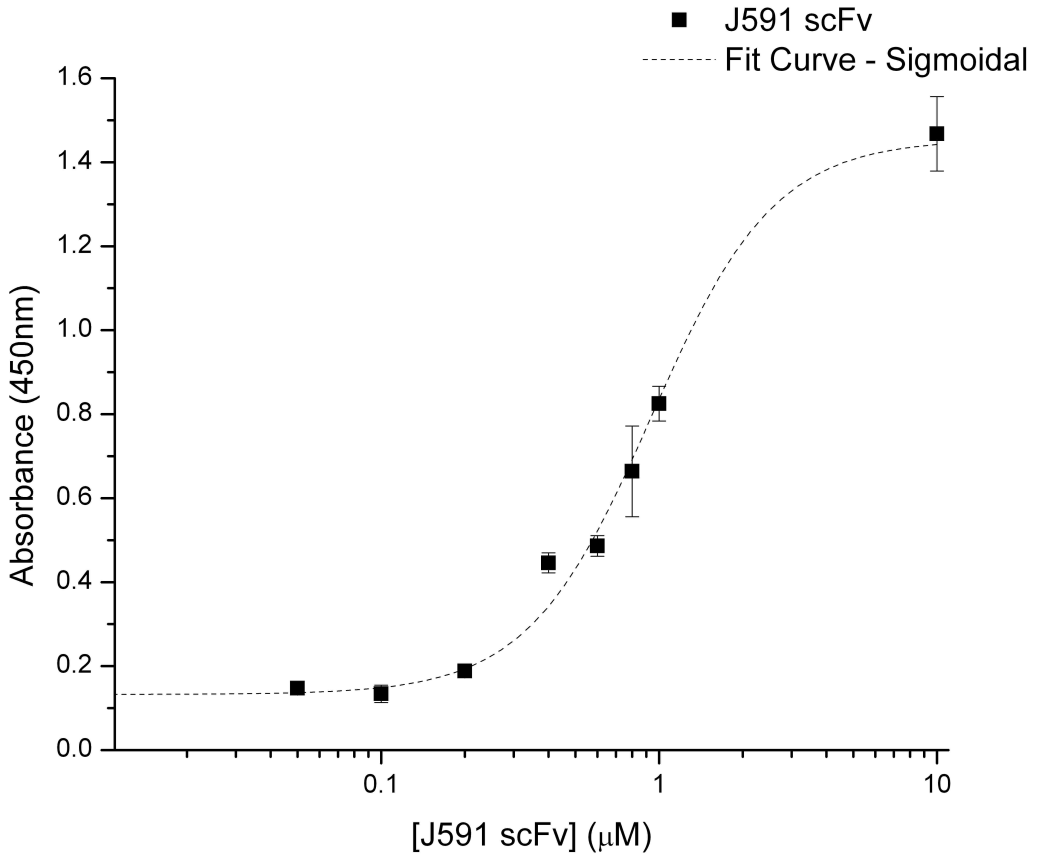

Figure 2.9 PSMA Binding Kinetics of J591 ScFv.
Binding of various concentrations of J591 ScFv to immobilized PSMA as measured by ELISA. 0.1 μg of PSMA antigen was immobilized in each well and incubated with varying concentrations of J591 ScFv. HRP conjugate was used for detection of bound J591 ScFv by TMB substrate and quantified by absorbance measured at 450nm. The OD 450 nm was plotted against the ScFv concentration and fit to a sigmoidal curve. The dissociation constant (Kd) was determined to be 0.7 μM.

2.5 Conclusion

We have designed, produced, and characterized a single-chain variable fragment (ScFv) derived from the prostate specific membrane antigen (PSMA) monoclonal antibody J591. The J591 ScFv was expressed in the supernatant of methanol-induced *P. pastoris.* Production of the ScFv was scaled-up using an online methanol control fed batch

fermentation, which makes it possible to grow the organism to high cell densities. A 2 L fermentation yielded 330 mg of total protein and 2 mg of purified J591 ScFv was collected following IMAC purification.

The results of flow cytometry analysis, competitive binding experimental assays, Western, and immunoblot analysis of the J591 ScFv confirmed the functionality, PSMA specificity, that the ScFv detects the same PSMA epitope as the J591 mAb, and the down-scale production capability of the ScFv reported in this study. The ScFv can be used to make fusion proteins such as for treatment and detection of cancer growth and metastasis. Our functional testing results confirm that our J591 ScFv may be also be suitable for development of targeted cancer treatment therapies in a wide variety of therapeutic delivery systems. This further suggests that the J591 ScFv not only binds specifically to PSMA but also competes for the

In summary, our J591 ScFv can be used to target the site of solid tumor neovasculature providing increased effectiveness of current treatment strategies. Future work will include optimization of the fermentation process for ScFv production, and quantification of the binding capacity of the ScFv, and further development and testing of ScFv based targeted therapies.

2.6 Acknowledgements

The authors thank Dr. Neil Bander of Weill Medical College of Cornell University, New York, NY for providing cell lines as well as guidance regarding this work. We would also like to that Vincent Navarro of Weill Medical College of Cornell University, New York, NY for providing invaluable assistance and input.

CHAPTER 3 J591 ScFv-PHA Synthase Fusion Protein for Targeted Vascular Occlusion

3.1 Abstract

A single chain variable fragment (J591 ScFv) that recognizes the extracellular glyco-protein prostate specific membrane antigen (PSMA) was fused with Polyhydroxylalkanoate (PHA) Synthase, the key enzyme for biosynthesis of polyhydroxyalkanoic acids (PHAs), from *Ralstonia eutropha* H16 and expressed in *Pichia pastoris*. The resulting protein contained two domains one for tumor targeting and the other domain for site-specific PHA polymer growth. Two gene constructs were formulated for the work: (1) the first contained the J591 ScFv and the PHA Synthase, *PhaC*, genes joined end-to-end and cloned into the pPIC9K expression vector and the (2) second consisted of the two genes joined by a flexible linker, the nucleotide sequence encoding the *PhaC* gene was codon-optimized for expression in *P. pastoris,* and the genes were cloned into the pPICZaA expression vector. Both constructs were cloned into and expressed in *P. pastoris* and 2 L methanol-induced *P. pastoris* fermentations were used for scaled-up production of the fusion protein constructs. With total secreted protein yields of up to 0.516 g L^{-1}, after 96 h of induction. The addition of a linker between the J591 ScFv and PHA Synthase proteins was determined critical to maintain functionality of the ScFv. The fusion protein was reacted with the monomer for polymer synthesis studies, polymer synthesis was confirmed via fluorescence microscopy of stained polymer granules and real-time polymerization was monitored via surface plasmon resonance. PSMA recognition of the J591 ScFv-PHA synthase fusion protein was confirmed via flow cytometry analysis, confocal studies examined particle binding, and internalization. The protein was conjugated to iron oxide nanoparticles, which could act as a potential delivery mechanism and allow for monitoring via Magnetic Resonance

Imaging, and our results showed that conjugation did not disrupt enzyme activity. This study demonstrates that functional J591 ScFv-PHA synthase fusion protein can be produced in *P. pastoris* for use in diagnostic and targeted therapeutic applications.

3.2 Introduction

The potential for targeting the neovasculature of tumors as a form of cancer therapy, has been firmly established in experimental studies [230-232]. Selectively cutting off the blood supply to solid tumors via a method that can be delivered swiftly and non-invasively is a promising avenue for cancer treatment. Treatment strategies that have been explored include targeted anti-endothelial vascular agents and non-targeted embolization using microspheres. Current vascular targeting treatment strategies use agents that are coupled to therapeutic drugs that could damage non-targeted tissues in the body. Further, non-targeted microspheres have been used in radio and chemo-embolization and have been successful in eliciting a cyto-reductive effect in liver and colorectal cancers [233]. However, the majority of the microspheres in use are not specifically targeted to tumors, relying instead on administering the particles directly into the feeding arteries of the tumor [233]. Toxicity to normal tissue and the non-specificity of current options highlight the need for the development effective and minimally invasive targeted embolization treatment options that result in fewer complications [234]. Here we have developed a fusion protein, composed of a targeting single chain antibody and polymer-synthesizing enzyme, for selective occlusion tumor neovasculature via targeted nanoparticles. This is a novel approach to targeted vascular occlusion, as a form of solid tumor cancer therapy, via the introduction of antibody targeted emboli. The targeting moiety, J591 ScFv, was recently developed and characterized in our previous

work, and is specific to Prostate Specific Membrane Antigen (PSMA)[105]. PSMA is a solid tumor neovasculature marker for multiple non-prostatic solid tumors, including gastric and colorectal cancer, without expression by the tumor or normal vascular endothelium [161, 162, 165-169]. Evidence suggests that PSMA expression in associated neovasculature may be related to the degree and nature of angiogenesis, and that PSMA expression is greatest in high-grade and hormone-insensitive cancers [162, 170]. The second component of the fusion protein is Polyhydroxyalkanoate (PHA) synthase, the sole enzyme require to initiate the synthesis of the biocompatible polyhydroxybutyrate (PHB) polymer [190]. PHA synthase initiates the conversion of (R)-3-hydroxyacyl-CoA thioester substrate to PHAs with the concomitant release of CoA [160]. For this study we cloned the PHA synthase gene from *Ralstonia eutropha* H16 [235].

The methylotrophic yeast, *P. pastoris*, expression system was used for expression of the J591 ScFv-PHA Synthase fusion protein under the control of the methanol inducible alcohol oxidase 1 (*AOX1)* promoter [236]. There are several advantages of the *P. pastoris* expression over other bacterial expression systems, like *Escherichia coli.* These include the ability to grow high cell densities, produce recombinant proteins on the order of mg to g L^{-1} concentrations, and unlike bacterial, *P. pastoris* has the capability to perform post translation modifications typically associated with higher eukaryotes [237-239]. Thus eukaryotic proteins synthesized in *P. pastoris* are more likely to be properly folded, processed, and form active molecules. This is particularly relevant for this study as we are expressing a single chain variant of a mouse monoclonal antibody.

To accomplish targeting and occlusion via the J591 ScFv-PHA Synthase Protein we propose that: in situ growth of PHB polymer catalyzed by PHA synthase from the 3HBCoA monomer substrate, distributed within solid tumor microvasculature by targeted antibody-conjugated nanoparticles, will cause tissue ischemia, resulting in tumor necrosis. For this approach the J591 ScFv-PHA synthase fusion protein would be conjugated to nanoparticles, administered intravenously for selective tumor microvasculature accumulation, and the substrate would be delivered to the accumulated particles for formation of PHB polymer to selectively occlude the tumor microvasculature. The nanoparticles investigated for use here are superparamagnetic iron oxide nanoparticles (SPIONs). SPIONs are a well established MRI contrast agents and will allow for efficient treatment monitoring [240, 241]. Alternatively, the fusion protein may be administered for synthesis PHB polymer from the substrate to cause targeted tumor vasculature blockage.

3.3 Materials and Methods

3.3.1 Organisms and Strains

Escherichia coli DH5α were used for cloning of the J591 ScFv and PhaC nucleotide sequences in the pPIC9K and pPICZaA plasmids (V17520, Life Technologies, Carlsbad, CA USA). *P. pastoris* strains used for protein expression include the GS115 and KM71 from Life Technologies (Pichia Expression Kit, Version M, Life Technologies, Carlsbad, CA USA) and BG11 and Superman5 strains from Biogrammatics (Biogrammatics, Inc. Carlsbad, CA).

3.3.2 Cell lines and Cultures

Mammalian cancer cell lines used in this study include the prostate cancer cells lines LNCaP, PC3, and PC3-PIP and colon cancer cell line HT29 (American Type Culture Collection (ATCC), Manassas, VA). LNCaP cells were cultured in RPMI 1640 medium F12-K (Life Technologies, Carlsbad, CA USA) supplemented with: 10% (v/v) fetal bovine serum (FBS) and 1% penicillin–streptomycin (P/S, 100 units mL^{-1} penicillin, and 100 μg/mL streptomycin) and the other cell lines were cultured in Minimum Essential Media (Life Technologies, Carlsbad, CA USA) supplemented with: 1% penicillin–streptomycin respectively at 37^{o}C and 5% CO_2 in a humidified incubator.

3.3.3 Gene Constructs

Two gene constructs were formulated for the work: (1) the first contained the J591 ScFv and the PHA Synthase, *PhaC*, genes joined end-to-end and cloned into the pPIC9K expression vector and the (2) second consisted of the two genes joined by a flexible linker, the nucleotide sequence encoding the *PhaC* gene was codon-optimized for expression in *P. pastoris,* and the genes were cloned into the pPICZaA expression vector.

Construct 1: J591-phaC	
Plasmid	Strains, Phenotype
pPic9K	KM71 (Mut^S)
	GS115 (Mut^+)
Construct 2: J591-linker-phaC (codon optimized)	
Plasmid	Strains
pPICZaA	BG11, MutS
	Superman5, Mut+
Linker sequence:	S G G G G S G G G G S G G G G S

Table 3.1 Construct details for the two constructs used to clone the J591 PHA Synthase fusion protein.

3.3.4 Gene Construct 1: J591PhaC-pPIC9K with Overlap Extension PCR

The genes encoding the J591 Scfv and PHA Synthase (PhaC) enzyme from *Ralstonia Eutropha* were fused using overlap extension PCR as outlined in the three steps below with the primers listed in Table 3.2:

Step 1: First, the J591 and PhaC gene sequences were amplified individually from plasmids containing the genes. This step constructed the DNA fragments that were combined to create the hybrid gene. Following the amplification of the gene fragments the PCR products were visualized and confirmed by gel electrophoresis. The PCR reactions were then purified to remove the primers and plasmid DNA using the QIAquick PCR purification kit (Qiagen, Hilden, Germany). The concentration of the PCR products were determined by absorbance measurements at 260 nm, obtained using a NanoDrop ND-1000 (Thermo Scientific Waltham, MA USA).

Step 2: Next, the fragments were combined in a single PCR reaction. Before addition of the primers to the PCR reaction, the reaction was run with the fragments for three cycles for the overlap reaction to occur. The primers (J591 forward and PhaC reverse) were then added to the reaction for the remaining cycles.

Step 3: Following the final amplification step the PCR product was visualized by gel electrophoresis. The OE band was gel purified using the QIAquick PCR purification kit (Qaigen).

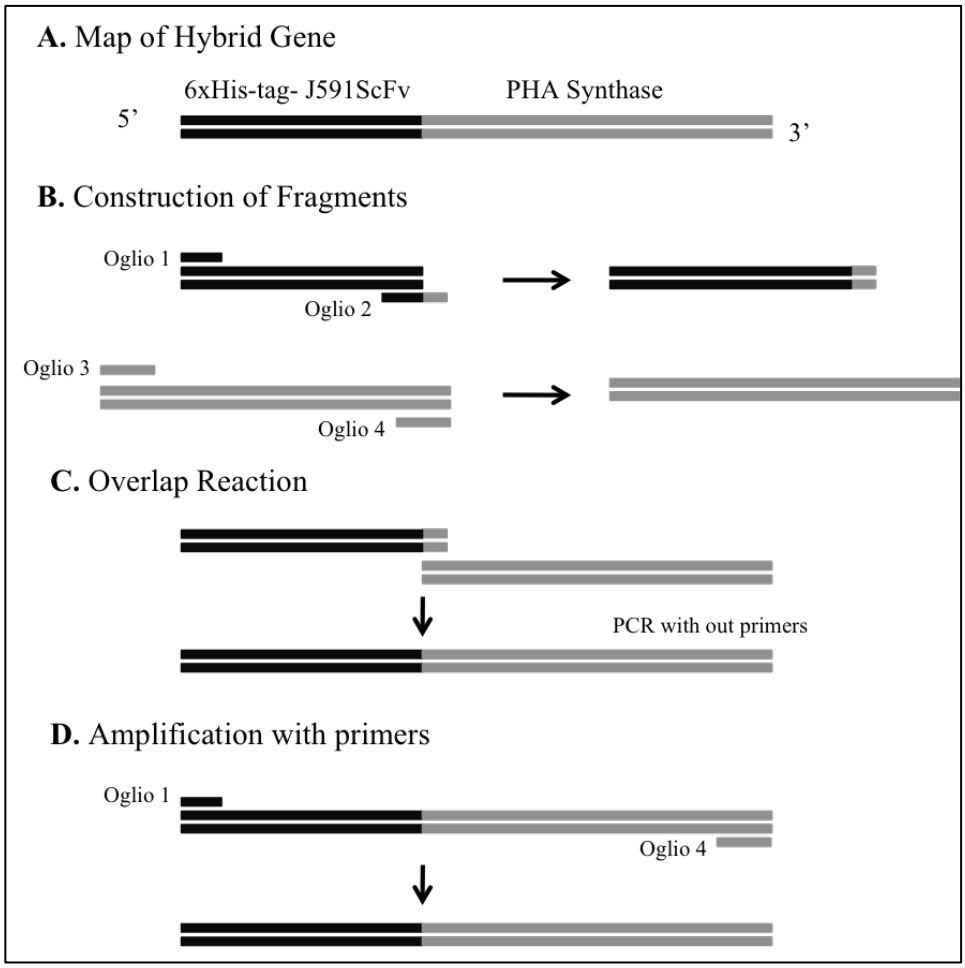

Figure 3.1 Overlap Extension PCR to construct J591 ScFv-PhaC hybrid gene.
(A) Map of the hybrid J591 ScFv-PhaC gene that was constructed. (B) PCR amplification of the J591ScFv and PhaC gene fragments from their respective plasmids. (C) Overlap reaction with the fragments from B. The PCR reaction cycles are run for 3 cycles without primers. (D) PCR was then used to amplify the overlap reaction with Oligios 1 and 4.

A MJ Research PTC-2000 Peltier Thermal Cycler (MJ Research, Quebec, Canada) was used for all PCR steps. The primers were designed to compliment the J591 ScFv and PhaC gene sequences, Table 3.2, the PCR conditions for amplification were optimized and occurred in three steps (1) initial denaturing of the plasmid DNA for 10 min at 95˚C, (2) followed by 95˚C for 1 min, 56˚C for 1 min, and 72˚C for 1 min cycled 30 times, and a (2) final extension at 72˚C for 10 min. The overlap extension PCR conditions used occurred in three steps (1) initial denaturing of the plasmid DNA for 10 min at 95˚C, (2)

followed by 95˚C for 1 min, 56˚C for 1 min, and 72˚C for 7 min cycled 30 times, and a (2) final extension at 72˚C for 10 min. The fragments and overlap reaction were visualized via gel electrophoresis, Figure 3.3.

Primers	
J591 ScFv	
Forward Primer	5'-TCT TCT CTC GAG AAA AGA GAG GCT GAA GCT -3'
Reverse Primer	5'-**CTT TGC CGG TCG CCA T**AG ATG AGA CAG TCA ACA AAG-3'
PhaC	
Forward Primer	5'-ATG GCG ACC GGC AAA GGC G-3'
Reverse Primer	5'-TCT TCT GAA TTC TCA TGC CTT GGC TTT GAC GTA TCG-3'

Table 3.2 J591 ScFv and PhaC Primers.
These primers were used for the amplification and overlap extension PCR reactions of the J591 Scfv and PhaC gene sequences. The bolded nucleotides of the J591 ScFv reverse primers are the beginning of the PhaC gene.

The fused gene sequences were sub-cloned into the Invitrogen TOPO TA plasmid for replication: ratio 5:1 worked best for TOPO cloning (Life Technologies, Carlsbad, CA). Blue and white screening was used to confirm integration into the TOPO vector. *Escherichia coil* DH5α was used to assemble the J591 ScFv-PHA synthase fusion protein genes in the pPIC9k plasmid, a 9.6Kb *Pichia Pastoris* expression vector (Life Technologies, Carlsbad, CA). The pPIC9k-J591 ScFv-PHA synthase construct was then cloned into the His Strain *P. pastoris* GS115 for expression. Preparation of competent *P. pastoris* cells and transformation procedure was done according to protocol developed by Lin-Cereghino *et al*.[242].

3.3.5 Gene Construct 2 pPICZαA-J591-linker-PhaC

PCR amplification was used to generate J591 ScFv sequence with flanking restriction sites, *XhoI* and *SacII*, for subsequent cloning into the pPICZαA vector. The phaC gene

was codon optimized for expression in *P. Pastoris* and provided as a gene fragment, GBlock (Intergrated DNA Technologies (IDT), Coralville IA). The amplified J591ScFv gene and PhaC gene block were sequentially cloned into the pPICZαA expression vector, respectively. The resulting plasmid included the J591 ScFv and PhaC genes joined by a flexible linker.

3.3.6 Transformation, Selection, and Expression in P. Pastoris

Preparation of competent cells and transformation of *P. pastoris* was performed in accordance with Lin-Cereghino's previously reported condensed protocol [218]. Briefly the transformation was as follows: Approximately 4 μL (50-100 ng) of linearized plasmid was mixed with 40 μL of electrocompetent *P. pastoris* GS115, KM71, BG11, or Superman5 cells. Plasmid and cells were transferred to a 0.2-cm electroporation cuvette. Electroporation was carried out in a Bio-Rad Gene Pulser with charging voltage of 1500 V, capacitance of 25 μF, and resistance of 200 Ω. Immediately after electroporation, 1 mL of ice-cold 1 M sorbitol was added to the cuvette, and 200, 100, 50 and 10 μL aliquots were spread onto minimal dextrose (MD) plates lacking histidine for construct 1 clones and Yeast Extract Peptone Dextrose Sorbitol Medium (YPDS) plates containing either 100, 200, 300 μg ml^{-1} Zeocin for construct 2 clones (Pichia Manual, Life Technologies, Carlsbad, CA). The plates were incubated for 2 days at 30°C for selection of transformants.

The pPIC9K-J591 ScFv-PhaC and pPICZαA-J591-linker-PhaC constructs expressed the J591 ScFv-PHA synthase protein under the control of the strong methanol-inducible alcohol oxidase (AOX1) promoter [219]. For the pPIC9K-J591 ScFv-PhaC construct four (His^+Mut^+) transformants and four KM71 (His^+Mut^S) transformants were screened

for the production of J591 ScFv-PHA Synthase. For the pPICZαA-J591-linker-PhaC construct sixteen colonies eight BG11 (His^+Mut^S) and eight Superman5 (His^+Mut^+) were screened. Single colonies were used to inoculate 5 mL Yeast Extract Peptone Dextrose (YPD) [1% (w/v) yeast extract (EMD Millipore Chemicals, Darmstadt, Germany), 2% (w/v) peptone (Difco Laboratories Inc., Franklin Lakes, NJ USA), and 2% (w/v) dextrose (VWR Chemicals, West Chester, PA, USA)] and grown overnight at 30ºC with vigorous shaking. Each 5 mL culture was used to inoculate 25 mL of Buffered Minimal Glycerol (BMGY) [1% (w/v) yeast extract, 2% (w/v) peptone, 100 mM potassium phosphate pH 6.0, 1.34% (w/v) YNB (Becton, Dickinson and Co., Franklin Lakes, NJ, USA), 4 x 10^{-5} % (w/v) biotin (Sigma-Aldrich, St. Louis, MO, USA), and 1% (v/v) glycerol (VWR Chemicals, West Chester, PA, USA) at pH 6.0 in a 250 mL baffled flask adjusting them to an OD_{600} of 1.0. They were then grown at 30°C in a shaking incubator (250–300 rpm) until the culture reached an OD_{600} of 2-4. Cells were then harvested by centrifuging at 3500 x g for 10 min at room temperature. To induce expression, the supernatant was decanted and the cell pellet was resuspended in 10 mL of Buffered Minimal Methanol (BMMY) [100 mM potassium phosphate pH 6.0, 1.34% (w/v) YNB, 4 x 10^{-5} % (w/v) biotin, and 0.5% (v/v) methanol] at pH 6.0 and grown at 30°C for 96 h. 0.5% methanol was added for induction every 24 h. Following 96 h of induction the optical density and protein concentration of the cultures were measured and supernatants were analyzed through SDS-PAGE Coomasie and Western blotting.

3.3.7 Scaled-Up Expression in 2 L Fermentation

Fermentations were performed following our previously published protocol for single-chain Fv production in *P. pastoris* [220]. A single *P. pastoris* transformant was used to

inoculate 5 mL YPD and the culture was grown overnight at 30°C. The overnight culture was diluted to an OD_{600} of 0.01 in 100 mL BMGY [1% (w/v) yeast extract, 2% (w/v) peptone, 100 mM potassium phosphate, pH 6.0, 1.34% (w/v) YNB, 4 x 10^{-5} % (w/v) biotin, and 1% (v/v) glycerol] in a 250 mL baffled flask and incubated at 30°C until the culture reached an OD_{600} of approximately 20. This culture was used to inoculate 1.1 L of fermentation media.

A 2 L working volume was used to conduct fermentations using a Bioflo 300 (New Brunswick Scientific, Edison, NJ USA) interfaced with AFS-Biocommand Bioprocessing software version 2.6 (New Brunswick Scientific) for data acquisition and operational control. A 1.1 L starting volume of modified basal salts medium [221] [0.23 gL^{-1} $CaSO_4 \cdot 2H_2O$, 4.55 gL^{-1} K_2SO_4, 3.73 gL^{-1} $MgSO_4 \cdot 7H_2O$, 1.03 gL^{-1} KOH, 6.68 mLL^{-1} H_3PO_4, and 5 % (v/v) glycerol] and 0.5 mL Antifoam 204 (Sigma-Aldrich, St. Louis, MO) was sterilized inside the reactor. Ammonium hydroxide [15% (v/v)] was used as a pH control agent and nitrogen source. The pH was measured with an Accumet pH electrode (Fisher Scientific). Prior to inoculation 4.35 mL L^{-1} of PTM_1 trace salts (24 mM $CuSO_4$, 0.53 mM NaI, 19.87 mM $MnSO_4$, 0.83 mM Na_2MoO_4, 0.32 mM boric acid, 2.1 mM $CoCl_2$, 0.14 mM $ZnCl_2$, 0.23 M $FeSO_4$, and 0.82 mM biotin) were added aseptically.

The fermentation was inoculated with the 100 mL overnight culture in BMGY. The fermentation was maintained at 25°C and a pH value of 4.0 for GS115 throughout the batch and induction stages. Dissolved oxygen (DO) levels were maintained at 40% of saturation and controlled by a DO cascade of agitation (maximum of 1000 rpm) and supplemented with pure oxygen as required. Oxygen concentration was measured with an InProb6110/220 electrode (Mettler-Toledo GmbH, Germany).

The batch phase was continued until the glycerol was consumed, indicated by a sharp increase in the DO. Following the batch phase the culture was induced with a methanol feed (100% methanol with 12 mL PTM_1 L^{-1} methanol) initiated by a closed loop Proportional-Integral-Differential (PID) control scheme. The control scheme consisted of the BioFlo 3000, a methanol probe (Raven Biotech, Vancouver, Canada), a PID controller Cni852-C4EI (Omega Engineering, Stanford, CT USA), and a Masterflex variable speed pump head (Cole-Parmer Instruments, Vernon Hills, IL USA). The methanol sensor was interfaced with Windmill Logger software (Windmill Software, Manchester, UK) for data acquisition. The methanol value was maintained at a value of 0.1 g L^{-1} for the entire 96 h induction phase. Samples were taken at 24 h intervals and the wet cell weight and protein concentration was measured for each time point.

3.3.8 Flow Cytometry

LNCaP (PSMA+) prostate epithelial carcinoma cells and HT29 (PSMA-) colon epithelial adenocarcinoma cells were cultured to 80% confluence for flow cytometry analysis. The cells were then collected and resuspended in phosphate buffer (PBS) pH 7.5. The fermentation supernatant containing the J591 ScFv-PHA synthase protein at a concentration of 0.7 mg mL^{-1} was fluorescently labeled with the Alexa Fluor 488 according to the manufacture's protocol (Life Technologies, Carlsbad, CA USA). The degree of labeling was calculated as the moles of dye per mole of protein in accordance with the manufactures' prescribed protocol using the molecular weight of the protein and the extinction coefficient calculated using the ProtParam software (ExPASy Bioformatics Resource Portal). Absorbance measurements of the labeled protein at 494 nm and 280 nm were taken using a Nanodrop ND-1000 (Thermo Scientific Waltham, MA USA). The

calculated degree of labeling of the J591 ScFv-PHA Synthase fusion supernatant was 0.382 moles of dye per mole of protein. 500,000 cells of either LNCaP or PC3 cells in PBS were incubated with 10 μg of labeled J591 ScFv for 30 min at 4°C. The cells were then washed twice with 1 mL PBS via centrifugation at x 300 g, and then resuspended in 500 μL PBS with 1% paraformaldehyde. Flow cytometry was carried out using a Beckman Coulter Epics XL-MCL Flow Cytometer (Beckman Coulter, Brea, CA USA). Flow cytometry data were analyzed using WinMDI software version 2.9 (Scripps Research Institute, La Jolla, CA, USA).

3.3.9 J591 ScFv-PHA Synthase Granule Cell Binding Studies

Cellular binding studies were used to examine binding specificity of PHB granules produced by the J591 ScFv-PHA Synthase fusion protein. To prepared PHB granules stained with Nile Red, 1 mL of the fermentation media was filtered through a 0.22 μm filter and then reacted with 5 mM 3 HB-CoA for 20 min at 30°C. The reaction was then mixed with 5 μl of Nile Red to stain the PHB granules. To extract the particles the reaction was spun down for 20 min at 16,000 x g, resuspended in 1 mL of PBS, and then sonicated briefly to break up aggregates.

For imaging studies, PC3-PIP (PSMA+) and PC3 (PSMA-) cells were grown to confluence in 35 mm glass bottom petri dish. The cells were washed with PBS then incubated with 100 μL of nile red stained J591-PHA-PHB granules and incubated for 30 min at 37°C in a CO_2 incubator. Following incubation the cells were washed 3 times with PBS and then fixed with 4% paraformaldehyde in PBS for 10 min at room temperature, before laser scanning confocal imaging using a Zeiss LSM 710 confocal microscope (Zeiss, Germany).

3.3.10 Polymerization of (R)-3-hydroxylbutyrl-CoA and Dynamic Light Scattering

(R)-3-hydroxylbutyrl-CoA (3HBCoA) was synthesized by reacting β-butyrolactone with free coenzyme A (CoA), as previously described by Simon et. al [243].[244] 100 mg of coenzyme A lithium salt (Affymetrix, Santa Clara, CA) was dissolved in 5 mL of 200 mM $KHCO_3$ (Sigma-Aldrich) solution. The solution was placed in ice bath with slow stirring and 106 μL of β-butyrolactone (Sigma-Aldrich) was slowly dripped in to a final molar ration of CoA to lactone of 1:10 and allowed to react for 2 h. Excess unreacted lactone was extracted with diethyl ether by the addition of one volume of ether, mixing the solution via vortex, and the discarding the upper phase was discarded. This procedure was repeated twice before lyophilizing for at least 2 h. The synthesized 3HBCoA was stored at -20°C and reconstituted in dH_2O before use.

To confirm that the J591 ScFv-PHA synthase protein maintains polymerization activity the fermentation supernatant was concentrated to 1 mg ml^{-1} and incubated with 10 mM 3HBCoA overnight and 7.5 % Tween 20. Particles were attained with Nile Red 0.5 mg mL^{-1} in DMSO. Imaged using fluorescence microscope.

Dynamic light scattering (DLS) measurements of PHB granules were taken using a Zetasizer Nano-ZS (Malvern Instruments Ltd, Worcestershire, UK). The particle size was calculated as the average of six consecutive measurements recorded at 25 ºC.

3.3.11 Real-time In-vitro PHB synthesis monitored via Surface Plasmon Resonance SPR

Surface plasmon resonance (SPR) previously described[245]. Gold substrates for SPR were prepared by electron-beam evaporation of an adhesive layer of chromium (10Å) and high purity gold (500Å) onto glass microscope slides (Fisher Scientific, Rochester, NY).

The gold surface was functionalized with Ni-NTA for immobilization of his-tagged fusion protein via a self-assembled monolayer (SAMs)[246]. SAM functionalization of the chip consisted first rinsing the gold substrate with either absolute ethanol or dichloromethane followed by several solution incubation steps, all at room temp. First the substrate was immersed in 0.002 M solution of 16-mercapto-hexadecanoic acid in ethanol and incubated overnight at room temp, rinsed with ethanol, and dried with nitrogen. The resulting substrate contained a carboxylic acid SAM and was immersed in a solution of 0.1 M trifluoroacetic acid (Sigma-Aldrich) and 0.2 M triethylamine (Sigma-Aldrich) in anhydrous N, N-dimethyformide (Sigma-Aldrich) for 20 min to generate interchain anhydrides. The substrate was then rinsed with dichloromethane, dried with a stream of nitrogen, immersed in a solution of N, N-bis(carboxymethyl)-L-Lysine hydrate (Sigma-Aldrich) and 0.01 M triethylene glycol monoamine (Molecular Biosciences, Boulder, CO) for 30 min, rinsed with ethanol, and dried with a stream of nitrogen. Ni-NTA groups were added to the SAM by immersion in a solution of nickel chloride for 1 h.

SPR measurements were performed at room temperature with a Reichert SR7000 Surface Plasmon Resonance Refractometer (Reichert Inc. Depew, NY). Buffer exchanged J591 ScFv-PHA Synthase fermentation supernatant was concentrated to 1 mg ml^{-1} and diluted in 1 ml of 50 mM Tris-HCL pH 7.5 to 5, 1, 0.5 μM for SPR experiments. Protein was immobilization on the NTA-SAM consisted of sequential injection of 40 mM Nickel Chloride solution at 50 μL min^{-1} for 5 min followed by the protein at flow rate of 25 μL min^{-1} for 10 min at room temperature. The surface was washed between steps with 50 mM Tris-HCL Buffer (pH 7.5) applied for 5 min a flow rate of 50 μL min^{-1}. For PHB

synthesis 0.5 mM 3HBCoA substrate was applied at 10 μL min^{-1} for 30 min. Protein immobilization and polymer growth resulted in a shift in the resonance angle.

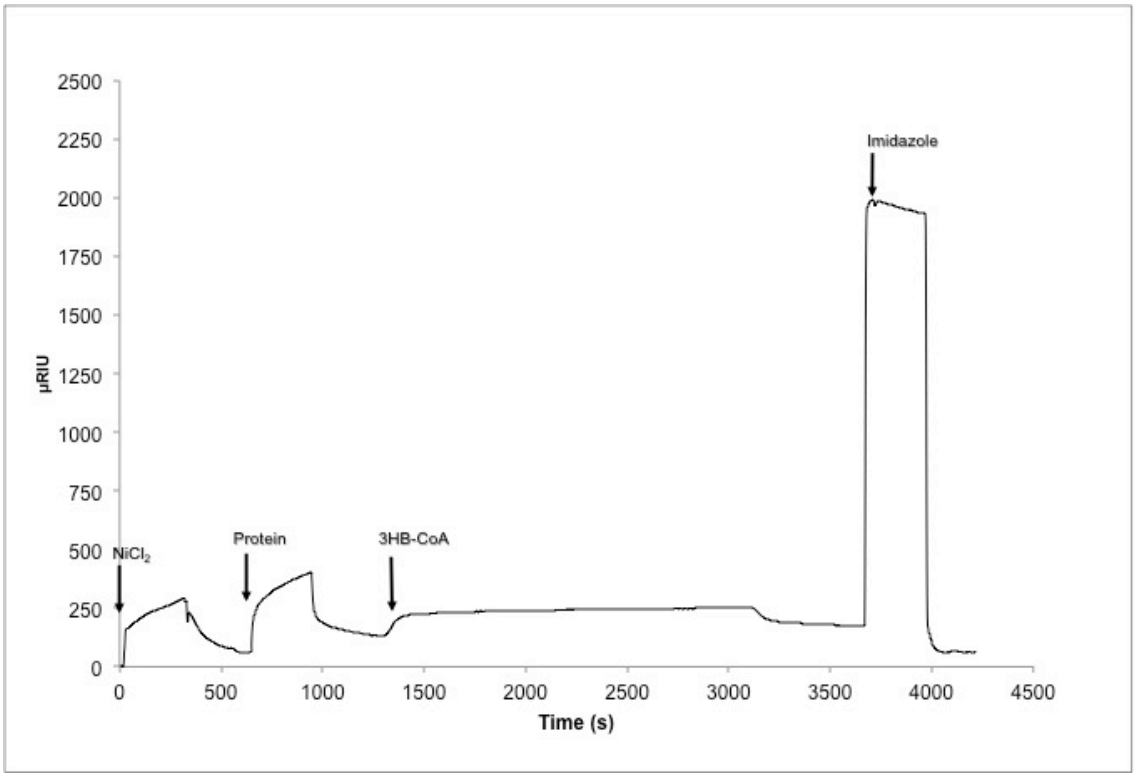

Figure 3.2 SPR Sensor gram for J591 ScFv-PHA Sythanse binding and 3HB-CoA Polymerization.

SPR Sensor gram showing the chip functionalized with $NiCl_2$ to create Ni-NTA functional groups, binding of the J591 ScFv-PHA Synthase Protein via the C-terminal histag binding to the Ni-NTA groups, 3HB-CoA monomer polymerization reaction initiated by the PHA synthase enzyme, and dissociation of the protein and PHB polymer from the surface by free imidazole. This experiment was run with three concentrations of J591-PHA supernatant 0.5, 1, and 5 μM, 1mM, the sensor gram above is taken from the 0.5 μM concentration run.

3.3.12 Purification

Anion exchange chromotography on a 5 mL Q Sepharose column (HiTrap QXL, GE Healthcare Bio-Sciences Corp. Piscataway, New Jersey) was used to purify the J591 ScFv-PHA Synthase fusion protein. For purification fermentation supernatant was collected via centrifugation following induction and buffer exchanged via dialysis in binding buffer (20 mM sodium phosphate buffer pH 8.0). All ion exchange

chromatography steps were carried out using an ÄKTA Explorer (GE Healthcare Bio-Sciences Corp. Piscataway, New Jersey). First the column was equilibrated with 5 column volumes of binding buffer then the buffer exchanged supernatant was loaded (2 mL min^{-1}) onto the column. After loading, the column was washed with 5 column volumes of the binding buffer. To elute the protein from the column two elution methods were used. (1) The elution buffer (20 mM phosphate buffer and 1 M sodium chloride pH 8.0), at 50% concentration, was then applied to the column (3 mL min^{-1}) for the elution step and the elution fraction was collected. (2) The elution buffer was added starting at a concentration of 0 to 100% over 10 column volumes, and each 5 mL column volume was collected. The NaCl was eliminated from the eluted fraction via buffer exchange into 20 mM PBS (pH 8.0) using an Amicon Ultra-15 10 kDa centrifugal filter unit (Millipore, Billerica, MA).

3.3.13 Conjugation of J591-PHA Synthase with SPIONS

5 nm SPIONs were synthesized and modified to with COOH-terminated PEG groups as previously described [247, 248]. EDC (1-ethyl-3-(3-dimethylaminopropyl) carbodiimide hydrochloride)/NHS (N-hydroxysulfosuccinimide) (Pierce Biotechnology, Rockford, IL USA) chemistry, following the manufactures protocol, was used to functionalize the 5 nm SPIONs with the J591 ScFv-PHA Synthase. Briefly, COOH groups on SPIONs (1 mg) were activated in activation buffer (0.1 M MES, 0.5 M NaCl, pH 6.0). Then 0.4 mg EDC and 1.1 mg of sulfo-NHS will be added to 1 mL of the activated particles and allowed to react for 15 min. Next, 1.4 μL of 2-mercaptoethanol was added to quench the EDC, followed by addition of 0.2 mg of the J591 ScFv-PHA synthase fusion protein. The reaction was then incubated for 2 h at room temperature. The reaction was quenched by

the addition of hydroxylamine to a final concentration of 10 mM. The conjugated particles were buffer exchanged and concentrated via centrifugation with a 30 kDa filter in 10 mM PBS pH 7.4. Following conjugation excess enzyme was removed via size exclusion chromatography. The conjugated particles were then reacted with the 3HBCoA substrate, to catalyze PHB polymer production, 20 μL of conjugated particles were reacted with 5 μL of 50 mM 3HBCoA substrate and 50 μg mL^{-1} Triton X-100 (Sigma Aldrich). Transmission Electron Microscopy (TEM) imaging was used to verify conjugation and polymer formation. TEM characterization was performed on a F20 FEI Technai 200 kV field transmission electron microscope (FEI, Hillsboro, Oregon). Images were recorded using a Gatan Orius 1000 dual-scan CCD camera at 1-3 s exposure times using Digital Micrograph (DM) software (Gatan, Inc., Pleasanton, CA).

3.4 Results and Discussion

3.4.1 Cloning Construct 1: J591 ScFv and Pha Synthase genes into pPic9K plasmid

The DNA sequence for the J591 ScFv-PHA Synthase fusion protein was constructed using overlap extension (OE) PCR [249, 250]. The overlap extension PCR reactions were carried out in three steps as outlined in Figure 3.1. Forward and reverse primers were designed to amplify the J591 ScFv (765bp) and PHA synthase (1770bp) genes. The J591 ScFv reverse primer added the first 16 bp of the PhaC gene to the end of J591 ScFv construct. The J591 ScFv reverse primer contained the beginning of the PhaC gene and the forward J591 ScFv and reverse PhaC primers were used to amplify the hybrid gene. In Figure 3.3A, lanes 2-5 shows amplification of the J591 ScFv template containing the 16 bp PhaC overlap and lanes 6-9 show amplification of the 1770 bp PhaC template. Figure 3.3B shows product of OE PCR amplification with the gene fusion appearing

close to 3.0 kilobases as expected. The J591 forward and PhaC reverse primers added flanking (*Xho1* and *EcoR1*) restriction sites to the 5' and 3' of the hybrid gene construct for insertion into the pPIC9K plasmid. The 3.0 kb band was gel extracted for further cloning into the pPIC9K plasmid as shown in Figure 3.4. This version of the fusion protein was 2553 bp (851 amino acids), with a molecular weight of 90 kDa. The construct was designed to include a 6x His-tag for Immobilized Metal Affinity Chromatography.

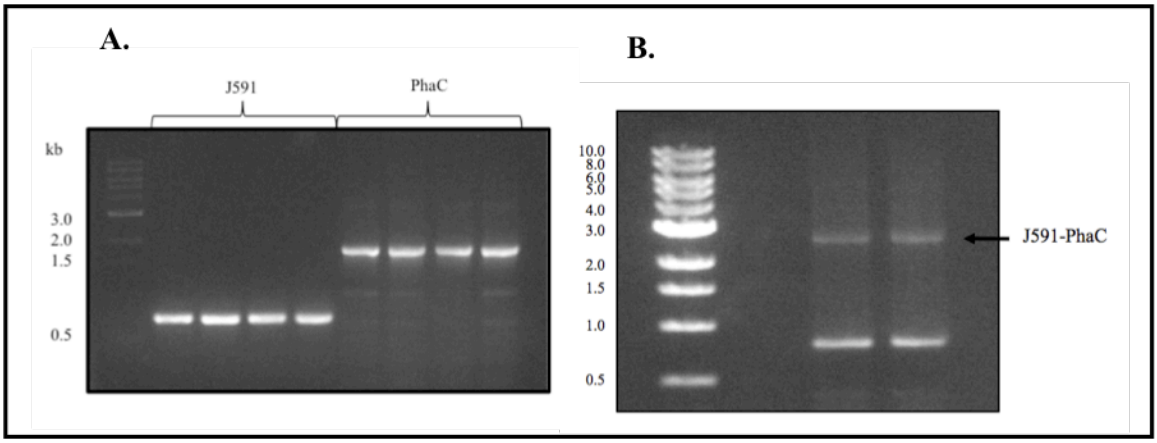

Figure 3.3 Agarose DNA Gels of J591Scfv-PhaC fusion protein overlap extension PCR reactions.

A. PCR amplification of the J591 ScFv (765bp) and PhaC (1770bp) sequences. B. Overlap extension PCR reaction to fuse the J591 ScFv and PhaC sequences.

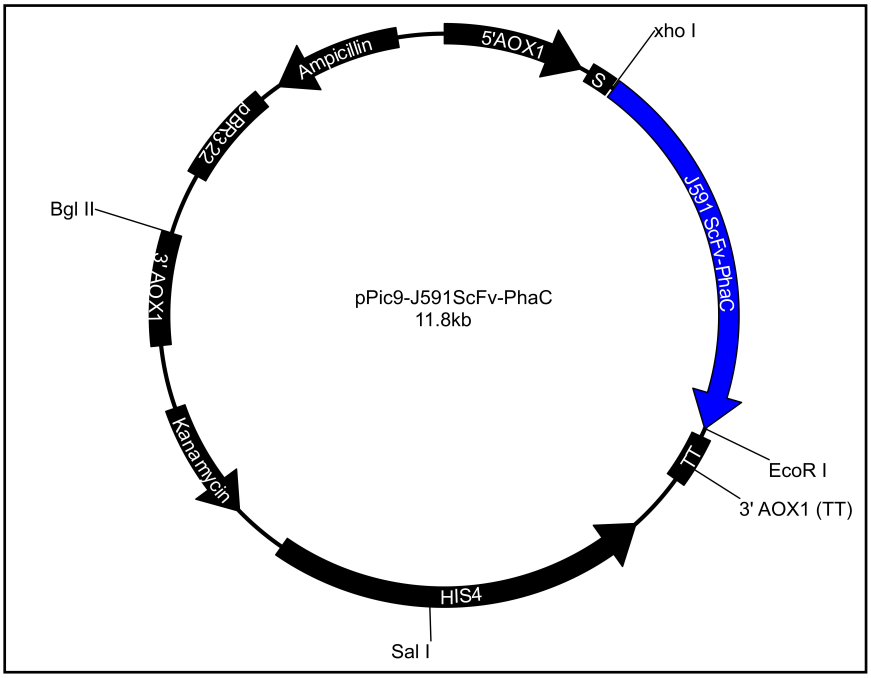

Figure 3.4 pPIC9K-J591ScFv-PhaC Construct
Plasmid map of pPIC9K-J591 ScFv-PHA Synthase expression vector. The gene was cloned between the XhoI and EcoRI restriction sites of the vector.

3.4.2 Expression of Construct 1

Construct 1 was cloned into GS115 and KM17 *P. pastoris* and transformants were screened for expression of the J591 ScFv-PHA Synthase fusion protein using SDS-PAGE and Bradford assay. A GS115 $His^{+}Mut^{+}$ was determined to have the highest level of protein production of the colonies screened and selected for further scaled-up expression of the fusion protein. A 2 L methanol-induced fermentation was used for scaled-up expression following our previously published protocol [220]. The wet cell weight and protein concentration were taken every 24 h during the induction phase of the fermentation and are plotted in Figure 3.5. As seen in Figure 3.5A, the final wet cell weight was 164 g L^{-1} and the total secreted protein concentration in the fermentation medium was 0.107 g L^{-1} after the 72 h induction. SDS-PAGE analysis confirmed expression of the 90 kDa fusion protein, and as seen on the gel in Figure 3.5B (lane 2) the

fusion protein was successfully expressed after 24 h. The 90 kDa is the most prominent band indicating that the fusion protein and made up the majority of the secreted protein in the supernatant, as is expected with *P. pastoris* secreted expression, Figure 3.5B. Mass Spectroscopy analysis on the tryptic digest of the fermentation supernatant confirmed the presence of the J591 ScFv-PHA Synthase, Figure 3.5C.

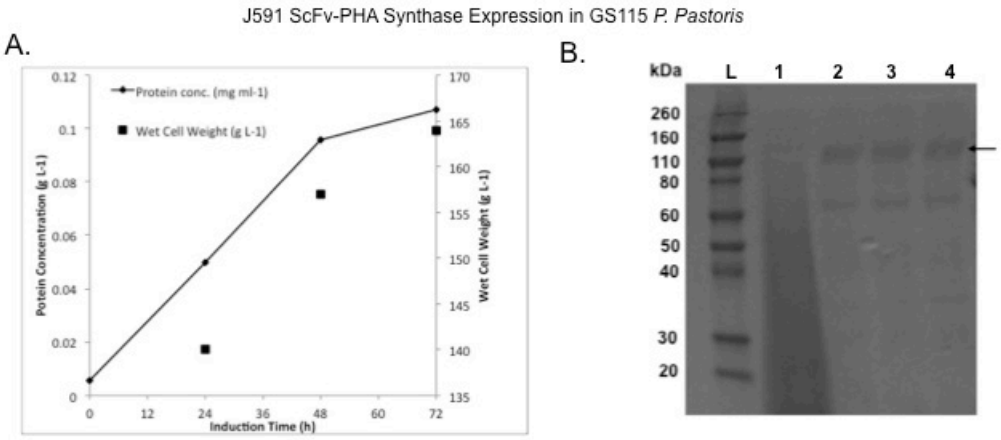

C.

Mass Spectrometry Analysis of J591ScFv – PHA Synthase Expressed in GS115	
Peptides Identified	Position
GKISQTDESAFEVGR	432
IAPAQLGDIQQR	302
ASQDVGTAVDWYQQKPGPSPK	25
LLIESGGESLR	409
STDTAYmELSSLR	199
ALTELADAVEADAK	365
NPDASmAGSTWDDYIEHAAIR	518
LLIYWASTR	45
TSGYTFTEYTIHWVK	148
YYILDLQPESSLVR	489
FAAAFYLLNAR	354

Figure 3.5 Construct 1 J591 ScFv-PHA Synthase Expression in GS115 in P. Pastoris 2 L Fermentation

(A) Protein concentration and wet cell weight during the induction stage of the fermentation of J591 ScFv-PHA Synthase Protein expressed in P. pastoris. (B) Coomassie stained SDS-PAGE gel of fermentation samples taken every 24 h during methanol induction (Lanes 1-4): 0 h, 24 h, 48 h, 72 h. The 90 kDa, J591 ScFv-PHA Synthase, protein is indicated by a black arrow. (C) Mass Spectrometry Analysis of fermentation supernatant identified the 11 peptides listed in the table from the J591 ScFv – PHA Synthase protein, confirming expression of the fusion protein.

This version of the construct did not include a linker between the single chain and PHA Synthase enzyme, which could lead to the enzyme inhibiting binding of the ScFv [251]. This construct was not codon optimized for expression in *P. pastoris,* which can be used to increase protein expression [252]. Thus construct 2 was designed to include a linker between the protein domains and the PHA synthase protein was codon optimized for expression in *P. pastoris*.

3.4.3 Cloning Construct 2: J591 ScFv linker Pha Synthase genes into pPicZαA

A 16 amino acid $(G_4S)_3$ flexible linker was added between the J591 ScFv and PhaC genes to prevent the PHA Synthase from inhibiting PSMA recognition function of the J591 ScFv [251, 253], Figure 3.6. (G_4S)n linkers are considered universal due to their flexibility and resistance to proteases [254-258]. This linker design has been successfully used for the development of fusion proteins for clinical use; including FDA approved bispecific monoclonal antibodies for targeted cancer therapeutics [259, 260]. The linker and phaC nucleotide sequences were codon optimized using the Integrated DNA Technologies (IDT, Coralville, Iowa) Codon Optimization design tool. The codon optimization was analyzed using the Genescript Rare Codon Analysis tool Codon Adaptation Index (CAI) was calculated to be 0.73 where a CAI of 1.0 is considered ideal while a CAI of > 0.8 is rated as good for expression in the desired expression organism. A double stranded genomic block fragment containing the codon optimized linker and PhaC gene was synthesized by Integrated DNA Technologies (IDT, Coralville, Iowa), Figure 3.7.

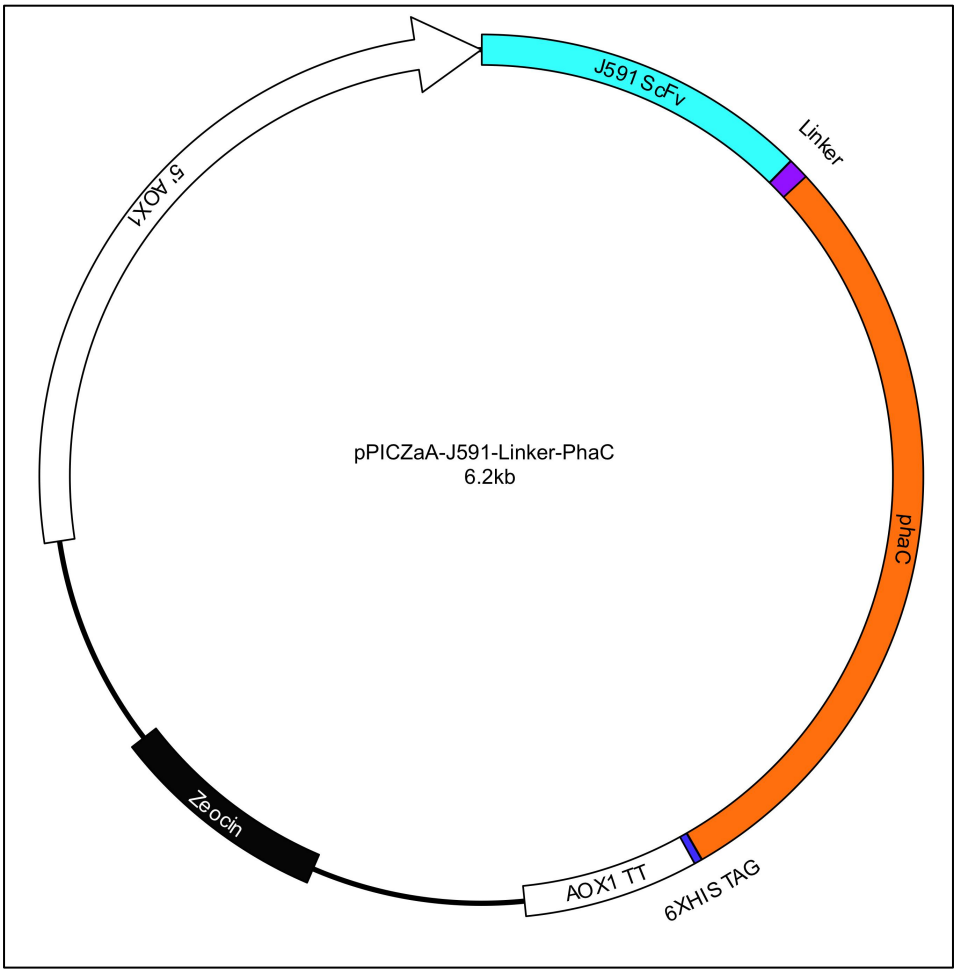

Figure 3.6 pPICZαA-J591ScFv-Linker-PhaC Construct 2.
Plasmid map of pPICZαA-J591 ScFv-PHA Synthase expression vector. The gene was cloned between the XhoI and SalI restriction sites of the vector.

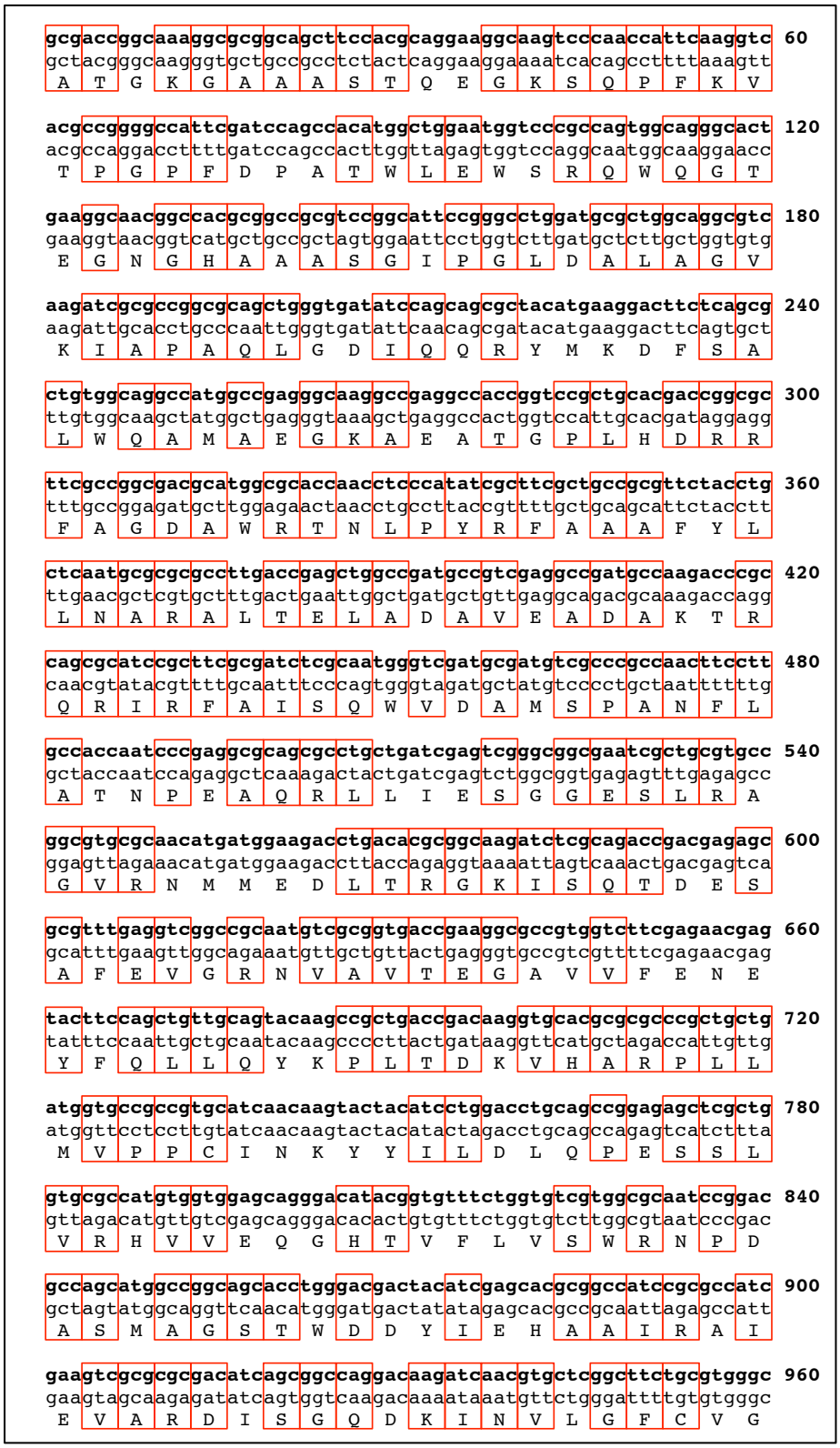

Figure 3.7 PHA Synthase Codon Optimization.

Top: Bolded text is the original PhaC gene sequence, Bottom: codon optimized sequence. The codons that differ between the two are boxed in red. (Continued on Next Page).

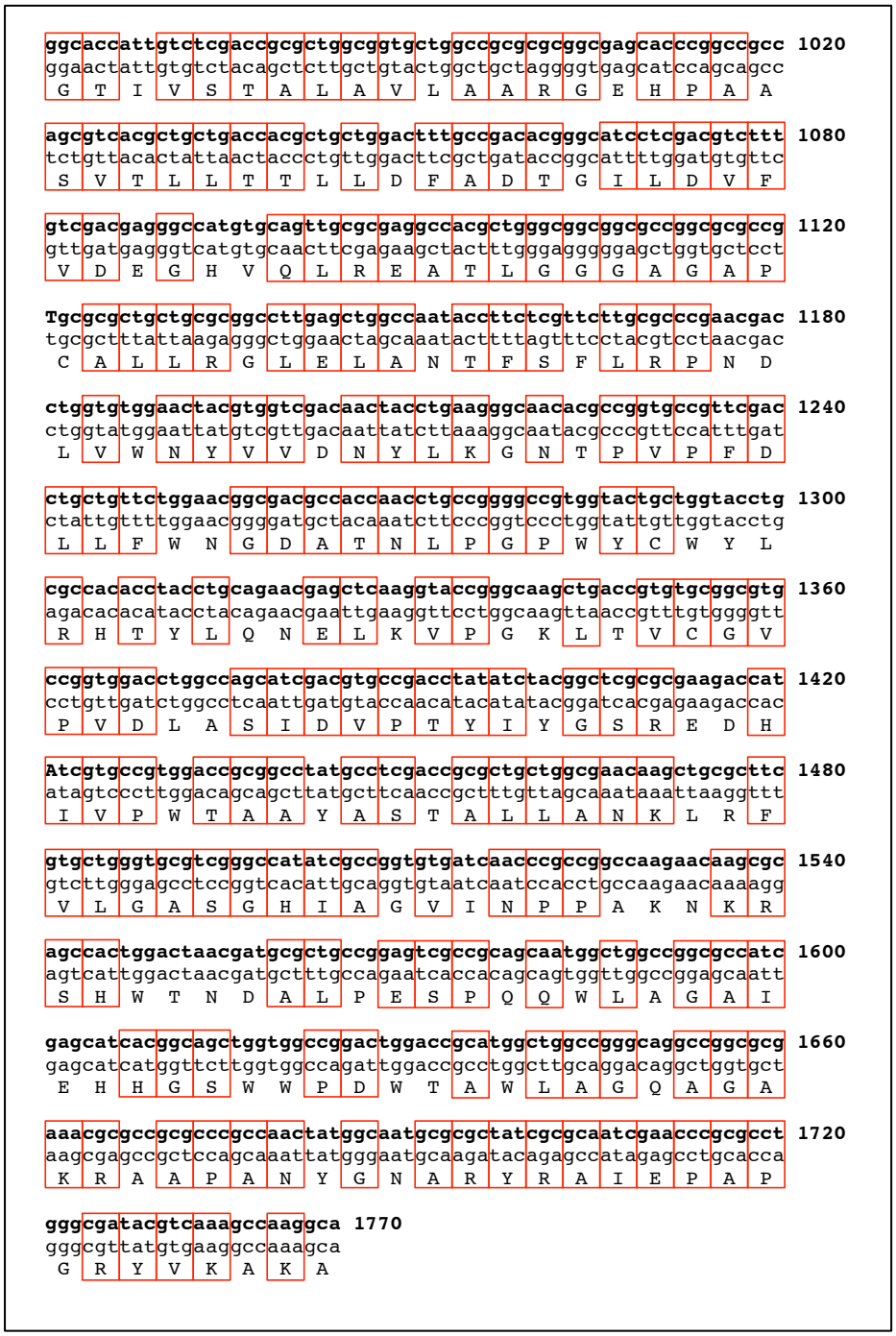

Figure 3.7 (continued) PhaC codon optimization.

3.4.4 Expression Construct 2

Construct 2 was cloned into BG11His^{+}Mut^{S} and Superman5 His^{+}Mut^{+} *P. pastoris* transformants were screened for expression of the J591 ScFv-PHA Synthase fusion as previously described. A BG11 and Superman5 transformant with the highest secretion level of the fusion protein as determined via SDS-PAGE analysis and Bradford protein assay was selected for further scaled-up expression of the fusion protein. The fusion protein was expressed in BG11 His^{+}Mut^{S} and Superman5 His^{+}Mut^{+} transformants in 2 L scale methanol-induced fermentations. Wet cell weight and total protein in supernatant measurements were taken approximately every 12 h, Figure 3.8A and B. The wet cell weight after 96 h of induction in BG11 was 199 g L^{-1} and the total protein concentration in the supernatant was 0.577 g L^{-1}. The Superman5 fermentation was stopped after 43 h of induction wet cell weight 507 g L^{-1} and a total protein concentration of 0.3155 g L^{-1}. For comparison the BG11 strain total protein concentration at a similar time point, 48 h after induction, was 0.399 g L^{-1}, which is slightly higher than the Superman5 secretion levels. SDS-PAGE analysis was run on the collected induction samples to confirm expression of the 92 kDa fusion protein, and as seen on the gel the fusion protein was successfully expressed in both BG11 and Superman5 fermentations, Figure 3.8B and D. Both the BG11 and Superman5 strains of *P. pastoris* secreted the J591 ScFv-PHA Synthase with the BG11 Mut^{S} strain producing 84 mg L^{-1} more protein at a lower wet cell weight, 268 g L^{-1} compared with 507 g L^{-1}, than the Superman5 Mut^{+} strain.

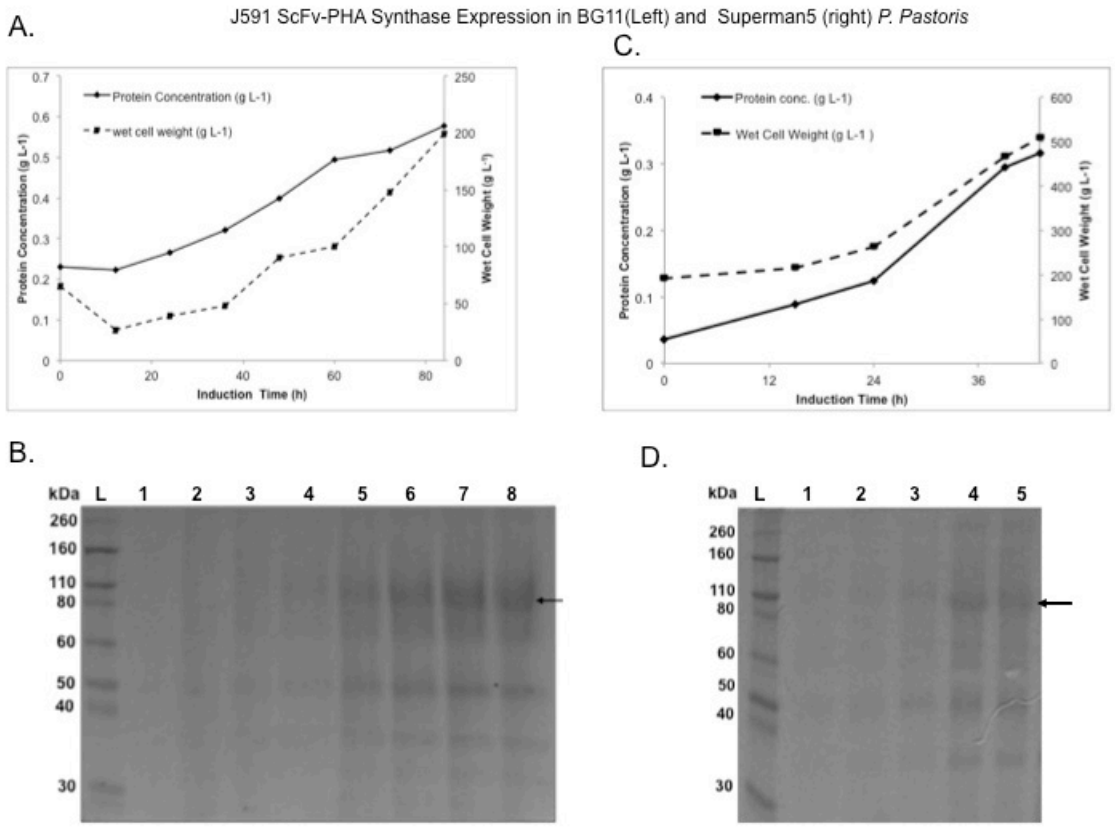

Figure 3.8 BG11 and Superman5 Construct 2 J591 ScFv-Linker-PHA Synthase expression

A. Wet cell weight and Protein concentration every 12 h taken during induction in (A) BG11 and (C) Superman5 fermenations. SDS-PAGE gel analysis of induction samples taken every 12 h for (B) BG11 and (D) Superman5 fermentations. (B) J591 ScFv-PHA Synthase expression in BG11 SDS-PAGE Gel analysis of fermentation samples Lanes: L) protein standard, induction times: 1) 0 h, 2) 12 h, 3) 24 h, 4) 36 h, 5) 48 h, 6) 60 h, 7) 72 h, and 8) 96 h. (D) J591 ScFv-PHA Synthase expression in Superman5 SDS-PAGE Gel analysis of fermentation samples Lane: L) protein standard, 1) 0 h, 2) 15 h, 3) 24 h, 4) 39 h, and 5) 43 h.

Expression of construct 2 produced a higher level of secreted expression than the previous construct 1, 0.516 g L^{-1} in BG11 Mut^S compared with 0.107 g L^{-1} in GS115 Mut^+ 72 h after induction. The BG11 fermentation had a lower wet cell weight 148 g L^{-1} than the GS115 164 g L^{-1}, which confirms that the increase in protein production is could be attributed to the codon optimization, strain phenotype, or gene integration during transformation.

3.4.5 J591 ScFv-PHA Synthase Anion Exchange Purification

J591 ScFv-PHA Synthase was purified via anion exchange chromatography. The isoelectric point of the J591 ScFv-PHA Synthase protein was estimated to be pH 6.1 using the ProtParam software (ExPASy Bioformatics Resource Portal). Clarified fermentation supernatant was buffer exchanged 20 mM sodium phosphate buffer at pH 8.0 and loaded onto a QXL Sepharose column. The protein was eluted using a linear gradient over 10 column volumes or 50 mL ranging from 0 to 1 M NaCl in 20 mM PBS at pH 8.0. SDS Gel Page analysis was used to determine the elution fraction containing the J591 ScFv-PHA Synthase protein. The 92 kDa J591 ScFv-PHA Synthase band confirmed elution of the J591 ScFv-PHA Synthase during the first 3 column volumes of the elution, with the purist fraction, determined by SDS page analysis, at 200 mM NaCl, as seen in Figure 3.9.

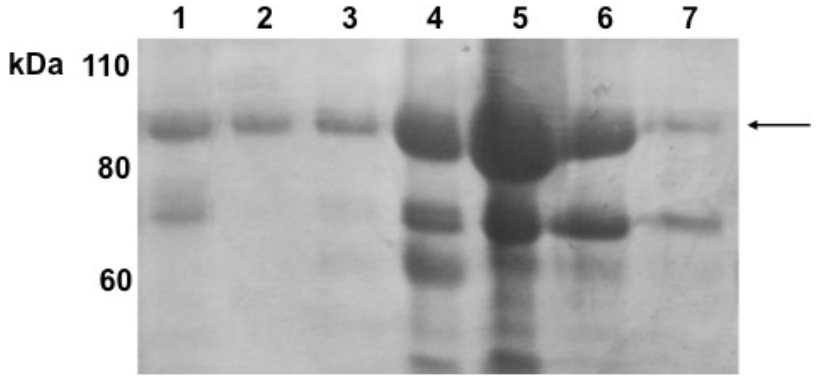

Figure 3.9 SDS-PAGE Analysis of J591 ScFv-PHA Synthase Anion Exchange purification

Elution Fractions from linear gradient of NaCl from 0 to 1 M taken from each 5 mL column volume collected for 10 column volumes, seven column volumes contained eluted proteins and are shown in the figure above. SDS-PAGE Gel analysis of elution Fractions Lanes: 1) 0-0.1M, 2) 0.1-0.2M, 3) 0.2-0.3M, 4) 0.3-0.4M, 5) 0.4-0.5M 6), 0.6-0,7 M and 7) 0.7-0.8M NaCl. The 92 kDa J591 ScFv- PHA Synthase protein, size indicated by black arrow, was eluted in the first three column volumes, with the purist fractions being column volumes 2 and 3 corresponding to lanes 2 and 3 in the figure eluted with 0.1-0.3 M NaCl.

3.4.6 Characterization of PSMA specificity

Flow cytometry was used to determine the specificity of the J591 ScFv-PHA Synthase fusion protein for PSMA. The protein was fluorescently labeled and then incubated with either LNCaP (PSMA+) or HT29 (PSMA-) cell lines for comparison. The fusion protein generated from construct 1 did not demonstrate binding specificity for PSMA. When the protein was fluorescently labeled and incubated (PSMA+) and (PSMA-) cell lines there was no significant shift in fluorescence.

The J591 ScFv –PHA Synthase fusion protein generated from construct 2 was also analyzed by flow cytometry. The protein in the fermentation supernatant was, fluorescently labeled with Alexa Fuor 488 and LNCaP (PSMA +) and HT29 (PSMA -) cell lines. Figure 3.10 contains histogram data of the fluorescence intensity of the LNCaP and HT29 cells incubated with 0, 20, and 50 μg of the labeled fusion protein. The population of positively stained cells after incubation with 20 and 50 μg proteins concentration was 96.9% and 98% for the LNCaP cells and 22.5% and 23.7% for the HT29 cells line. The results correspond to a greater than 3-fold magnitude increase in staining PSMA + cells line over the non-PSMA expressing cells, indicating that the fusion protein binds to PSMA.

In addition, the trend of the data shown in graphical form in Figure 3.10B demonstrates a dose dependent binding, as the concentration of the fusion protein increased the number of positively stained cells increased, as shown by an increase in fluorescence intensity corresponding to a shift to the right of the absorbance peak.

Since, specificity was demonstrated by the protein generated form construct 2 and not construct 1, this may indicate that the PHA synthase enzyme may be inhibiting the

activity of the J591 ScFv in construct 1. Therefore, the addition of the flexible linker must be necessary to preserve activity of the J591 ScFv region of the fusion construct.

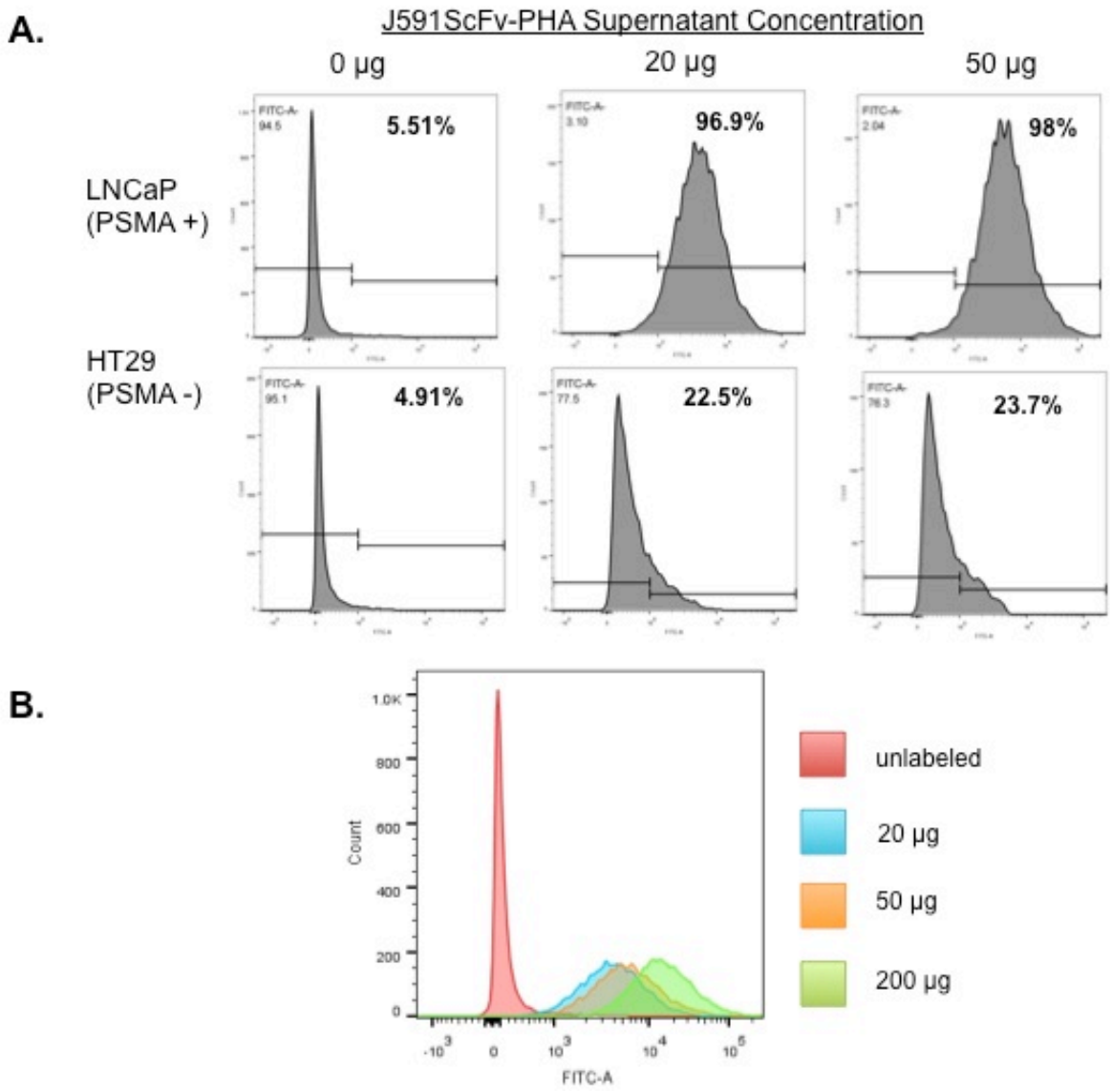

Figure 3.10 J591-PHA Flow Cytometry

Histogram plots of the fluorescence intensity measured via flow cytometry analysis (A.) of LNCaP (PSMA +) and HT29 (PSMA) cells stained with the Alexa fluor 488 labeled J591 ScFv-PHA Synthase fusion protein. The J591 ScFv domain of the fusion protein is designed to recognize an extracellular epitope of the PSMA antigen. (B.) Histogram plot of LNCaP (PSMA +) stained with increasing concentrations 0, 20, 50, and 200 µg of the J591 ScFv-PHA Synthase Alexa fluor 488 labeled protein.

3.4.7 PHA Synthase Activity Characterization

To confirm polymer synthesis activity of the J591ScFv-PHA synthase fusion protein, a sample was taken directly from the fermentation supernatant and was reacted with the 3HBCoA substrate and incubated overnight at room temperature. J591 ScFv-PHA Synthase fusion protein was incubated 5 mM 3HBCoA. Following the reaction, the polymer granules were imaged using Nile red staining under a fluorescence microscope Figure 3.11. As a control the fusion protein was incubated with out the substrate. As seen in Figure 3.11, the polymer granules formed overnight in the reaction with 3HBCoA substrate and not in the control sample.

For particle size measurement studies J591 ScFv-PHA Synthase 1 mL of protein in supernatant 0.1 mg mL^{-1} was reacted with 5 mM 3HBCoA in 2% Tween20 for 2 h at 30°C. The particles were sonicated for 20 min to break up aggregates and direct light scattering (DLS) was used to measure the size of the resulting PHB granules. The reaction produced particles with an average size of 362 nm, as seen in the histogram plotted from the particle measurements, Figure 3.11B. The particle size is a function of the protein concentration, surfactants in the reaction, and the substrate concentration [261]. The size data include a species of micron-sized particles, however these are likely aggregates, which accumulate due to the hydrophobicity of the PHB polymer.

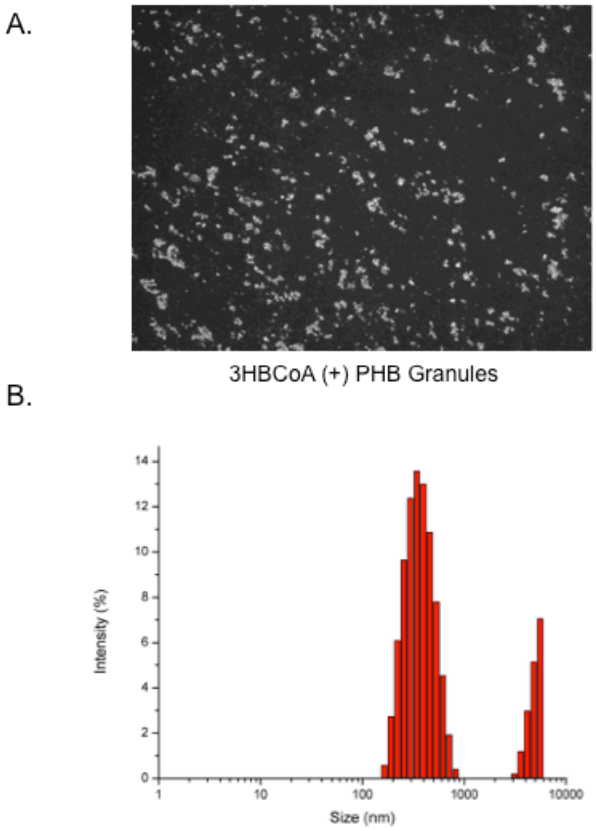

Figure 3.11 J591-PHA fusion protein synthesis of PHB granules and Direct Light Scattered Measurements of PHB Granule size.
(A) J591-PHA incubated (Left) with 3HB-CoA monomer, at room temperature overnight, and stained with Nile red 0.5 mg mL^{-1}. (B) Histogram of J591 ScFv-PHA Synthase synthesized PHB granule size measured via dynamic light scattering. Average granule size of 362 nm.

3.4.8 Surface Plasmon Resonance Real Time Polymerization Studies

In order for the fusion protein to be used for in situ vascular occlusion the protein must synthesize polymer under flow conditions. Real-time Surface Plasmon Resonance (SPR) analysis was used to measure the J591 ScFv-PHA Synthase PHB synthesis activity under flow conditions. Figure 3.12A illustrates a schematic of the SPR experiment. The J591 ScFv-PHA Synthase protein was immobilized via the 6 X histag at the C-terminus of the protein, which bind to the nickel on the functionalized gold surface of an SPR chip. The immobilization of the protein was applied for 5 min, following which buffer was run over

the chip to remove unbound protein. Three concentrations of the supernatant containing the J591 ScFv-PHA Synthase were used for SPR experiments (5.0, 1.0, and 0.5 μM) while the substrate concentration was kept constant at 0.5 mM for each experiment. For 1 and 0.5 μM protein concentrations, the increase in resonance following removal of excess protein was approximately 140 μRIU from the normalized baseline indicating a similar amount of protein loading for the two concentrations. When the concentration was increased to 5 μM the resonance angle after immobilization increased by 300 μRIU indicating that this concentration had more bound protein (Figure 3.12B). After protein immobilization, the substrate at 0.5 mM concentration was applied at 10 μL min^{-1} for 30 min. The change in resonance following the dissociation period using the equilibration buffer resulted in between 30 and 80 μRIU above the baseline for protein concentrations used in the study indicating bound polymer on the surface of the chip.

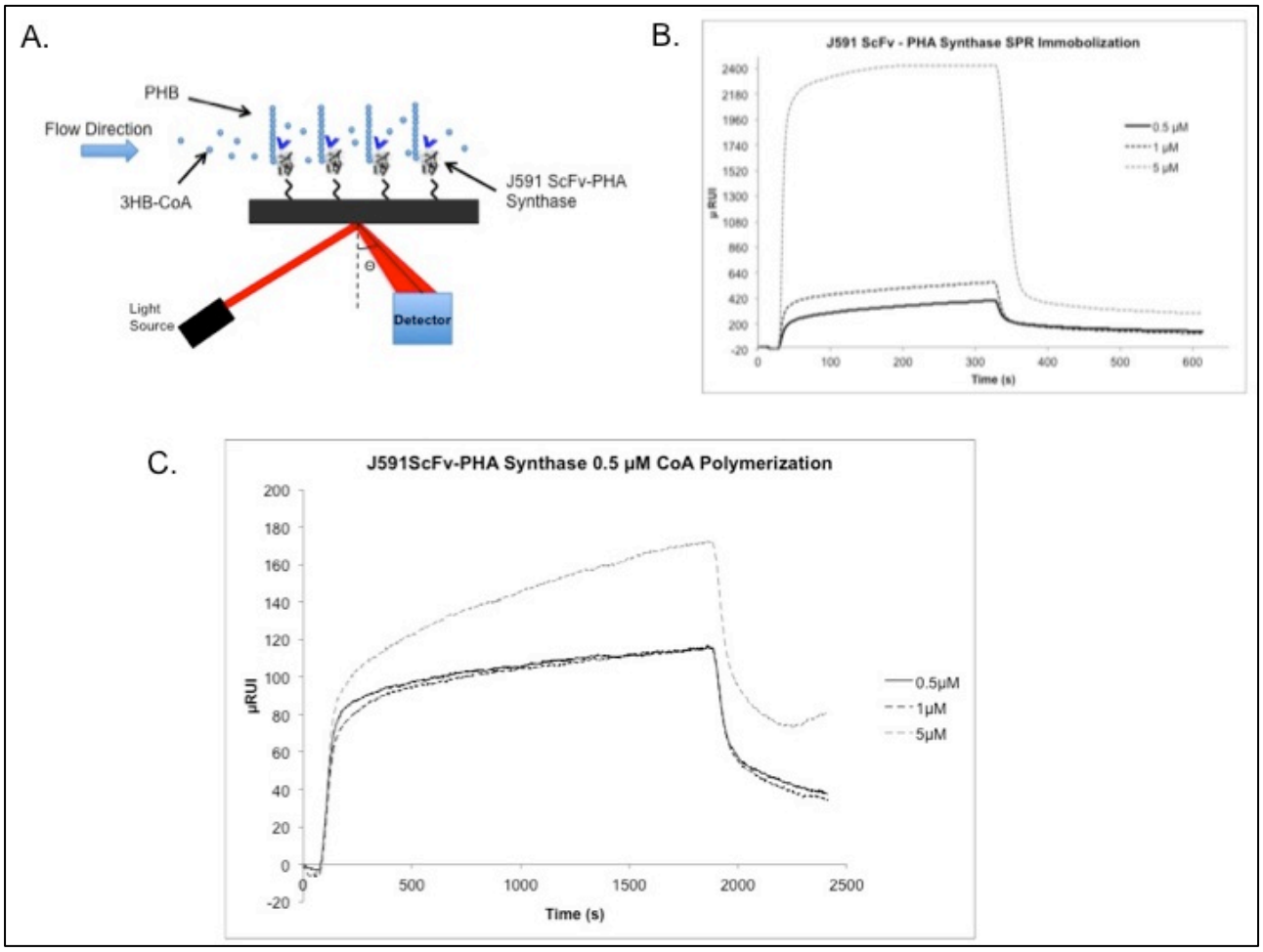

Figure 3.12 J591 ScFv - PHA Synthase PHB Synthesis Monitored in Real-Time via Surface Plasmon Resonance

(A) Schematic of the SPR experiment showing synthesis of PHB from 3HB-CoA monomer units by J591 ScFv-PHA Synthase protein immobilized on a gold SPR chip. SPR sensor gram plots (B) during immobilization of J591 ScFv-PHA Synthase in fermentation supernatant concentrations 0.5, 1, and 5 µM and (C) 3HB-CoA polymerization by J591 ScFv-PHA Synthase protein, concentration refers to the concentration of protein immobilized, the monomer concentration was kept constant for all SPR PHB synthesis experiments.

3.4.9 J591 ScFv-PHA Synthase PHB Particle Binding Confocal Studies

The J591 ScFv-PHA Synthase fusion protein was designed to form granules that recognize the extracellular PSMA epitope as the J591 mAb. The fusion protein PSMA epitope recognition was determined using confocal imaging with PHB granules synthesized via the fusion protein. The granules, with an average of diameter 362 nm,

were stained with Nile red, and were incubated with PC3-PIP (PSMA+) and PC3 (PSMA-) prostate cancer cell lines. Confocal images of cells incubated with the particles, is shown in Figure 3.13. In Figure 3.13A, a bright field image is used a reference to show relative position of particles in fluorescence images. Figure 3.13B shows an increase in fluorescence in the PC3-PIP cell line when compared to the PC3 control. When the bright field image and fluorescence image are overlapped, the PC3-PIP cells are all intensely stained with Nile Red, while the negative control PC3 cells have diffuse staining not specifically localized to the cells.

To determine if the localization of the particle fluorescence with the cells is the result of internalization of the Nile Red labeled PHB granules by means of antibody recognition of PSMA antigen, the cell lines were each blocked by the J591 Fab before incubation with the J591 ScFv-PHA Synthase PHB granules. As seen in, Figure 3.14 under the same imaging settings, there is reduced fluorescence in the PC3-PIP cell blocked with the J591 Fab compared to the staining seen in the unblocked PC3-PIP cells. In the negative control PC3 cells, there was a minimal amount of staining in the unblocked sample and the addition of the J591 Fab had no impact on the staining of the cells. Next, a Z-stack confocal images of the PC3-PIP cells incubated with the particles was used to determine particle internalization. As seen in Figure 3.15, 3D renderings and orthogonal images with bright field overlay show that the J591 ScFv-PHA Synthase PHB granules are located inside of the cells.

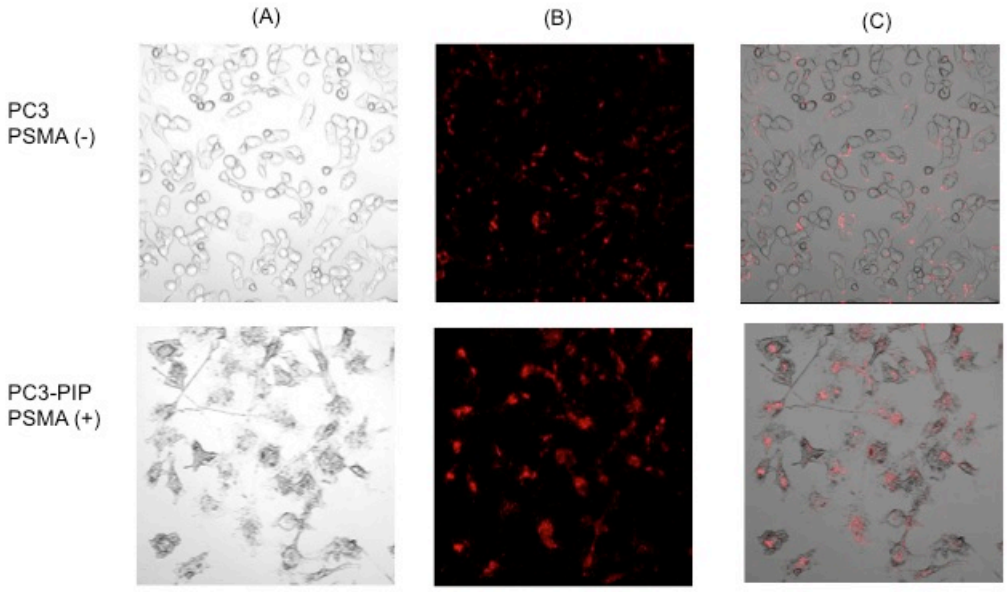

Figure 3.13 J591 ScFv-PHA Synthase granules incubated with PSMA- and PSMA + prostate cancer cell lines and imaging via confocal microscopy.
Top images PC3 (PSMA-) and Bottom images PC3-PIP (PSMA+) cells incubated with J591 ScFv-PHA Synthase PHB Granules: (A) Bright field images, (B) fluorescence images, and (C) overlaid images taken via confocal microscopy.

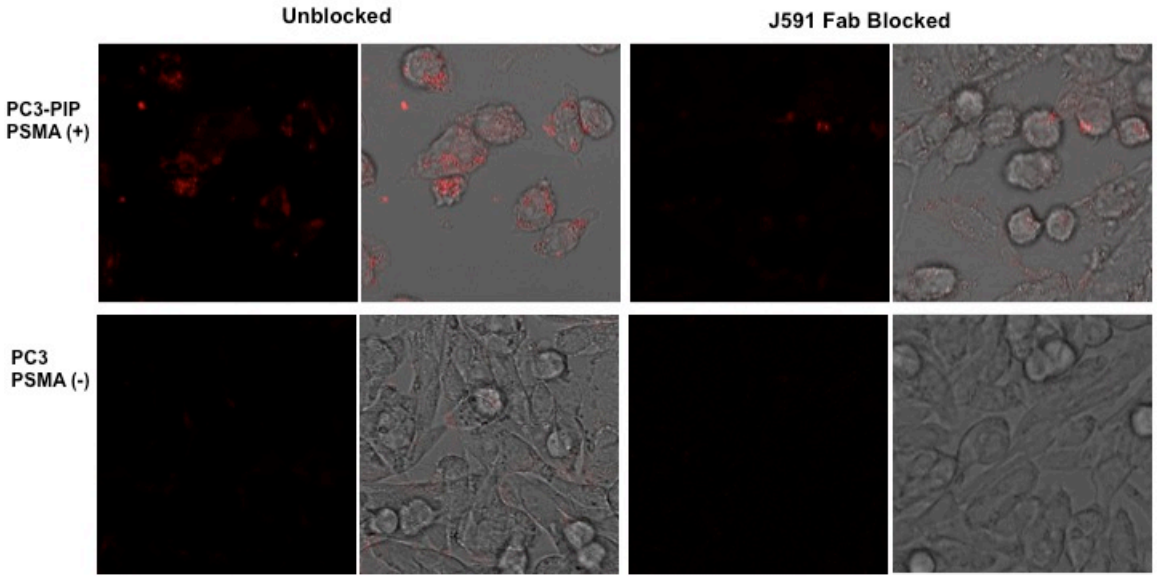

Figure 3.14 Blocking Studies

Fluorescence and combined, fluorescence and bright field overlaid, confocal images of (Top) images PC3-PIP (PSMA+) and (Bottom) PC3 (PSMA -) images cells incubated with J591 ScFv-PHA Synthase PHB Granules. Left: (Unblocked) Cells incubated with PHB granules without blocking. Right: (J591 Fab Block) Cells blocked with J591 Fab before incubating with the J591-PHA Synthase PHB granules.

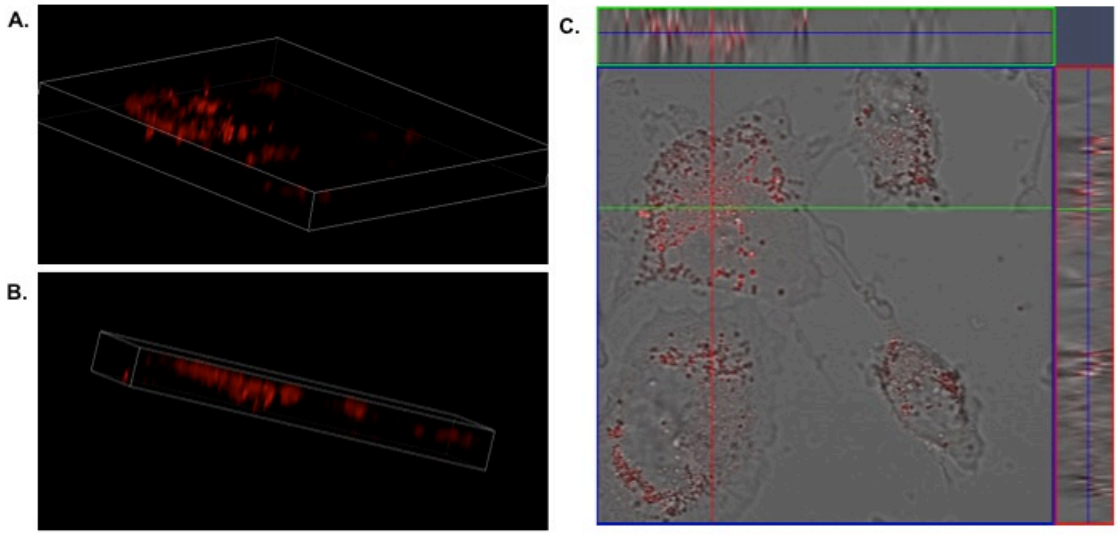

Figure 3.15 Particle Internalization Confocal Z-Stack
(A) and (B) 3D fluorescence images of z-stack images, and (C) Orthogonal projection views of z-stack image shows internalization of J591-PHA granules in PC3-PIP (PSMA+) cells. Z-stack images show cross-sectional view of the cells and the particles located inside of the cells.

3.4.10 Nanoparticle Conjugation and Activity

Nanoparticles are the purposed delivery system for in situ polymerization of the J591 ScFv-PHA Synthase fusion protein. In order for this to be a reliable delivery method the functionalization of the particles should not effect the activity for the protein. SPIONs conjugated with J591 ScFv-PHA synthase to determine if attaching the protein to the nanoparticles inhibits PHB synthesis. SPIONs were bioconjugated using EDC/NHS chemistry with the J591 ScFv-PHA Synthase protein, excess protein was removed via gel filtration, and the J591 ScFv-PHA Synthase-SPIONs were incubated with 5 mM CoA-Substrate for 2 h at room temperature for PHB synthesis. TEM images were taken of the reaction, Figure 3.16, and show SPIONs surrounding and embedded in PHB polymer granules. Therefore the conjugated nanoparticles successfully produced PHB polymer

granules *in vitro*. The particles from this reaction ranged in size from 500 nm to 2 μm in diameter, as measured during imaging.

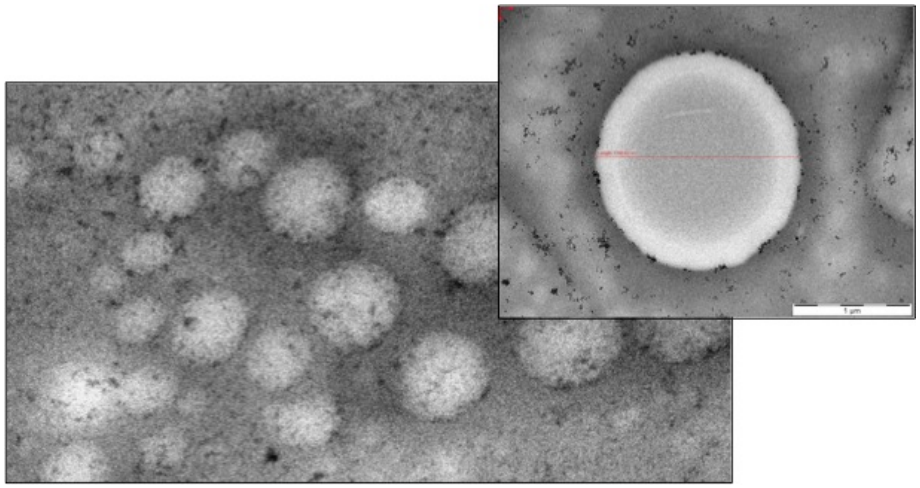

Figure 3.16 PHB granules formed from SPIONs conjugated with J591 ScFv-PHA synthase.
On the left multiple PHB granules formed by conjugated SPIONs. On right zoomed in image of a particle coated granule.

3.5 Conclusion

We have designed, constructed, and produced the J591 ScFv-PHA synthase fusion protein in *P. pastoris*. The J591 ScFv-PHA synthase fusion protein will provide the targeting moiety, J591 ScFv, and occlusion effector moiety of our system, PHB polymer synthesized by the PHA synthase enzyme. This study found the addition of a flexible linker between the two protein domains and codon optimization of the gene construct to be the optimal in regards to protein functionality and production of the fusion protein in *P. Pastoris*. Omitting the linker from the construct inhibited PSMA recognition of the J591 ScFv. Condon optimization resulted in more than 2-fold increase in yield. Flow cytometry studies were used to confirm PSMA recognition of the fusion protein, and the results showed the protein bound to PSMA expressing cells and not to PSMA non-expressing cell lines used in the experiment. The protein successfully synthesized PHB

granules *in vitro* in the form of granules 362 nm in diameter. Additionally, the protein showed polymer synthesis under flow conditions as measured via SPR analysis. The fusion protein PHB particles were internalized by PSMA expressing PC3-PIP cells, without internalization in non-PSMA expressing cells. Particles may have additional function in cancer imaging, because they are up-taken specifically by PSMA expressing cells. These particles can be labeled with fluorescent dyes or conjugated with MRI contrast agents, such as SPIONs or Hybrid Nanoparticles, for imaging enhancement.

3.6 Acknowledgements

Imaging data was acquired through the Cornell University Biotechnology Resource Center, with NIH 1S10RR025502 funding for the shared Zeiss LSM 710 Confocal Microscope.

CHAPTER 4 Conclusion and Future Directions

The object of this work was to develop a means to selectively and non-invasively cutting off the blood supply to solid tumors via targeted in situ polymer growth. This was accomplished via the creation of a dual modal protein a composed of a tumor neovasculature targeting moiety and a polymer-synthesizing moiety. A single chain variable fragment (J591 ScFv) that recognizes the extracellular glyco-protein prostate specific membrane antigen (PSMA) was fused with Polyhydroxylalkanoate (PHA) Synthase, the key enzyme for biosynthesis of polyhydroxyalkanoic acids (PHAs), from *Ralstonia eutropha* H16 and expressed in *P. pastoris*.

Future work will include *in vivo* studies in a mouse model to determine if the J591 ScFv-PHA synthase fusion protein will effectively target the tumor neovasculature and synthesize a sufficient quantity of polymer to block tumor microvessels. However, the ScFv portion of the protein will have to be substituted as there is currently is not a mouse model that expresses PSMA. An alternative to the *in vivo* mouse model is to create a microfluidic device that can mimic the tumor vasculature for feasibility studies of the in situ polymer formation approach to treat solid tumors via blocking the neovasculature. Preliminary experiments, included in the Appendix section I, with microfluidics seeded with PSMA expressing PC3-PIP cells have demonstrated that an accumulation of PHB can be observed via confocal microscopy and that the fusion protein can produce enough polymer to cause obstruction in the channels. The next step is to design a microfluidic device that more accurately models the tumor microenvironment for further *in vitro* studies. Additionally we have preformed preliminary *in vivo*, detailed in Appendix I,

experiments with synthetic PHB granules that demonstrate imaging of PHB granules *in vivo* and present protocols that can be used in further studies.

In this study we proposed the option of conjugating the fusion protein with superparamagnetic iron oxide nanoparticles (SPIONs) to allow for monitoring via Magnetic resonance imaging (MRI) and potentially provide a means increasing the valency of the fusion protein. However, due to the large size of the fusion protein, 92 kDa, it would be possible to label the protein itself or image the PHB polymer after the in situ synthesis reaction. Further studies are required to determine the most effective method of monitoring the activity of the fusion protein *in vivo*.

Overall, the work presented here presents an innovative dual modal approach to cancer therapeutics that is non-invasive with limited harmful side effects. This method could be used to augment current therapeutics and if effective could potentially be an improvement current methods of cancer treatment. Additionally targeted in situ growth of biodegradable PHB polymer could be used to develop other medical advances that require non-invasive temporary biodegradable polymer, for applications such as: surface modification of an immunogenic implant or in situ formation of a tissue scaffold.

APPENDIX

APPENDIX I. Preliminary *In vitro* Microfluidic Studies and *In vivo* Studies

i.i. In Vitro Microfluidic Studies

Microfluidic Device Fabrication

A simple microfluidic device was designed fro preliminary proof of concept experiments with multiple vascular-sized channels [262] connected in parallel to a single inlet channel. The use of transparent PDMS allows for visual characterization of polymer formation in the channel via confocal microscopy. A 3D rendering of the microfluidic device, with channel sizes 1mm in width, 0.5mm in height, and 500 mm in length, was created using SOLIDWORKS (Dassault Systèmes SOLIDWORKS Corp., Waltham, Massachusetts, USA) Computer-aided drafting software, Figure i.i. A 3D printer (ObJetPro by Stratasys, Eden Prairie, MN), used to generate mold composed of transparent plastic (VeroClear RGD 810, Stratasys). The mold was coated in parylene via vacuum deposition (PDS 2010 LABCOTER, SCS Equipment, Indianapolis, IN). To fabricate the device the mold pattern transferred to Polydimethylsiloxane (PDMS) and the PDMS mold was bonded to a glass slide, following standard protocols. The micro device was fabricated using rapid prototyping [263].

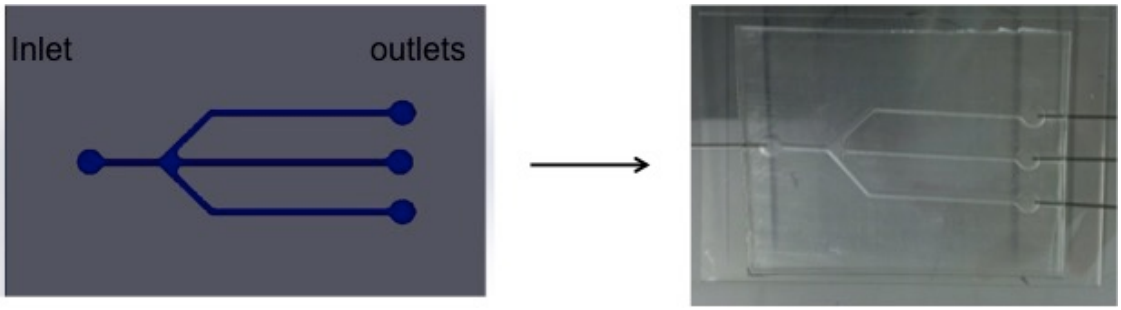

Figure i.i Microfluidic Device Design.
(left) SOLIDWORKS CAD drawing of the microfluidic device containing a single inlet connected to 3 outlet channels (1mm in width, 0.5mm in height, and 500 mm in length). (right) Image of actual device created via rapid prototyping with PDMS on a glass slide.

Microfluidic Cell Seeding and Imaging

Before seeding, the channels were coated with fibronectin to allow cells to attach on the channel surfaces. The microfluidic device was flushed with 70% ethanol to sterilize and then flushed with sterile PBS, before applying fibronectin from human plasma (Sigma-Aldrich) into the channels, and incubating with fibronectin, to coat the glass, overnight at 37^{o}C and 5% CO_2 in a humidified incubator. Following incubation the channels were flushed with PBS and cells were seeded according to previously published protocols [264].

The PC3-PIP prostate cancer cell line was cultured in Minimum Essential Media (Life Technologies, Carlsbad, CA USA) supplemented with: 1% penicillin–streptomycin respectively at 37^{o}C and 5% CO_2 in a humidified incubator and grown to 80% confluence in 200 mm flasks. PC3-PIP cells were then removed from the flasks with trypsin (Life Technologies, Carlsbad, CA USA), and suspended in cells Minimal essential Media supplemented with 8% dextran the cells were then applied to the channel at a flow rate of 2 μL min^{-1} for 48 h. The channels were then supplemented with fresh media for 3 to 5 days at a rate of 20 uL min^{-1}. The inlet flow conditions will be controlled using a syringe pump (Harvard Apparatus Pump 33).

To occlude the channels 1 mg of the J591 ScFv –PHA Synthase fusion protein was reacted with 5 mM 3HB-CoA substrate for 2 h to form granules in PBS. The particles were spun down and resuspended in MEM media. The particles were incubated with Nile red solution (0.05% v/v), and applied to the channels at a flow rate of 20 uL min^{-1}. The PHB granules accumulated in the channels until the back pressure prevented further flow through the channels. Confocal microscopy using a Zeiss LSM 710 confocal microscope (Zeiss, Germany) was then used to visualize accumulated PHB granules in the channels. The confocal images of the channels with accumulated PHB are shown in Figure i.ii. As seen in the figure the PHB granules are easily visualized in the fluorescent images and the majority accumulated at the channel side-walls. However, because the cells in the channel are not labeled it is difficult to determine if the particles are associated with cells. Improvements to *in vitro* microfluidic include: creating a 3D channel to more accurately model the *in vivo* tumor neovasculature environment and label the cells fluorescently to determine if the PHB is specifically binding to the cells or are only interacting with the channels themselves.

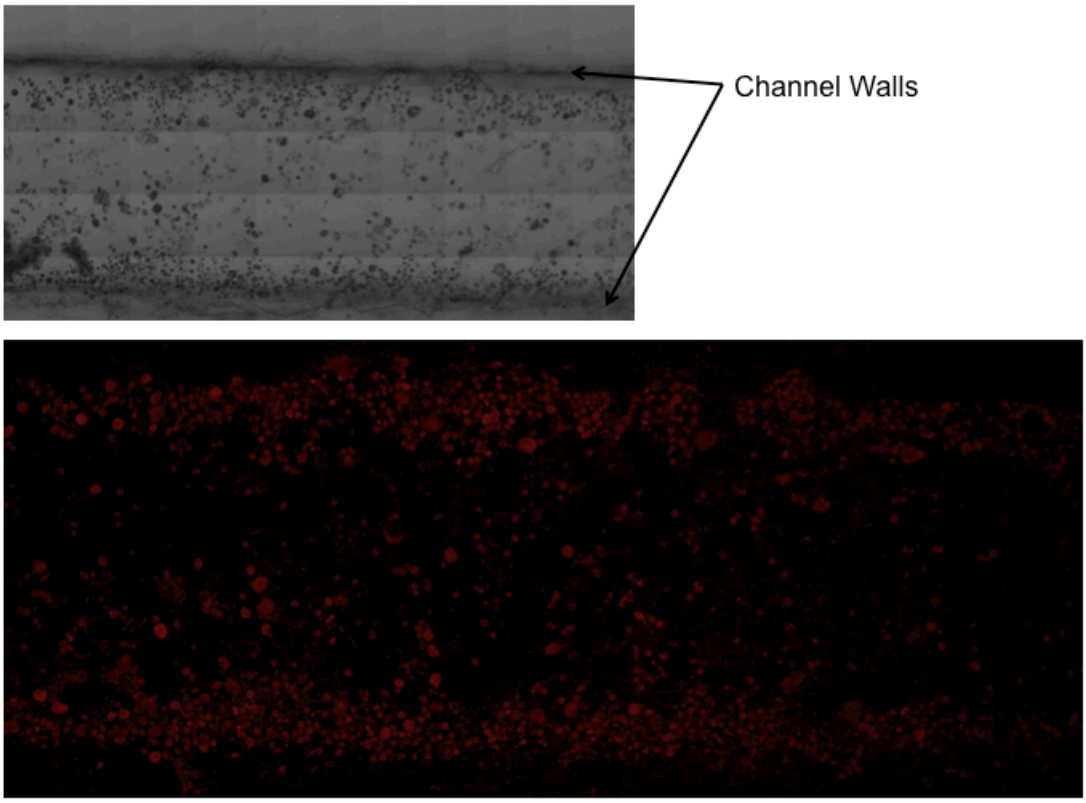

Figure i.ii Confocal images of PHB granules in cell seeded microfluidic channel
(Top) Bright field image of J591 ScFv targeted PHB granules in a microfluidic channel seeded with PC3-PIP cells. (Bottom) Fluorescent image of the same channel with PHB granules labeled with Nile Red. As seen in the image the majority of the PHB granules accumulated at the channel side-walls.

i.ii. *In Vivo* Studies Visualization of PHB Granules in Tumor Vasculature

PHB Granule Synthesis

These methods were adapted from the water-in-oil-in-water emulsion solvent evaporation technique as previously described [1-3]. A solution of 2% Poly(vinyl alcohol) PVA was prepared by dissolving 20g of PVA in 1000 ml of deionized (DI) water. The PVA was allowed to fully dissolve on a stir plate overnight. 180 mg of Poly[(R)-3-hydroxybutyric Acid] (PHB) (Sigma-Aldrich) was dissolved in 6 mL of dichloromethane (DCM) and then added to 24ml 2% PVA solution with intermediate vortexing. The solution was placed on ice for 5 min and sonicate at 45W for 120 min then the NP emulsion was

stirred for 12 hours on a stir plate in a fume hood to allow evaporation of DCM and NP stabilization. To isolate the nanometer sized population and remove residual the solution was centrifuged for 25 minutes at 20,000 rpm at 4°C twice to PVA. The pellet was resuspended in 8ml of DI water and centrifuge for 10 minutes at 1000 rpm at 4°C the supernatant was isolated and flash froozen it at -80° C. The sample was lyophilized for 48 hrs and the particles were stored in a dessicator at -80° C until time of use.

Dynamic light scattering (DLS) measurements of PHB granules were taken using a Zetasizer Nano-ZS (Malvern Instruments Ltd, Worcestershire, UK). The particle size was calculated as the average of six consecutive measurements recorded at 25 ºC.

Particle Labeling and *In vivo* Imaging

PHB particles were labeled by incubating 1 mg of particles with 15 µL of DiD dye (Vybrant, Life Technologies).

Accumulation of DiD-labeled PHB in tumor microenvironment were visualized and quantified by intravital microscopy. Tumors were exposed using a skin-flap procedure. In brief, a midline abdominal incision was performed with a wetted cotton applicator used to peel away skin and expose the tumor while avoiding vascular occlusion. Before imaging, a bolus injection of 70 kDa FITC-dextran (50 µL in PBS) was used to delineate the vasculature. Images were obtained with a two-channel setup in which the fluorescence was collected at 488/525 nm for FITC-dextran and at 624/665 nm excitation/emission filters for DiD-labeled PHB. Fluorescently labeled PHB granules were injected through the tail vein. The following figures i.iii and i.iv PHB granules visualized within the tumor vasculature taken in real-time under flow. As seen in Figure i.iii, PHB granules accumulated at vessel junctions, in the figure the particles are concentrated in specific

areas that correspond to vessel junctions; this could be due to their hydrophobicity. Based on these studies and previous *in vitro* work this shows that the particle accumulate resulting in high density of particles in small volume area, which would be necessary to occlude the blood vessels.

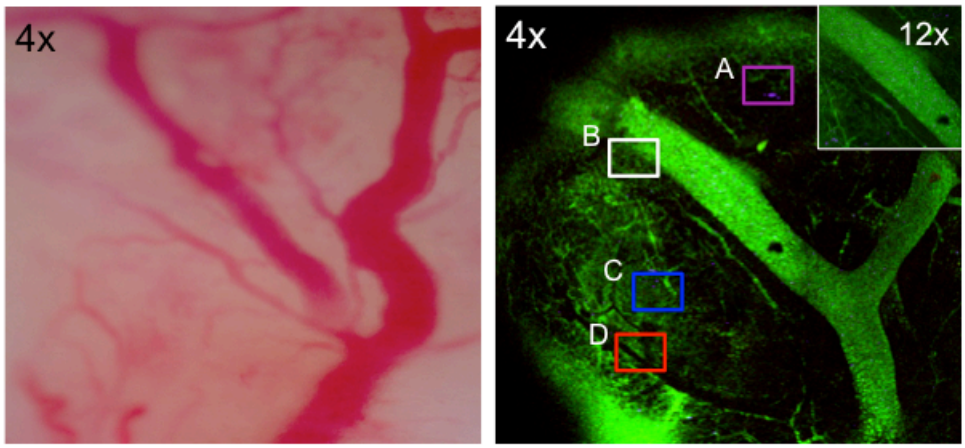

Figure i.iii In vivo imaging of PHB in tumor microvasculature
Implanted tumors were exposed using a skin-flap procedure for intravital microscopy imaging. PHB granules were injected into the vessels for imaging studies. (Left) Tumor blood vessel bright field image; (Right) merged fluorescent microscopy images of the same vessel stained with FITC (green) and PHB stained with DiD dye (violet) under 4x magnification; including an overlaid image at 12x magnification. The boxed regions are labeled A-D and were used for further imaging at a higher magnification to visualize PHB in vivo, shown in Figure i.ii.

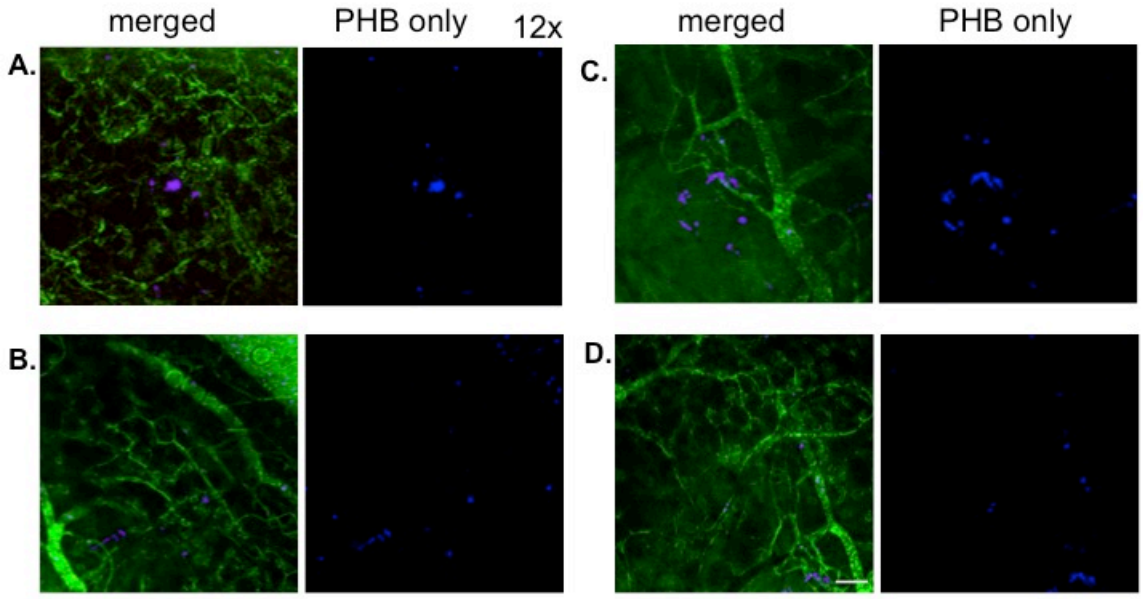

Figure i.iv Fluorescent images of PHB granules in tumor microvasculature in vivo studies

The four areas labeled A-B in the previous image (Figure i.iii) are shown here. On the left: of each image is the merged fluorescent images showing the vessels stained with FITC (green) and PHB stained with DiD dye (violet). On the right: the image of PHB alone in the vessels.

APPENDIX II. Optimization of Norovirus Virus-Like Particle Production in *Pichia Pastoris* Using a Real-Time Near-Infrared Bioprocess Monitor

Article for submitted to Biotechnology and Bioengineering. Stephanie A. Parker, Mitchell H. Maloy, Jaime Tome-Amat, Cameron L. Bardliving, Kaylee J. Lanz, Mark A. Arnold, Carl A. Batt

i.iii. Abstract

The production of norovirus virus-like particles (NoV VLPs) displaying NY-ESO-1 cancer testis antigen in BG11 *Pichia pastoris* has been optimized through the use of a real-time near-infrared bioprocess monitor (RTBio™ Bioprocess Monitor, ASL Analytical, Inc.). The production of NoV VLPs displaying NY-ESO-1 in *P. pastoris* is important for demonstrating the potential for this expression system to be used to generate VLP-based cancer vaccines for pharmaceutical applications. Optimization of the growth conditions resulted in expression levels of 0.85 g L^{-1} of VLP-NY-ESO-1 in the supernatant of *P. pastoris* grown in a 2 L bioreactor as compared to the pre optimization levels of 0.45 g L^{-1}. We investigated the effects of methanol concentration, batch phase time, and batch to induction transition on NoV VLP-NY-ESO-1 production. The real-time bioprocess monitor was used to monitor and control glycerol and methanol concentrations throughout the fermentation process. The optimized process included a glycerol transition phase during the first 2 h of induction and maintaining methanol concentration at 4 g L-1 during in induction. The sensor resulted in the maximum NoV VP1-NY-ESO-1 yield of 0.85 g L^{-1}.

Keywords
Norovirus Virus-Like Particles (NoV VLPs), NY-ESO-1, Fed-Batch Fermentation

i.iv. Introduction

Virus-like particles (VLPs) mimic the structure of native viruses, but lack the viral genome and are thus non-infectious. Recombinant expression of structural viral proteins, capsid and envelope, can result in the self-assembly of VLPs. Due to their repetitive, antigenic structure, VLPs are highly effective at inducing significant immune responses

[265, 266]. Several VLP-based vaccines have been commercialized and approved for therapeutic applications including prophylactic vaccines for hepatitis B [267] and cervical cancer [268, 269]. Chemical and genetic modifications have been used to incorporate one or more antigens into multimeric VLP protein structures [270, 271]. The potency of VLPs can generate a protective response at lower doses of antigen, substantially reducing vaccine cost [272, 273]. VLPs modified to display tumor-associated antigens have been developed to enhance the antitumor cytotoxicity response to the peptides. Murine cancer model study findings have demonstrated that vaccination with VLPs displaying tumor associated antigens leads to a delay in tumor development *in vivo* [271, 274, 275].

Widely used recombinant protein production platforms for VLP production include bacterial [276], insect, mammalian cells, and yeast. Here, *P. pastoris*, a methyotrohic yeast, was been investigated as an expression platform for norovirus VLPs (NoV VLPs) displaying a cancer testis antigen, NY-ESO-1. The *P. pastoris* expression system has been genetically engineered for the production of milligram-to-gram quantities of recombinant proteins and is commonly used for industrial, pharmaceutical, and basic research applications [277-279]. Advantages of the *P. pastoris* expression system over other widely used systems include genetic stability, highly regulated promoters, such as the methanol inducible alcohol oxidase I gene (*AOX1*) used in this study, and secretion of heterologous proteins with low levels of endogenous proteins thus reducing complexity of downstream processing [280-284]. Fed-batch high cell density fermentations of *P. pastoris* have been well characterized and several strategies have been developed to optimize recombinant protein production [285, 286].

This work builds on our previous study demonstrating the expression and secretion of the norovirus capsid viral protein 1 (VP1) in *P. pastoris* resulting in self-assembled non-infectious NoV VLPs [287]. Here, VP1 was genetically modified to display the NY-ESO-1 cancer testis antigen for recombinant expression in *P. pastoris*. NY-ESO-1 is a highly immunogenic cancer antigen expressed in multiple types of tumors, as well as in normal adult tissues with the exclusion of germ cells in testes and ovaries [288, 289]. NY-ESO-1 has been studied for use in specific-immunotherapy for patients with NY-ESO-1 positive cancers including advanced colorectal cancer (CRC) [290]. Clinical trials have demonstrated that NY-ESO-1 based vaccines are effective at inhibiting tumorogenesis and tumor growth [291, 292].

Near-infrared spectroscopy (NIRS) has been shown to provide accurate and reliable real-time measurements of the targeted analytes, glycerol and methanol, in *P. pastoris* bioprocesses [293, 294]. In this investigation, the RTBio^{TM} Bioprocess Monitor (ASL Analytical, Inc. Coralville, IA) was used for continuous, real-time monitoring and control of the glycerol and methanol concentrations during the cell growth and production phases, respectively. The output and control provided by the bioprocess monitor were critical for optimizing the conditions for VP1-NY-ESO-1 production in *P. pastoris*.

i.v. Materials and Methods

Organisms and Constructs

Our previously described pJ912-NoV-VLP plasmid construct containing two multi-cloning sites, which facilitate cloning into two external loops of the NoV VLP, was used for expression in *P. pastoris* under the control of the AOX1 promoter [287]. The gene encoding the NY-ESO-1 antigen was inserted into the second multi-cloning site of the

pJ912-NoV-VP1 plasmid, allowing for external display of the antigen on the surface of the NoV VLPs. The *P. pastoris* BG11 (HIS^+, Mut^S, Biogrammatics, Inc., Carlsbad, CA) was transformed with the pJ912-NoV-VP1-NY-ESO-1 construct for expression.

Fermentation Conditions

A single *P. pastoris* colony was used to inoculate 5 mL of YPD medium [1% yeast extract, 2% peptone, 2% dextrose] and grown overnight at 30°C. The culture was diluted to an OD_{600} of 0.01 in 100 mL BMGY [1% yeast extract, 2% peptone, 100 mM potassium phosphate (pH 6), 1.34% YNB, 1% glycerol, $4x10^{-5}$ % biotin], grown to an OD_{600} of 20, and used to inoculate the fermentation medium.

Fermentations were performed in a 2 L New Brunswick Scientific BioFlo 3000. A total of 1.5 L of basal salt media [0.375 g $CaSO_4 \cdot 7H_2O$, 7.50 g K_2SO_4, 6.15 g $MgSO_4 \cdot 2H_2O$, 1.70 g KOH, 11.02 mL H_3PO_4, 82.5 mL glycerol, 0.5 mL antifoam 204] was prepared and sterilized within the vessel. A total of 7 mL PTM trace salts [2.1 mM $CoCl_2$, 24 mM $CuSO_4$, 19.87 mM $MnSO_4$, 0.53 mM NaI, 0.83 mM Na_2MoO_4, 0.32 mM boric acid, 0.15 mM $ZnCl_2$, 0.23 M $FeSO_4$, 0.82 mM biotin] were added to the vessel after sterilization. Dissolved oxygen (DO) was measured using the Mettler Toledo lnPro 6110/220 sensor (Mettler-Toledo GmbH, Germany) and maintained at 40% through cascade control of agitation and pure oxygen supplementation. The pH was measured using a Mettler Toledo 405-DPAS-SC-K8S/225 combination pH probe and controlled at 3.0 using 15% NH_4OH. As applicable, the glycerol feed [63% (w/v) glycerol and 12 mL L^{-1} PTM Trace Salts] and methanol feed (ultra-pure methanol with 12 mL L^{-1} PTM salts) were controlled with the RTBio™ Bioprocess Monitor**.**

Feed Strategies

VP1-NY-ESO-1 production was induced by adding methanol to the fermentation medium when either the glycerol concentration or cell density reached a targeted value. Three strategies were evaluated for maximizing production of the VP1-NY-ESO-1 construct. The first strategy consisted of a glycerol batch phase at inoculation, followed by methanol induction after glycerol depletion, as indicated by the output of the bioprocess monitor and confirmed with a spike in the DO sensor of approximately 55%. In the second strategy, the initial glycerol batch phase was followed by a glycerol fed-batch phase, where the concentration of glycerol was maintained at 10 g L^{-1} until the wet cell weight (WCW) was greater than 450 g L^{-1}. When the desired WCW was reached, methanol induction was initiated with a brief glycerol co-feeding period, resulting in a transition phase where both glycerol and methanol were present. In the third strategy, a glycerol fed-batch phase was initiated at inoculation, and the concentration of glycerol was maintained at 20 g L^{-1} throughout the cell growth period. When the WCW reached 450 g L^{-1}, the glycerol feed was stopped and methanol induction began.

Anion Exchange Chromatography Purification

VP1-NY-ESO-1 was purified via anion exchange chromatography performed on a ÄKTA Explorer (GE Healthcare Life Sciences Piscataway, NJ) via a 5 mL column packed with a strong anion exchange resin, Q Sepharose XL (GE Healthare). Fermentation supernatant was clarified with a 0.22 μm capsule filter (EMD Millipore Corporation, Darmstadt, Germany) followed by concentration and buffer exchange via tangential flow filtration using a 10 kDa membrane (Pall Corporation, Port Washington, NY) into 50 mM phosphate buffer (pH 8.0). The purification scheme consisted of column equilibration

with binding buffer (50 mM phosphate buffer, pH 8.0), followed by washing with binding buffer to remove loosely bound proteins, and VP1-NY-ESO-1 elution step was preformed via a stepwise gradient of elution buffer (binding buffer containing 1 M NaCl).

Protein Determination

Total protein concentration was determined via BCA protein assay according to the manufacturer's protocol (Thermo Fisher Scientific, Waltham, MA). To determine concentrations of NoV VLPs Displaying NY-ESO-1 produced, supernatant samples were purified by sucrose gradient 10-40% via ultracentrifugation 235,500 x g for 4 h at 4°C, as previously described [295, 296]. The UV absorbance of the sucrose gradient purified samples and the extinction coefficient (55725 $M^{-1}cm^{-1}$), estimated based on the protein sequence [297, 298], were used to determine the protein concentration via Beer's law.

Transmission Electron Microscopy Imaging and Dynamic Light Scattering

Fermentation supernatant samples were loaded onto copper mesh grids (Electron Microscopy Sciences, Fort Washington, PA) and stained with 1.5% uranyl acetate. Transmission electron microscopy (TEM) characterization was performed on a F20 FEI Technai 200 kV field transmission electron microscope (FEI, Hillsboro, Oregon). Images were recorded using a Gatan Orius 1000 dual-scan CCD camera at 1-3 s exposure times using Digital Micrograph (DM) software (Gatan, Inc., Pleasanton, CA).

Dynamic light scattering (DLS) measurements of VLPs displaying NYESO-1 were taken using a Zetasizer Nano-ZS (Malvern Instruments Ltd, Worcestershire, UK). The particle size was calculated as the average of six consecutive measurements recorded at 25 ºC.

Off-line Methanol Determination

Off-line measurement of the methanol concentration in fermentation supernatant samples was performed with the Analox GM8 Microstat Analyzer (Analox Instruments,

Lunenburg, MA). Supernatant samples were stored at -80°C until analysis, and run in batches for several fermentations. The analysis methodology was described previously [293, 294].

i.vi. Results and Discussion

High cell density *P. pastoris* fermentations normally include three phases: (1) a glycerol batch phase, where cells grow using glycerol contained in the fermentation medium; (2) a glycerol fed-batch phase, where additional glycerol is added to the fermentation medium to increase cell density; and (3) a methanol fed-batch or induction phase, in which the AOX1 promoter is induced and heterologous protein produced by feeding in methanol at a specified rate [278]. Parameters influencing protein production yield and activity include pH, aeration, cell density, and carbon source feed rate [299, 300]. Here, we varied the methanol concentration during the methanol fed-batch phase, conducted fermentations with and without the glycerol fed-batch phase, and investigated the effect of co-feeding glycerol and methanol during the initial hours of the methanol fed-batch phase.

VP1-NY-ESO-1 Fermentation with On-line Pichia Pastoris Bioprocess Monitor

In this study, the RTBio^{TM} Bioprocess Monitor (ASL Analytical, Inc.) was used for continuous, real-time monitoring and control of glycerol and methanol concentrations during the fermentation, as well as for continuous, real-time monitoring of relative cell density. The bioprocess monitor provided robust control of the methanol and glycerol concentrations during fed-batch periods, and allowed determination of the optimal methanol concentration for induction. The bioprocess monitor also allowed comparison of the cell growth behavior between different fermentation processes.

The bioprocess monitor was equipped with factory calibrations for glycerol, methanol, and relative cell density for the first fermentation. Following this fermentation, the calibrations were tuned for the on-site operating and environmental conditions. These tuned calibrations were utilized for real-time, continuous measurements of glycerol concentration, methanol concentration, and relative cell density for all subsequent fermentations. The tuned calibrations were utilized without modification for the subsequent 10 fermentations completed over the 16-week period of this investigation.

Prior to each fermentation run, quality test standards were analyzed by the bioprocess monitor as a check of calibration performance. These standards consisted of a 40 g L^{-1} glycerol solution, a 15 g L^{-1} methanol solution, and a mixture of 10 g L^{-1} glycerol and 10 g L^{-1} methanol. For each standard, the glycerol and methanol concentrations were measured and compared to the prepared concentrations. The cumulative average and standard deviation for the glycerol and methanol concentrations are given in Table ii.i. These values correspond to the average and standard deviation for 10 separate measurements, representing 10 different fermentations over a period of 16 weeks. Results indicate excellent measurement accuracy and precision for both the glycerol and methanol calibrations.

	Glycerol Concentration (g L^{-1})		Methanol Concentration (g $L^{-1)}$	
	Actual	Measured	Actual	Measured
Glycerol Standard	40.0 ± 0.1	39.7 ± 0.6	0	0.0 ± 0.1
Methanol Standard	0	0.4 ± 0.4	15.0 ± 0.1	14.8 ± 0.2
Mixture Standard	10.0 ± 0.1	10.0 ± 0.2	10.0 ± 0.1	10.0 ± 0.1

Table ii.i Bioprocess monitor results for the quality test standards analyses performed prior to each of 10 fermentations over a 16-week period.

Robustness of the tuned methanol calibration was assessed further by comparing the output from the bioprocess monitor to a conventional off-line method for methanol

concentration determination. This comparison indicated a mean percentage error of 4% for 61 unique samples from 10 different fermentations over a concentration range of 0-12 g L^{-1}.

During fermentation, a peristaltic pump was used to circulate the cell culture broth (containing both growth medium and cells) continuously from the bioreactor, through the bioprocess monitor, and back to the bioreactor within a sealed, sterile process cartridge (Figure ii.i). A near-infrared transmission spectrum of the circulating broth was automatically collected by the monitor every 30 seconds. Values for glycerol concentration, methanol concentration, and relative cell density were determined from analysis of the resulting spectra, and these values were displayed in real-time and recorded throughout the fermentation process [301, 302]. Automated set-point control of glycerol and methanol concentrations was achieved using feed pumps controlled by the monitor using a model-based algorithm [293, 294].

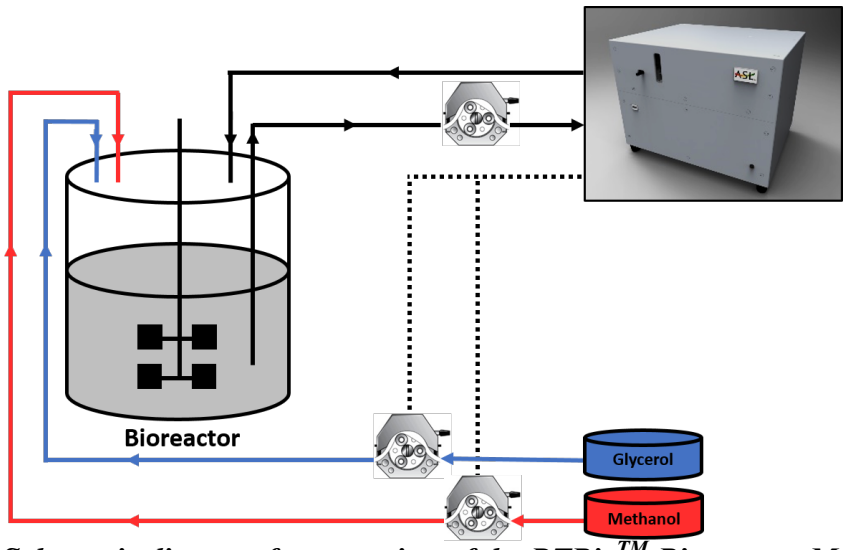

Figure ii.i. Schematic diagram for operation of the RTBio™ Bioprocess Monitor, highlighting the external circulation loop between the bioreactor and monitor as well as the set up for feed control of glycerol and methanol.

Figure ii.ii gives an example of the output provided by the bioprocess monitor. This output consists of profiles for the concentrations of glycerol and methanol, as well as relative cell density. The glycerol profile illustrates how the monitor output is superior to the practice of monitoring DO spikes to identify the point of glycerol depletion at the end of the batch phase. As shown in Figure ii.ii, variations in the DO signal before and after the labeled DO spike confound this information, whereas the bioprocess monitor provides a cleaner and error-free indication. In addition, real-time cell growth profiles like that given in Figure ii.ii provide valuable analytical data that serve to document run-to-run consistency in terms of the rate of cell growth during both the glycerol and methanol phases [30].

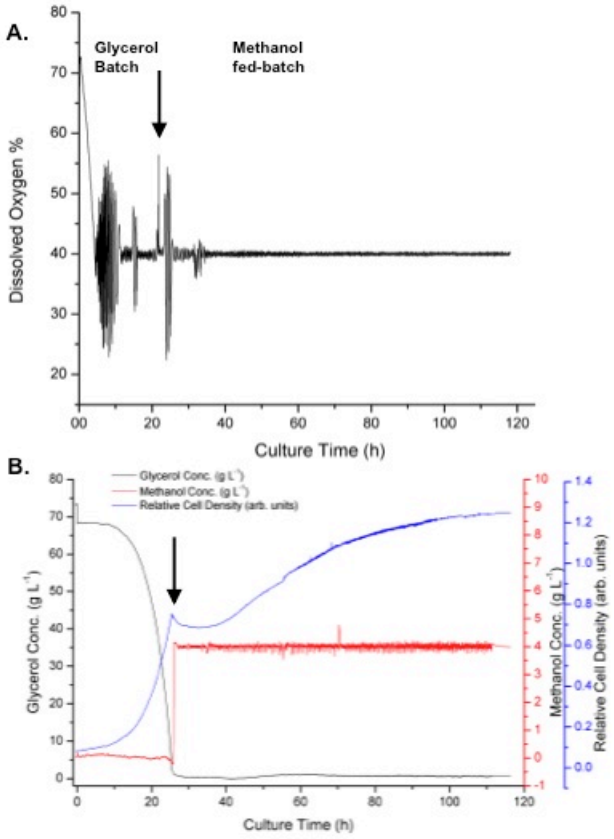

Figure ii.ii. Dissolved oxygen, glycerol concentration, methanol concentration, and relative cell density profiles during a representative limited-batch fermentation of P. pastoris BG-11 expressing the VP1-NY-ESO-construct.

(A.) Dissolved oxygen concentration during the fermentation, with the start of induction corresponding to the DO spike indicated by the arrow. The DO spike signals the exhaustion of glycerol in the medium. (B.) Glycerol concentration (black), methanol concentration (red), and relative cell density (blue) profiles provided by the bioprocess monitor. The start of induction is indicated by the black arrow.

The methanol concentration profile in Figure ii.iiB illustrates the ability of the bioprocess monitor to control the concentration of the carbon sources at a given set point. This capability was used for both, where glycerol concentrations were controlled during fed-batch periods and methanol concentrations were controlled during induction. In both cases, analytical results from the bioprocess monitor were used to control the delivery rate in order to maintain the concentration set point.

Optimization of Methanol Concentration

Methanol feed rate is a crucial process parameter during the induction phase of fermentation. Controlling the methanol concentration prevents toxic levels of methanol and the concomitant accumulation of formaldehyde [303, 304]. Maintaining methanol at a constant concentration is important for optimizing protein yield, as a more stable methanol concentration results in higher productivity [305]. For these studies, the bioprocess monitor provided tight methanol control at different set points while dissolved oxygen, pH, medium composition, temperature, and cell growth conditions were held constant.

The fermentation process scheme for this investigation included two phases, a glycerol-batch phase directly followed by a methanol induction phase. Completion of the glycerol-batch phase was indicated by both the bioprocess monitor and the dissolved oxygen concentration, as a DO spike corresponded to depletion of glycerol in the basal salt medium. The methanol concentration was maintained at a constant level for the entire induction phase using the bioprocess monitor control. Methanol concentrations of 1 g L^{-1}, 4 g L^{-1}, and 7 g L^{-1} were investigated for secreted production of NoV VLPs displaying NY-ESO-1.

Figure ii.iii summarizes the results collected during each of the three fermentations with set methanol concentrations. Relative cell density (Figure ii.iii A) and WCW (Figure ii.iii B) profiles indicate that the rate of cell growth was higher when using a methanol concentration of 4 g L^{-1} compared to the others. The cell growth rate during induction for the 4 g L^{-1} fermentation was 2.25 g L^{-1} h^{-1}, while the growth rates for the 1 g L^{-1} and 7 g L^{-1} fermentations were -0.83 g L^{-1} h^{-1} and 1.75 g L^{-1} h^{-1}, respectively. At a methanol

concentration of 1 g L^{-1}, cells were not able to sustain growth beyond 36 h of induction, as indicated by a decline in the wet cell weight, which resulted in the fermentation being stopped 60 h after induction. The total protein concentration in the supernatant was also highest at a methanol concentration of 4 g L^{-1} (Figure ii.iii C). The 4 g L^{-1} fermentation yielded 4.9 g L^{-1} of total protein secreted in the fermentation medium, while the total protein yields for the 1 g L^{-1} and 7 g L^{-1} fermentations were 2.5 g L^{-1} and 2.56 g L^{-1}, respectively.

Methanol consumption rates for these three fermentations were obtained from the bioprocess monitor, and the measured profiles are presented in Figure ii.iii D. The methanol consumption rate was observed to increase as a function of the methanol set point with the highest rates recorded for the 7 g L^{-1} methanol fermentation. At a methanol concentration of 7 g L^{-1}, the consumption rate steadily increased during induction until reaching a value of 8.2 g L^{-1} h^{-1} 60 h after induction. In contrast, the 4 g L^{-1} methanol fermentation reached a methanol consumption rate of 1.7 g L^{-1} h^{-1} 25 h after induction, and maintained that rate (± 0.2 g L^{-1} h^{-1}) for the remainder of the fermentation. The consumption rate does not appear to correlate directly to an increase in cell growth rate or secreted expression of VP1-NY-ESO-1, given that the highest cell density and total protein concentration was observed for the 4 g L^{-1} methanol fermentation (Figure ii.iii). This may be attributed to an accumulation of the toxic byproducts of methanol metabolism, formaldehyde and hydrogen peroxide, which can be growth limiting [306, 307]. Additionally, the higher methanol consumption rate could result in overproduction of recombinant proteins, thereby overloading the endoplasmic reticulum (ER) folding and secretion capacity which can cause ER stress and result in an unfolded protein response

(UPR) and limited protein secretion [308, 309]. The 4 g L^{-1} methanol concentration was used for further optimization studies as it yielded the highest VP1-NY-ESO-1 concentration, 0.45 g L^{-1}, after 96 h of induction, as well as the highest cell density and growth rate (Figure ii.iii).

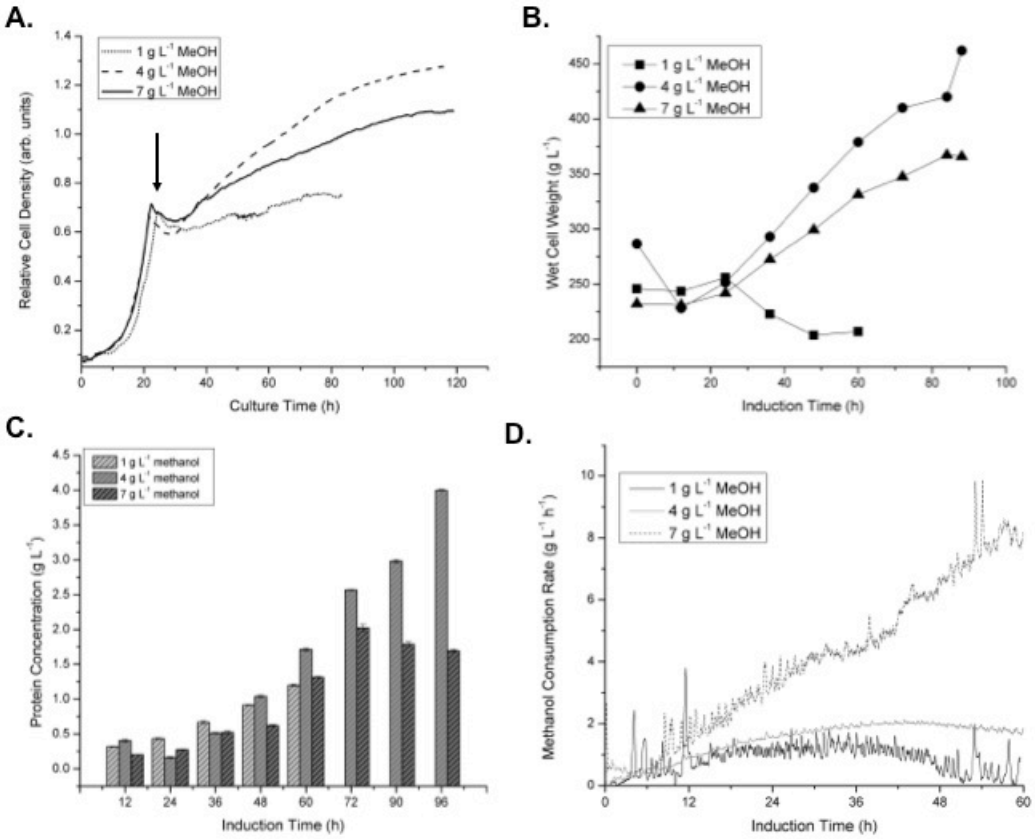

Figure ii.iii Relative cell density, wet cell weight, protein concentration, and methanol consumption rate profiles for the NoV VLP-NY-ESO-1 fermentations at methanol concentrations of 1, 4, and 7 g L^{-1}.
(A.) Relative cell density profiles from the bioprocess monitor for both the batch and induction phases, with the start of induction being indicated by a dip in the profile and marked with an arrow. (B.) Wet cell weight measurements taken during induction. (C.) Total protein measurements taken during induction. (D.) Methanol consumption rates during first the 60 h of induction.

Feed Strategy

To further optimize recombinant expression of the VP1-NY-ESO-1 protein, the effect of elongating the batch phase and the addition of a glycerol transition phase was

investigated. The glycerol batch phase was extended for the purpose of increasing the cell density at the start of induction. The previous limited-batch phase runs began induction with the WCW around 265 g L^{-1}. Here, a glycerol fed-batch phase was used to increase the WCW to approximately 450 g L^{-1} prior to induction. Furthermore, a glycerol transition phase was evaluated as the addition of a mixed-feed transition phase has been shown to increase recombinant protein production in Mut^S *P. pastoris* [310-312]. Previously, the production of *Rhizopus oryzae* lipase in *P. pastoris* was increased 13.6-fold by the introduction of a mixed-feed transition phase [310].

For this investigation, the glycerol-fed batch phase and methanol induction phases were carried out using two methods: (1) Following depletion of glycerol in the initial media, the glycerol concentration was controlled at 10 g L^{-1} until a WCW of approximately 450 g L^{-1} was reached. After the targeted WCW was reached, the set point for the glycerol concentration was reduced to 5 g L^{-1} and induction was initiated with the methanol concentration controlled at 4 g L^{-1}. After one hour, the glycerol concentration set point was lowered to 1 g L^{-1} for 10 min. Afterwards, the glycerol feed control was turned off and the glycerol was allowed to deplete (Figure ii.iv A); and (2) The glycerol concentration was maintained at a constant concentration of 20 g L^{-1} from inoculation until the WCW was above 450 g L^{-1}. Subsequently, induction was initiated with the methanol concentration maintained at 4 g L^{-1}. At this time, the glycerol feed control was turned off and the glycerol was allowed to gradually deplete (Figure ii.iv B). Approximately 38 h into the fermentation, the methanol set point was adjusted from 4 to 6 g L^{-1} and then reset to 4 g L^{-1} after approximately 2 h. This temporary adjustment in the methanol set point was done to determine the ability of the bioprocess monitor to

accurately respond to such adjustments. As indicated in Figure ii.iv B, the methanol concentration rapidly reaches the 6 g L^{-1} set point within 15 min, while 3 h was required to reestablish the 4 g L^{-1} set point. The slower reduction in the methanol concentration is consistent with cellular metabolism being rate limiting.

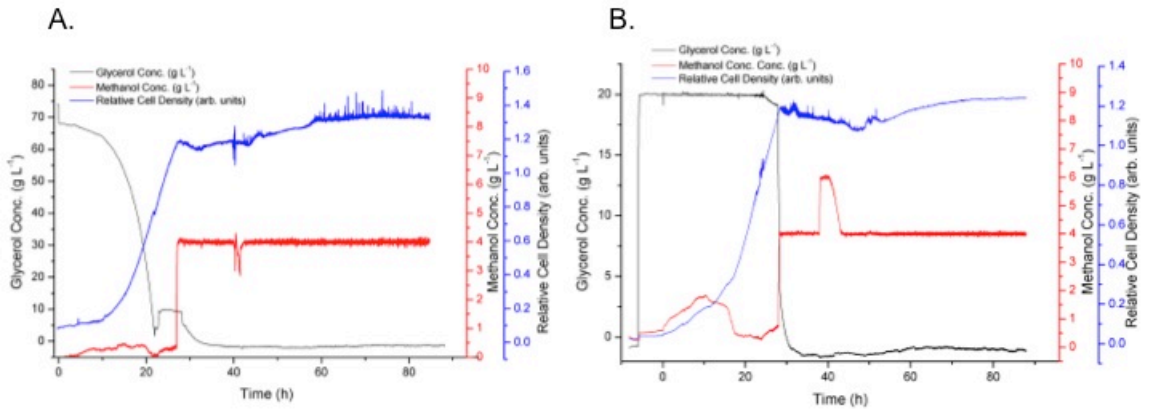

Figure ii.iv Glycerol concentration (black), methanol concentration (red), and relative cell density (blue) profiles for the two different mixed-feed strategies.
(A) Glycerol batch phase followed by a glycerol fed-batch phase with the glycerol concentration controlled at 10 g L^{-1}. Induction with methanol at a constant concentration of 4 g L^{-1} while co-feeding glycerol at a constant concentration of 5 g L^{-1} for 1 h and then 1 g L^{-1} for 10 min before turning off the glycerol feed control and allowing glycerol exhaustion. (B) Glycerol fed-batch phase with the glycerol concentration controlled at 20 g L^{-1} followed by induction with 4 g L^{-1} methanol. The methanol concentration set point was briefly adjusted to 6 g L^{-1} at 38 h, before resuming control at 4 g L^{-1} at 40 h for the remainder of the fermentation.

The total protein concentration profiles for the two different mixed-feed strategies are presented in Figure ii.v A. For comparison, the total protein concentration data for the standard limited-batch fermentation with induction at 4 g L^{-1} methanol are also given. As seen in Figure ii.v A, the total protein concentration was highest for the mixed-feed strategy that incorporated a glycerol transition phase. Thus, higher levels of protein secretion occurred under glycerol transition conditions, which was determined via sucrose gradient to be 0.85 g L^{-1} of VP1-NY-ESO-1 produced after 60 h of induction. The methanol consumption rates and total protein concentrations were also plotted

together for the three different fermentation strategies (Figure ii.v C-E). Similar to the previous methanol consumption rate data for the different induction methanol concentrations (Figure ii.v D), methanol consumption rates do not trend with protein production. The limited-batch fermentation had a higher methanol consumption rate after 60 h than the extended batch runs, but a lower total protein concentration coupled with a lower cell density.

However, in examining the first 15 h of induction, the methanol consumption rate increased more rapidly for the fermentation that included a glycerol transition phase at induction when compared to the other mixed-feed method. As seen in Figure ii.v B, the methanol consumption rate reached 1 g L^{-1} h^{-1} after 6 h of induction for the fermentation including a glycerol transition phase. In contrast, the fermentation run with the 20 g L^{-1} glycerol fed-batch phase did not reach a methanol consumption rate value of 1 g L^{-1} h^{-1} until 14.7 h after induction, though it started off at approximately the same cell density. This difference suggests that the addition of a glycerol transition phase enhanced the induction process and formation of the AOX enzyme.

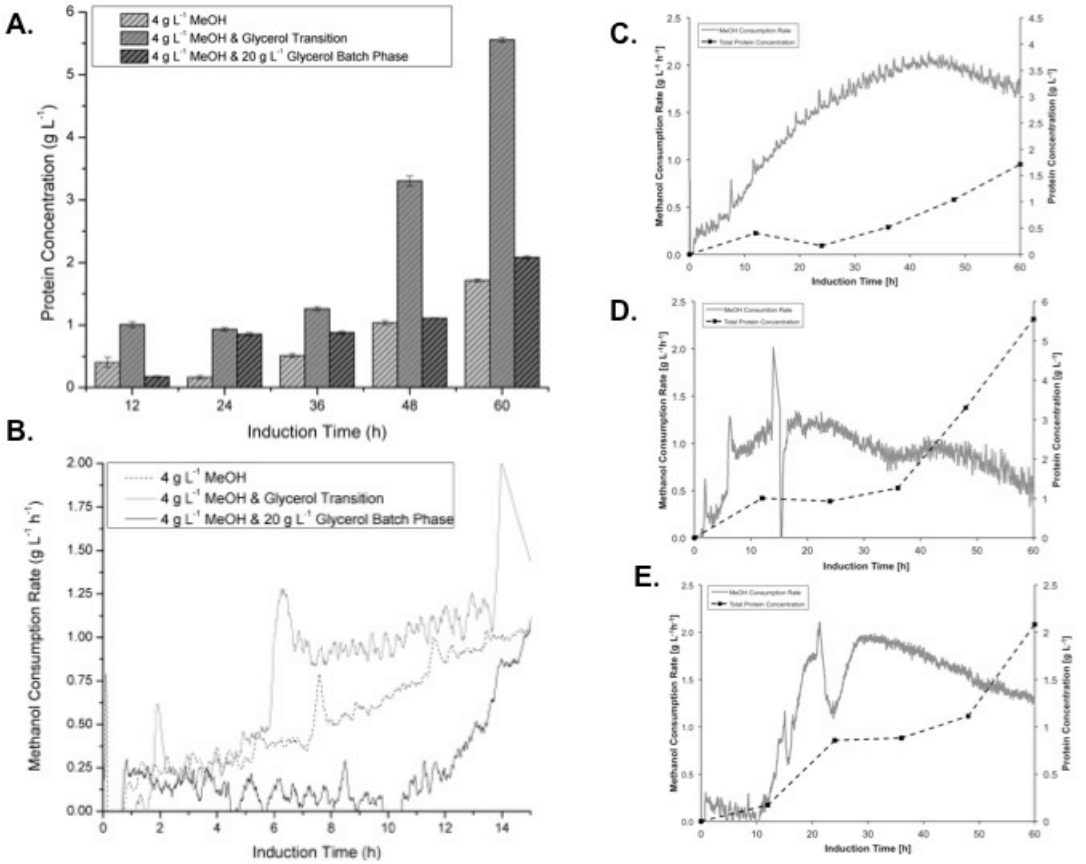

Figure ii.v Total protein concentration and methanol consumption rates for the three different fermentation strategies.

(I) standard limited-batch; (II) batch phase extended with a 10 g L^{-1} glycerol fed-batch phase and a 5 g L^{-1} glycerol transition phase; and (III) glycerol fed-batch at a constant glycerol concentration of 20 g L^{-1}. (A.) Total protein concentration during induction taken at 12 h intervals. (B.) Methanol consumption rate profiles as a function of induction time for the first 15 h of induction. Methanol consumption rate and total protein concentration profiles as a function of induction time for strategies I (C.), II (D.), and III (E).

TEM Imaging and DLS

TEM images of fermentation supernatant were taken to confirm secreted expression and assembling of NoV VLPs displaying NY-ESO-1 (Figure ii.vi). Direct light scattering measurements of the fermentation supernatant were used to further characterize secreted NoV VLPs displaying NY-ESO-1 expression in the fermentation supernatant. The average particle size was determined to be ~ 50-100 nm, and corresponds to the second population presented in Figure ii.vi B. These light scattering measurements were taken directly from raw fermentation samples, thus explaining the observed two distinct populations corresponding to the 10 nm supernatant debris and the larger size population of NoV VLPs displaying NY-ESO-1.

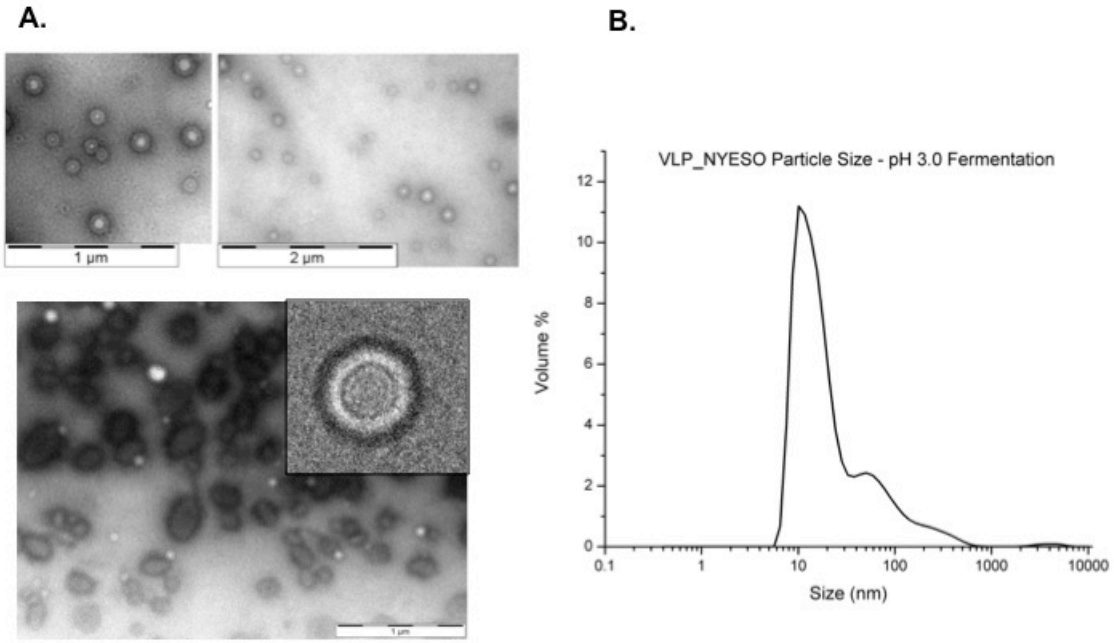

Figure ii.vi (A.) TEM images of the fermentation supernatant. (B.) Dynamic light scattering measurements of NoV VLP-NY-ESO-1 expressed in fermentation supernatant.

Purification

NoV VLPs displaying NY-ESO-1 were purified via anion exchange chromatography. Clarified fermentation supernatant was buffer exchanged with 50 mM sodium phosphate buffer at pH 8.0 and loaded onto a QXL Sepharose column. The protein was eluted using a 3-step gradient of 200 mM, 350 mM, and 1 M NaCl. SDS gel page analysis was used to determine the elution fraction that contained the NoV VLPs. The 73 kDa VP1-NY-ESO-1 band confirmed elution of the NoV VLPs displaying NY-ESO-1 at 350 mM NaCl (Figure ii.vii).

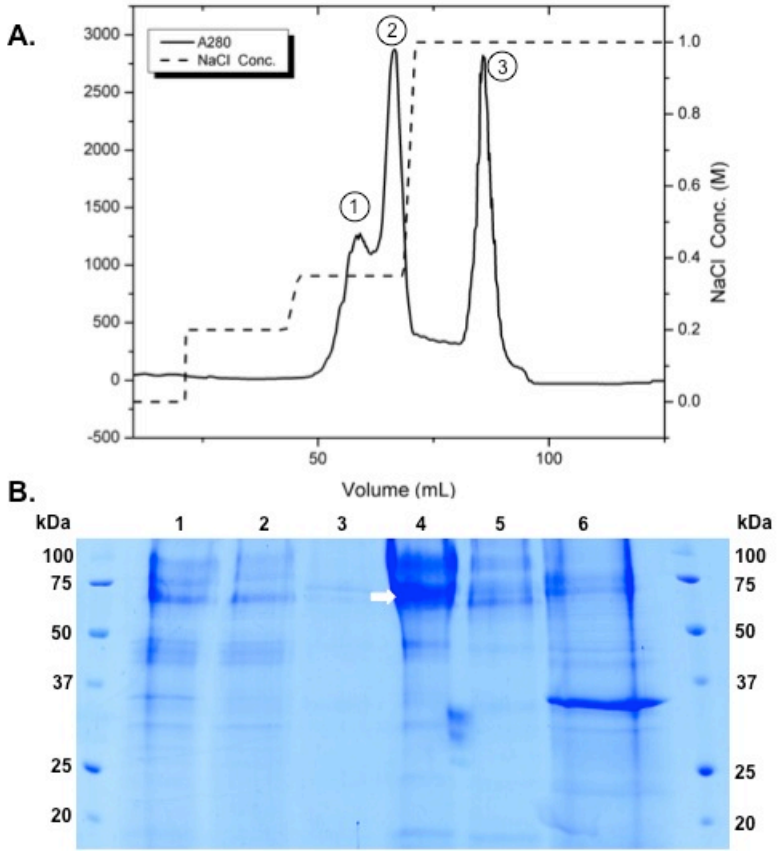

Figure ii.vii NoV VLP-NY-ESO-1 anion exchange chromatography purification.
(A.) Chromatogram of the step-wise gradient elution of the NoV VLPs with three NaCl concentrations (200 mM, 350mM, and 1M). (B.) 15% SDS page gel of the NoV VLP-NY-ESO-1 purification lane 1: Flow through, 2: Wash, 3: Elution Peak 4: Elution Peak 1, 5: Elution Peak 2, 6: Elution Peak 3. The white arrow indicates the 73kDa to NoV VLP-NY-ESO-1 band.

i.vii. Conclusion

Maintaining methanol concentration at optimal levels is critical to protein production in *P. pastoris*. Previous work has reported several methods for methanol feed control including those based on [313]: (1) off-line gas chromatography analysis of fermentation samples; (2) the DO level, where a rapid increase in the DO indicates that the methanol concentration should be increased and vice versa; (3) the specific growth rate [312]; and (4) the detection of the methanol vapor concentration in the exhaust air from the culture by a tin dioxide (SnO_2) semiconductor sensor [314]. The RTBio^{TM} Bioprocess Monitor presents an improvement over these methods as it provides continuous, real-time monitoring and control of both glycerol and methanol concentrations without requiring off-line measurements or being dependent upon fluctuations in the DO concentration, which could negatively impact cell growth. The bioprocess monitor also provides methanol consumption rates which can provide valuable insight into cellular metabolism processes. These analytical features are obtained with minimal user-free operation after an initial straightforward calibration tuning process. Measurement accuracy for glycerol and methanol were determined to be 0.7% and 0.2%, respectively, from a set of quality test standards implemented at the beginning of each fermentation over the 16-week period of this investigation.

In this study, the RTBio^{TM} Bioprocess Monitor was used to optimize the production of NoV VLPs displaying NY-ESO-1 tumor associated antigen expressed and secreted in *P. pastoris.* Optimization of the induction phase methanol concentration and the batch phase time, as well as inclusion of a glycerol transition phase, resulted in the maximum NoV VP1-NY-ESO-1 yield of 0.85 g L^{-1}. Previous work in the area of optimization of

recombinant VLP production have reported yields ranging from 0.3 g L^{-1} in *P. pastoris* [315] to 0.18 g L^{-1} in *E. coli*. The three-fold increase in yield presented here (0.85 g L^{-1}) represents a major advance compared to these previous reports. This level of improvement was achieved via tight control of the glycerol and methanol concentrations during both batch and induction phases, respectively, as well as through real-time monitoring of the cell growth during the batch phase.

The first parameter that was optimized in this investigation, was the induction phase methanol concentration, and a 4 g L^{-1} methanol concentration was determined to be optimal among the three concentrations investigated (1 g L^{-1}, 4 g L^{-1}, and 7 g L^{-1}). Secondly, the fermentation process scheme was optimized by extending the batch phase time and adding a glycerol transition phase at induction. This mixed-feed strategy increased the yield of NoV VLPs displaying NY-ESO-1 and reduced the induction time required to produce a substantial amount of recombinant NoV VLPs. However, increasing the batch time alone without addition of the glycerol transition only slightly increased the total protein yield (Figure 6A). This finding indicates that the critical factor to increasing protein production is the co-feed of glycerol during the transition phase. Methanol consumption rate data provide evidence that substantial concentrations of glycerol during the transition phase reduces the time required for the cells to switch over to methanol metabolism.

i.viii. Acknowledgements

This work made use of the Cornell Center for Materials Research Shared Facilities supported through the NSF MRSEC program (DMR-1120296). ASL Analytical Inc., 2500 Crosspark Rd, Coralville, IA 52241, USA.

REFERENCES

1. Siegel, R., D. Naishadham, and A. Jemal, *Cancer statistics, 2013.* CA: A Cancer Journal for Clinicians, 2013. **63**(1): p. 11-30.
2. Kochanek KD, X.J., Murphy SL, Minino AM, Kung HC., *Deaths: final data for 2009.* Natl Vital Stat Rep., 2011(60): p. 1-117.
3. Holohan, C., et al., *Cancer drug resistance: an evolving paradigm.* Nat Rev Cancer, 2013. **13**(10): p. 714-726.
4. Hull, L.C., D. Farrell, and P. Grodzinski, *Highlights of recent developments and trends in cancer nanotechnology research—View from NCI Alliance for Nanotechnology in Cancer.* Biotechnology Advances, 2014. **32**(4): p. 666-678.
5. Curry, T., et al., *Multifunctional theranostic gold nanoparticles for targeted CT imaging and photothermal therapy.* Contrast Media & Molecular Imaging, 2014. **9**(1): p. 53-61.
6. Julien, D.C., et al., *Utilization of monoclonal antibody-targeted nanomaterials in the treatment of cancer.* MAbs, 2011. **3**(5): p. 467-78.
7. He, X., K. Wang, and Z. Cheng, *In vivo near-infrared fluorescence imaging of cancer with nanoparticle-based probes.* Wiley Interdisciplinary Reviews: Nanomedicine and Nanobiotechnology, 2010. **2**(4): p. 349-366.
8. Chow, E.K.-H. and D. Ho, *Cancer Nanomedicine: From Drug Delivery to Imaging.* Science Translational Medicine, 2013. **5**(216): p. 216rv4.
9. Alivisatos, P., *The use of nanocrystals in biological detection.* Nat Biotech, 2004. **22**(1): p. 47-52.

10. Thakor, A.S., et al., *Gold Nanoparticles: A Revival in Precious Metal Administration to Patients.* Nano Letters, 2011. **11**(10): p. 4029-4036.

11. Cai, W., et al., *Applications of gold nanoparticles in cancer nanotechnology.* Nanotechnology, science and applications, 2008. **2008**(1): p. 10.2147/NSA.S3788.

12. Heddle, J., *Gold Nanoparticle-Biological Molecule Interactions and Catalysis.* Catalysts, 2013. **3**(3): p. 683-708.

13. Huang, X.H., et al., *Gold nanoparticles: interesting optical properties and recent applications in cancer diagnostic and therapy.* Nanomedicine, 2007. **2**(5): p. 681-693.

14. Huang, X. and M.A. El-Sayed, *Gold nanoparticles: Optical properties and implementations in cancer diagnosis and photothermal therapy.* Journal of Advanced Research, 2010. **1**(1): p. 13-28.

15. Ku, K.H., et al., *Aspect Ratio Effect of Nanorod Surfactants on the Shape and Internal Morphology of Block Copolymer Particles.* Journal of Polymer Science Part a-Polymer Chemistry, 2015. **53**(2): p. 188-192.

16. Cao-Milan, R. and L.M. Liz-Marzan, *Gold nanoparticle conjugates: recent advances toward clinical applications.* Expert Opinion on Drug Delivery, 2014. **11**(5): p. 741-752.

17. Zhou, J., et al., *Functionalized gold nanoparticles: Synthesis, structure and colloid stability.* Journal of Colloid and Interface Science, 2009. **331**(2): p. 251-262.

18. Fratoddi, I., et al., *Gold nanoparticles and gold nanoparticle-conjugates for delivery of therapeutic molecules. Progress and challenges.* Journal of Materials Chemistry B, 2014. **2**(27): p. 4204-4220.

19. Dykman, L. and N. Khlebtsov, *Gold nanoparticles in biomedical applications: recent advances and perspectives.* Chem Soc Rev, 2012. **41**(6): p. 2256-82.

20. Klein, S., et al., *Quantitative visualization of colloidal and intracellular gold nanoparticles by confocal microscopy.* Journal of Biomedical Optics, 2010. **15**(3): p. 036015-036015-11.

21. van Dijk, M.A., et al., *Absorption and scattering microscopy of single metal nanoparticles.* Physical Chemistry Chemical Physics, 2006. **8**(30): p. 3486-3495.

22. Tcherniak, A., et al., *Probing a Century Old Prediction One Plasmonic Particle at a Time.* Nano Letters, 2010. **10**(4): p. 1398-1404.

23. Dreaden, E.C., et al., *The golden age: gold nanoparticles for biomedicine.* Chemical Society Reviews, 2012. **41**(7): p. 2740-2779.

24. Cho, S.J., et al., *Growth mechanisms and oxidation resistance of gold-coated iron nanoparticles.* Chemistry of Materials, 2005. **17**(12): p. 3181-3186.

25. Teja, A.S. and P.-Y. Koh, *Synthesis, properties, and applications of magnetic iron oxide nanoparticles.* Progress in Crystal Growth and Characterization of Materials, 2009. **55**(1–2): p. 22-45.

26. Wang, D., et al., *Superparamagnetic Fe2O3 Beads−CdSe/ZnS Quantum Dots Core−Shell Nanocomposite Particles for Cell Separation.* Nano Letters, 2004. **4**(3): p. 409-413.

27. Rosen, J.E., et al., *Iron oxide nanoparticles for targeted cancer imaging and diagnostics.* Nanomedicine: Nanotechnology, Biology and Medicine, 2012. **8**(3): p. 275-290.

28. Wang, Y.-X., S. Hussain, and G. Krestin, *Superparamagnetic iron oxide contrast agents: physicochemical characteristics and applications in MR imaging.* European Radiology, 2001. **11**(11): p. 2319-2331.

29. Wang, Y.X., *Superparamagnetic iron oxide based MRI contrast agents: Current status of clinical application.* Quant Imaging Med Surg, 2011. **1**(1): p. 35-40.

30. Clement, O., et al., *Liver tumors in cirrhosis: experimental study with SPIO-enhanced MR imaging.* Radiology, 1991. **180**(1): p. 31-6.

31. Deryl, L.T. and H.B. Stefan, *Utilization of Magnetic Nanoparticles for Cancer Therapy*, in *Nanomedicine and Cancer*. 2011, Science Publishers.

32. Kim, J., et al., *Designed Fabrication of Multifunctional Magnetic Gold Nanoshells and Their Application to Magnetic Resonance Imaging and Photothermal Therapy.* Angewandte Chemie, 2006. **118**(46): p. 7918-7922.

33. Wang, L.Y., et al., *Monodispersed core-shell Fe3O4@Au nanoparticles.* Journal of Physical Chemistry B, 2005. **109**(46): p. 21593-21601.

34. Melancon, M.P., et al., *Targeted multifunctional gold-based nanoshells for magnetic resonance-guided laser ablation of head and neck cancer.* Biomaterials, 2011. **32**(30): p. 7600-7608.

35. Li, L., et al., *Synthesis and Morphology Control of Gold/Iron Oxide Magnetic Nanocomposites via a Simple Aqueous Method.* Ieee Transactions on Magnetics, 2014. **50**(1).

36. Li, L., et al., *Novel Hybrid Au/Fe3O4 Magnetic Octahedron-like Nanoparticles with Tunable Size.* Ieee Transactions on Magnetics, 2014. **50**(1).

37. Xu, Z., Y. Hou, and S. Sun, *Magnetic Core/Shell Fe3O4/Au and Fe3O4/Au/Ag Nanoparticles with Tunable Plasmonic Properties.* Journal of the American Chemical Society, 2007. **129**(28): p. 8698-8699.

38. Lyon, J.L., et al., *Synthesis of Fe Oxide Core/Au Shell Nanoparticles by Iterative Hydroxylamine Seeding.* Nano Letters, 2004. **4**(4): p. 719-723.

39. Yu, H., et al., *Dumbbell-like Bifunctional Au−Fe3O4 Nanoparticles.* Nano Letters, 2005. **5**(2): p. 379-382.

40. Kirui, D.K., D.A. Rey, and C.A. Batt, *Gold hybrid nanoparticles for targeted phototherapy and cancer imaging.* Nanotechnology, 2010. **21**(10): p. 105105.

41. Barnett, C.M., et al., *Physical stability, biocompatibility and potential use of hybrid iron oxide-gold nanoparticles as drug carriers.* Journal of Nanoparticle Research, 2013. **15**(6).

42. Mezni, A., et al., *Hybrid Au-Fe3O4 Nanoparticles: Plasmonic, Surface Enhanced Raman Scattering, and Phase Transition Properties.* Journal of Physical Chemistry C, 2013. **117**(31): p. 16166-16174.

43. Shevchenko, E.V., et al., *Gold/Iron Oxide Core/Hollow-Shell Nanoparticles.* Advanced Materials, 2008. **20**(22): p. 4323-4329.

44. Park, H.Y., et al., *Fabrication of magnetic core @ shell Fe oxide @ Au nanoparticles for interfacial bioactivity and bio-separation.* Langmuir, 2007. **23**(17): p. 9050-9056.

45. Gautier, J., et al., *Recent advances in theranostic nanocarriers of doxorubicin based on iron oxide and gold nanoparticles.* Journal of Controlled Release, 2013. **169**(1-2): p. 48-61.

46. Zavisova, V., et al., *The cytotoxicity of iron oxide nanoparticles with different modifications evaluated in vitro.* Journal of Magnetism and Magnetic Materials, 2015. **380**(0): p. 85-89.

47. Tiwari, P.M., et al., *Enhanced intracellular translocation and biodistribution of gold nanoparticles functionalized with a cell-penetrating peptide (VG-21) from vesicular stomatitis virus.* Biomaterials, 2014. **35**(35): p. 9484-9494.

48. Bogdanov, A.A., et al., *Gold Nanoparticles Stabilized with MPEG-Grafted Poly(L-lysine): in Vitro and in Vivo Evaluation of a Potential Theranostic Agent.* Bioconjugate Chemistry, 2015. **26**(1): p. 39-50.

49. Choi, Y.-W., et al., *Colloidal stability of iron oxide nanoparticles with multivalent polymer surfactants.* Journal of Colloid and Interface Science, 2015. **443**: p. 8-12.

50. Maldonado, C.R., et al., *Nano-functionalization of metal complexes for molecular imaging and anticancer therapy.* Coordination Chemistry Reviews, 2013. **257**(19–20): p. 2668-2688.

51. Aryal, S., et al., *Spectroscopic identification of S-Au interaction in cysteine capped gold nanoparticles.* Spectrochimica Acta Part a-Molecular and Biomolecular Spectroscopy, 2006. **63**(1): p. 160-163.

52. Gupta, R.K., M.P. Srinivasan, and R. Dharmarajan, *Synthesis of short chain thiol capped gold nanoparticles, their stabilization and immobilization on silicon*

surface. Colloids and Surfaces a-Physicochemical and Engineering Aspects, 2011. **390**(1-3): p. 149-156.

53. Gupta, R.K., M.P. Srinivasan, and R. Dharmarajan, *Synthesis of 16-Mercaptohexadecanoic acid capped gold nanoparticles and their immobilization on a substrate.* Materials Letters, 2012. **67**(1): p. 315-319.

54. Lavenn, C., et al., *Synthesis, characterization and optical properties of an amino-functionalized gold thiolate cluster: Au-10(SPh-pNH(2))(10).* Journal of Colloid and Interface Science, 2014. **418**: p. 234-239.

55. Lin, S.Y., et al., *Two-step functionalization of neutral and positively charged thiols onto citrate-stabilized Au nanoparticles.* Journal of Physical Chemistry B, 2004. **108**(7): p. 2134-2139.

56. Zhou, J.F., et al., *Colloid stability of thymine-functionalized gold nanoparticles.* Langmuir, 2007. **23**(24): p. 12096-12103.

57. Tan, H., T. Zhan, and W.Y. Fan, *Direct functionalization of the hydroxyl group of the 6-mercapto-1-hexanol (MCH) ligand attached to gold nanoclusters.* Journal of Physical Chemistry B, 2006. **110**(43): p. 21690-21693.

58. Yoo, C.I., et al., *A Facile One-Pot Synthesis of Hydroxyl-Functionalized Gold Polyhedrons by a Surface Regulating Copolymer.* Chemistry of Materials, 2009. **21**(5): p. 939-944.

59. Goren, M., N. Galley, and R.B. Lennox, *Adsorption of alkylthiol-capped gold nanoparticles onto alkylthiol self-assembled monolayers: An SPR study.* Langmuir, 2006. **22**(3): p. 1048-1054.

60. Hofmann, A., et al., *Controlled Formation of Gold Nanoparticle Dimers Using Multivalent Thiol Ligands.* Langmuir, 2011. **27**(24): p. 15165-15175.

61. Shichibu, Y., et al., *Large-scale synthesis of thiolated Au-25 clusters via ligand exchange reactions of phosphine-stabilized Au-11 clusters.* Journal of the American Chemical Society, 2005. **127**(39): p. 13464-13465.

62. Woehrle, G.H., L.O. Brown, and J.E. Hutchison, *Thiol-functionalized, 1.5-nm gold nanoparticles through ligand exchange reactions: Scope and mechanism of ligand exchange.* Journal of the American Chemical Society, 2005. **127**(7): p. 2172-2183.

63. Davis, K., et al., *Quantitative Measurement of Ligand Exchange on Iron Oxides via Radiolabeled Oleic Acid.* Langmuir, 2014. **30**(36): p. 10918-10925.

64. Hofmann, A., et al., *Highly monodisperse water-dispersable iron oxide nanoparticles for biomedical applications.* Journal of Materials Chemistry, 2010. **20**(36): p. 7842-7853.

65. Shem, P.M., R. Sardar, and J.S. Shumaker-Parry, *One-Step Synthesis of Phosphine-Stabilized Gold Nanoparticles Using the Mild Reducing Agent 9-BBN.* Langmuir, 2009. **25**(23): p. 13279-13283.

66. Scaravelli, R.C.B., et al., *Direct synthesis of coated gold nanoparticles mediated by polymers with amino groups.* Journal of Colloid and Interface Science, 2013. **397**: p. 114-121.

67. Wang, X.G., et al., *Amphiphilic block copolymer-stabilized gold nanoparticles for aerobic oxidation of alcohols in aqueous solution.* Chemical Communications, 2008(37): p. 4442-4444.

68. Rey, D.A., et al., *In vitro Self-Assembly of Gold Nanoparticle-Coated Poly(3-hydroxybutyrate) Granules Exhibiting Plasmon-Induced Thermo-Optical Enhancements.* Acs Applied Materials & Interfaces, 2010. **2**(7): p. 1804-1810.

69. Xu, S.Y., et al., *Self-assembling gold nanoparticles on thiol-functionalized poly(styrene-co-acrylic acid) nanospheres for fabrication of a mediatorless biosensor.* Analytica Chimica Acta, 2006. **570**(2): p. 151-157.

70. Fuentes, M., et al., *Preparation of inert magnetic nano-particles for the directed immobilization of antibodies.* Biosensors and Bioelectronics, 2005. **20**(7): p. 1380-1387.

71. Almeida, J.P.M., E.R. Figueroa, and R.A. Drezek, *Gold nanoparticle mediated cancer immunotherapy.* Nanomedicine: Nanotechnology, Biology and Medicine, 2014. **10**(3): p. 503-514.

72. Huang, G., et al., *A Novel Strategy for Surface Modification of Superparamagnetic Iron Oxide Nanoparticles for Lung Cancer Imaging.* J Mater Chem, 2009. **19**: p. 6367-6372.

73. Chen, H.W., et al., *Thiol-reactive amphiphilic block copolymer for coating gold nanoparticles with neutral and functionable surfaces.* Polymer Chemistry, 2014. **5**(8): p. 2768-2773.

74. Bloemen, M., et al., *Improved functionalization of oleic acid-coated iron oxide nanoparticles for biomedical applications.* Journal of Nanoparticle Research, 2012. **14**(9): p. 1-10.

75. von Maltzahn, G., et al., *Computationally Guided Photothermal Tumor Therapy Using Long-Circulating Gold Nanorod Antennas.* Cancer Research, 2009. **69**(9): p. 3892-3900.

76. Zhang, S., et al., *Thiol-PEG-carboxyl-stabilized Fe2O3/Au nanoparticles targeted to CD105: Synthesis, characterization and application in MR imaging of tumor angiogenesis.* European Journal of Radiology, 2014. **83**(7): p. 1190-1198.

77. Tassa, C., S.Y. Shaw, and R. Weissleder, *Dextran-Coated Iron Oxide Nanoparticles: A Versatile Platform for Targeted Molecular Imaging, Molecular Diagnostics, and Therapy.* Accounts of Chemical Research, 2011. **44**(10): p. 842-852.

78. Li, S., H. Liu, and N. He, *Covalent binding of streptavidin on gold magnetic nanoparticles for bead array fabrication.* J Nanosci Nanotechnol, 2010. **10**(8): p. 4875-82.

79. Giaume, D., et al., *Organic functionalization of luminescent oxide nanoparticles toward their application as biological probes.* Langmuir, 2008. **24**(19): p. 11018-26.

80. Erathodiyil, N. and J.Y. Ying, *Functionalization of Inorganic Nanoparticles for Bioimaging Applications.* Accounts of Chemical Research, 2011. **44**(10): p. 925-935.

81. Graf, C., et al., *A general method to coat colloidal particles with silica.* Langmuir, 2003. **19**(17): p. 6693-6700.

82. Liberman, A., et al., *Synthesis and surface functionalization of silica nanoparticles for nanomedicine.* Surface Science Reports, 2014. **69**(2–3): p. 132-158.

83. Guerrero-Martínez, A., J. Pérez-Juste, and L.M. Liz-Marzán, *Recent Progress on Silica Coating of Nanoparticles and Related Nanomaterials.* Advanced Materials, 2010. **22**(11): p. 1182-1195.

84. Ladj, R., et al., *Polymer encapsulation of inorganic nanoparticles for biomedical applications.* International Journal of Pharmaceutics, 2013. **458**(1): p. 230-241.

85. Gun, S., M. Edirisinghe, and E. Stride, *Encapsulation of superparamagnetic iron oxide nanoparticles in poly-(lactide-co-glycolic acid) microspheres for biomedical applications.* Materials Science and Engineering: C, 2013. **33**(6): p. 3129-3137.

86. Boisselier, E., et al., *Encapsulation and Stabilization of Gold Nanoparticles with "Click" Polyethyleneglycol Dendrimers.* Journal of the American Chemical Society, 2010. **132**(8): p. 2729-2742.

87. Li, K. and B. Liu, *Polymer encapsulated conjugated polymer nanoparticles for fluorescence bioimaging.* Journal of Materials Chemistry, 2012. **22**(4): p. 1257-1264.

88. Fratila, R.M., et al., *Strategies for the Biofunctionalization of Gold and Iron Oxide Nanoparticles.* Langmuir, 2014.

89. Sperling, R.A. and W.J. Parak, *Surface modification, functionalization and bioconjugation of colloidal inorganic nanoparticles.* Philosophical Transactions

of the Royal Society A: Mathematical, Physical and Engineering Sciences, 2010. **368**(1915): p. 1333-1383.

90. Rayavarapu, R.G., et al., *Synthesis and Bioconjugation of Gold Nanoparticles as Potential Molecular Probes for Light-Based Imaging Techniques.* International Journal of Biomedical Imaging, 2007. **2007**: p. 10.

91. Puertas, S., et al., *Taking Advantage of Unspecific Interactions to Produce Highly Active Magnetic Nanoparticle−Antibody Conjugates.* ACS Nano, 2011. **5**(6): p. 4521-4528.

92. Chinol, M., et al., *Biochemical modifications of avidin improve pharmacokinetics and biodistribution, and reduce immunogenicity.* Br J Cancer, 1998. **78**(2): p. 189-97.

93. Cheung, N.K., et al., *Single-chain Fv-streptavidin substantially improved therapeutic index in multistep targeting directed at disialoganglioside GD2.* J Nucl Med, 2004. **45**(5): p. 867-77.

94. Tajima, N., M. Takai, and K. Ishihara, *Significance of Antibody Orientation Unraveled: Well-Oriented Antibodies Recorded High Binding Affinity.* Analytical Chemistry, 2011. **83**(6): p. 1969-1976.

95. Colombo, M., et al., *Site-Specific Conjugation of ScFvs Antibodies to Nanoparticles by Bioorthogonal Strain-Promoted Alkyne–Nitrone Cycloaddition.* Angewandte Chemie International Edition, 2012. **51**(2): p. 496-499.

96. Hutchins, B.M., et al., *Site-Specific Coupling and Sterically Controlled Formation of Multimeric Antibody Fab Fragments with Unnatural Amino Acids.* Journal of Molecular Biology, 2011. **406**(4): p. 595-603.

97. Ackerson, C.J., et al., *Rigid, Specific, and Discrete Gold Nanoparticle/Antibody Conjugates.* Journal of the American Chemical Society, 2006. **128**(8): p. 2635-2640.

98. Scott, A.M., *Specific targeting, biodistribution and lack of immunogenicity of chimeric anti-GD3 monoclonal antibody KM871 in patients with metastatic melanoma — results of a Phase I trial.* J. Clin. Oncol., 2001. **19**: p. 3976-3987.

99. Nelson, A.L., *Development trends for human monoclonal antibody therapeutics.* Nature Rev. Drug Discov., 2010. **9**: p. 767-774.

100. Reichert, J.M., *Monoclonal antibodies as innovative therapeutics.* Curr Pharm Biotechnol, 2008. **9**(6): p. 423-30.

101. Weiner, L.M., R. Surana, and S. Wang, *Monoclonal antibodies: versatile platforms for cancer immunotherapy.* Nature Rev. Immunol., 2010. **10**: p. 317-327.

102. Alderson, K.L. and P.M. Sondel, *Clinical cancer therapy by NK cells via antibody-dependent cell-mediated cytotoxicity.* J Biomed Biotechnol, 2011. **379123**(10): p. 24.

103. *Drugs@FDA FDA Approved Drugs*, 2014.

104. Davis, M.E., Z. Chen, and D.M. Shin, *Nanoparticle therapeutics: an emerging treatment modality for cancer.* Nat Rev Drug Discov, 2008. **7**(9): p. 771-782.

105. Parker, S.A., et al., *Design, production, and characterization of a single-chain variable fragment (ScFv) derived from the prostate specific membrane antigen (PSMA) monoclonal antibody J591.* Protein Expr Purif, 2013. **89**(2): p. 136-45.

106. Huang, X., et al., *Magnetic Fe3O4 nanoparticles grafted with single-chain antibody (scFv) and docetaxel loaded β-cyclodextrin potential for ovarian cancer dual-targeting therapy.* Materials Science and Engineering: C, 2014. **42**: p. 325-332.

107. Liu, Y., et al., *Single chain fragment variable recombinant antibody functionalized gold nanoparticles for a highly sensitive colorimetric immunoassay.* Biosensors and Bioelectronics, 2009. **24**(9): p. 2853-2857.

108. Lee, N., et al., *Magnetosome-like ferrimagnetic iron oxide nanocubes for highly sensitive MRI of single cells and transplanted pancreatic islets.* Proceedings of the National Academy of Sciences, 2011. **108**(7): p. 2662-2667.

109. Jain, P.K., I.H. El-Sayed, and M.A. El-Sayed, *Au nanoparticles target cancer.* Nano Today, 2007. **2**(1): p. 18-29.

110. Lima, K.M.G., et al., *Environmentally compatible bioconjugated gold nanoparticles as efficient contrast agents for colorectal cancer cell imaging.* Sensors and Actuators B: Chemical, 2014. **196**(0): p. 306-313.

111. Luo, S., et al., *A review of NIR dyes in cancer targeting and imaging.* Biomaterials, 2011. **32**(29): p. 7127-7138.

112. Altinoglu, E.I. and J.H. Adair, *Near infrared imaging with nanoparticles.* Wiley Interdiscip Rev Nanomed Nanobiotechnol, 2010. **2**(5): p. 461-77.

113. Murphy, C.J., et al., *Gold Nanoparticles in Biology: Beyond Toxicity to Cellular Imaging.* Accounts of Chemical Research, 2008. **41**(12): p. 1721-1730.

114. Lee, C.N., et al., *Super-paramagnetic iron oxide nanoparticles for use in extrapulmonary tuberculosis diagnosis.* Clinical Microbiology and Infection, 2012. **18**(6): p. E149-E157.

115. Skaat, H., et al., *Antibody-conjugated, dual-modal, near-infrared fluorescent iron oxide nanoparticles for antiamyloidgenic activity and specific detection of amyloid-beta fibrils.* Int J Nanomedicine, 2013. **8**: p. 4063-76.

116. Sokolov, K., et al., *Real-Time Vital Optical Imaging of Precancer Using Anti-Epidermal Growth Factor Receptor Antibodies Conjugated to Gold Nanoparticles.* Cancer Research, 2003. **63**(9): p. 1999-2004.

117. Schol, D., et al., *Anti-PSMA antibody-coupled gold nanorods detection by optical and electron microscopies.* Micron, 2013. **50**: p. 68-74.

118. Hainfeld, J.F., et al., *Micro-CT enables microlocalisation and quantification of Her2-targeted gold nanoparticles within tumour regions.* Br J Radiol, 2011. **84**(1002): p. 526-33.

119. Coughlin, A.J., et al., *Gadolinium-Conjugated Gold Nanoshells for Multimodal Diagnostic Imaging and Photothermal Cancer Therapy.* Small, 2014. **10**(3): p. 556-565.

120. Lee, N., et al., *Water-Dispersible Ferrimagnetic Iron Oxide Nanocubes with Extremely High r2 Relaxivity for Highly Sensitive in Vivo MRI of Tumors.* Nano Letters, 2012. **12**(6): p. 3127-3131.

121. Serda, R.E., et al., *Targeting and cellular trafficking of magnetic nanoparticles for prostate cancer imaging.* Mol Imaging, 2007. **6**(4): p. 277-88.

122. Kao, H.W., et al., *Evaluation of EGFR-targeted radioimmuno-gold-nanoparticles as a theranostic agent in a tumor animal model.* Bioorg Med Chem Lett, 2013. **23**(11): p. 3180-5.

123. Gong, T., et al., *Engineering bioconjugated gold nanospheres and gold nanorods as label-free plasmon scattering probes for ultrasensitive multiplex dark-field imaging of cancer cells.* J Biomed Nanotechnol, 2013. **9**(6): p. 985-91.

124. Choi, W.I., et al., *Targeted antitumor efficacy and imaging via multifunctional nano-carrier conjugated with anti-HER2 trastuzumab.* Nanomedicine, 2015. **11**(2): p. 359-68.

125. Karmani, L., et al., *Zr-89-labeled anti-endoglin antibody-targeted gold nanoparticles for imaging cancer: implications for future cancer therapy.* Nanomedicine, 2014. **9**(13): p. 1923-1937.

126. Chen, T.J., et al., *Targeted Herceptin-dextran iron oxide nanoparticles for noninvasive imaging of HER2/neu receptors using MRI.* J Biol Inorg Chem, 2009. **14**(2): p. 253-60.

127. Vertrees, R.A., et al., *Synergistic interaction of hyperthermia and Gemcitabine in lung cancer.* Cancer Biol Ther, 2005. **4**(10): p. 1144-53.

128. Hildebrandt, B., et al., *The cellular and molecular basis of hyperthermia.* Crit Rev Oncol Hematol, 2002. **43**(1): p. 33-56.

129. Ito, A., H. Honda, and T. Kobayashi, *Cancer immunotherapy based on intracellular hyperthermia using magnetite nanoparticles: a novel concept of "heat-controlled necrosis" with heat shock protein expression.* Cancer Immunol Immunother, 2006. **55**(3): p. 320-8.

130. Chae, S.Y., et al., *High-Intensity Focused Ultrasound-Induced, Localized Mild Hyperthermia to Enhance Anti-cancer Efficacy of Systemic Doxorubicin: An Experimental Study.* Ultrasound in Medicine & Biology, 2014. **40**(7): p. 1554-1563.

131. Overgaard, J., et al., *Randomised trial of hyperthermia as adjuvant to radiotherapy for recurrent or metastatic malignant melanoma. European Society for Hyperthermic Oncology.* Lancet, 1995. **345**(8949): p. 540-3.

132. Roa, W., et al., *Gold nanoparticle sensitize radiotherapy of prostate cancer cells by regulation of the cell cycle.* Nanotechnology, 2009. **20**(37): p. 0957-4484.

133. Atkinson, R.L., et al., *Thermal enhancement with optically activated gold nanoshells sensitizes breast cancer stem cells to radiation therapy.* Sci Transl Med, 2010. **2**(55): p. 3001447.

134. Kampinga, H.H., *Cell biological effects of hyperthermia alone or combined with radiation or drugs: A short introduction to newcomers in the field.* International Journal of Hyperthermia, 2006. **22**(3): p. 191-196.

135. Cui, Z.-G., et al., *Molecular mechanisms of hyperthermia-induced apoptosis enhanced by docosahexaenoic acid: Implication for cancer therapy.* Chemico-Biological Interactions, 2014. **215**: p. 46-53.

136. Saniei, N., *Hyperthermia and Cancer Treatment.* Heat Transfer Engineering, 2009. **30**(12): p. 915-917.

137. Sawdon, A., E. Weydemeyer, and C.A. Peng, *Antitumor Therapy Using Nanomaterial-Mediated Thermolysis.* Journal of Biomedical Nanotechnology, 2014. **10**(9): p. 1894-1917.

138. Dennis, C.L., et al., *Nearly complete regression of tumors via collective behavior of magnetic nanoparticles in hyperthermia.* Nanotechnology, 2009. **20**(39): p. 395103.

139. Song, X., et al., *Ultra-Small Iron Oxide Doped Polypyrrole Nanoparticles for In Vivo Multimodal Imaging Guided Photothermal Therapy.* Advanced Functional Materials, 2014. **24**(9): p. 1194-1201.

140. Huang, P., et al., *Photosensitizer-conjugated silica-coated gold nanoclusters for fluorescence imaging-guided photodynamic therapy.* Biomaterials, 2013. **34**(19): p. 4643-4654.

141. Lee, J., et al., *Gold nanoparticles in breast cancer treatment: Promise and potential pitfalls.* Cancer Letters, 2014. **347**(1): p. 46-53.

142. Loo, C., et al., *Immunotargeted Nanoshells for Integrated Cancer Imaging and Therapy.* Nano Letters, 2005. **5**(4): p. 709-711.

143. Kirui, D.K., et al., *Targeted near-IR hybrid magnetic nanoparticles for in vivo cancer therapy and imaging.* Nanomedicine: Nanotechnology, Biology and Medicine, 2013. **9**(5): p. 702-711.

144. Gibson, J.D., B.P. Khanal, and E.R. Zubarev, *Paclitaxel-functionalized gold nanoparticles.* J Am Chem Soc, 2007. **129**(37): p. 11653-61.

145. Ding, Y., et al., *The performance of thiol-terminated PEG-paclitaxel-conjugated gold nanoparticles.* Biomaterials, 2013. **34**(38): p. 10217-10227.

146. Sun, C., et al., *Tumor-targeted drug delivery and MRI contrast enhancement by chlorotoxin-conjugated iron oxide nanoparticles.* Nanomedicine (London, England), 2008. **3**(4): p. 495-505.

147. Wang, F., et al., *Doxorubicin-tethered responsive gold nanoparticles facilitate intracellular drug delivery for overcoming multidrug resistance in cancer cells.* ACS Nano, 2011. **5**(5): p. 3679-3692.

148. Venkatesan, R., et al., *Doxorubicin conjugated gold nanorods: a sustained drug delivery carrier for improved anticancer therapy.* Journal of Materials Chemistry B, 2013. **1**(7): p. 1010-1018.

149. Patra, C.R., et al., *Fabrication of gold nanoparticles for targeted therapy in pancreatic cancer.* Advanced Drug Delivery Reviews, 2010. **62**(3): p. 346-361.

150. Laurent, S. and M. Mahmoudi, *Superparamagnetic iron oxide nanoparticles: promises for diagnosis and treatment of cancer.* International journal of molecular epidemiology and genetics, 2011. **2**(4): p. 367-390.

151. Kapse-Mistry, S., et al., *Nanodrug delivery in reversing multidrug resistance in cancer cells.* Front Pharmacol, 2014. **5**: p. 159.

152. Starkewolf, Z.B., et al., *X-ray triggered release of doxorubicin from nanoparticle drug carriers for cancer therapy.* Chemical communications (Cambridge, England), 2013. **49**(25): p. 2545-2547.

153. Madhusudhan, A., et al., *Efficient pH dependent drug delivery to target cancer cells by gold nanoparticles capped with carboxymethyl chitosan.* International journal of molecular sciences, 2014. **15**(5): p. 8216-8234.

154. Derfus, A.M., et al., *Remotely Triggered Release from Magnetic Nanoparticles.* Advanced Materials, 2007. **19**(22): p. 3932-3936.

155. Zhang, X.-D., et al., *Size-dependent radiosensitization of PEG-coated gold nanoparticles for cancer radiation therapy.* Biomaterials, 2012. **33**(27): p. 6408-6419.

156. Dani, R.K., C. Schumann, and O. Taratula, *Temperature-tunable iron oxide nanoparticles for remote-controlled drug release.* AAPS PharmSciTech, 2014. **15**(4): p. 963-972.

157. Bisker, G., et al., *Controlled release of Rituximab from gold nanoparticles for phototherapy of malignant cells.* J Control Release, 2012. **162**(2): p. 303-9.

158. Dilnawaz, F., et al., *Dual drug loaded superparamagnetic iron oxide nanoparticles for targeted cancer therapy.* Biomaterials, 2010. **31**(13): p. 3694-3706.

159. Zolata, H., F. Abbasi Davani, and H. Afarideh, *Synthesis, characterization and theranostic evaluation of Indium-111 labeled multifunctional superparamagnetic iron oxide nanoparticles.* Nuclear Medicine and Biology, 2015. **42**(2): p. 164-170.

160. Rehm, B.H.A., *Polyester synthases: natural catalysts for plastics.* Biochemical Journal, 2003. **376**: p. 15-33.

161. Chang, S.S., O'Keefe, Denise S., Bacich Dean J., et. al., *Prostate-specifc Membrane Antigen Is Produced in Tumo-associated Neovasculature.* Clinical Cancer Research, 1999. **5**: p. 2674-2681.

162. Chang, S.S., *Five different anti-prostate-specific membrane antigen (psma) antibodies confirm psma expression in tumor-associated neovasculature.* Cancer Research, 1999. **59**: p. 3192-3198.

163. Pinto, J.T., Suffoletto, Brian P., Berzin, Tyler M. et al., *Prostate-specific membrane antigen: a novel folate hydrolase in Human Prostatic Carcinoma Cells.* Clinical Cancer Research, 1996. **2**: p. 1445-1451.

164. Yao, V., Bacich, Dean J., *Prostate Specific Membrane Antigen (PSMA) Expression Gives Prostate Cancer Cells a Growth Advantage in a Physiologically Relevant Folate Environment InVitro.* The Prostate, 2006. **66**: p. 867-875.

165. Milowsky, M.I., Nanus, David M., Kostakoglu, Lale, Sheehan, Christine E., Vallabhajosula, Shankar, Goldsmith, Stanley J., Ross, Jeffrey S., and Bander, Neil H., *Vascular Targeted Therapy With Anti–Prostate Specific Membrane Antigen Monoclonal Antibody J591 in Advanced Solid Tumors.* Journal of Clinical Oncology, 2007. **25**(5): p. 540-547.

166. Haffner, M.C.M., Kronberger, Irmgard E. MD, Ross, Jeffery S. MD, Sheehan, Christine E. MD, Zitt, Matthias MD, Muhlmann, Gilbert MD, Ofner, Dietmar MD, Zelger, Bettina MD, Ensnger, Christian MD, Yang, Ximing J. MD, Geley, Stephan MD, Margreiter, Raimund MD, and Bander, Neil H. MD *Prostate-specific membrane antigen expression in the nevasculature of gastric and colorectal cancers.* Human Pathology, 2009. **40**: p. 1754-1761.

167. Liu, H., Moy, Peggy, Kim, Sae, Xi, Yan, Rajasekaran, Ayyappan, Navarro, Vincent, and Bander, H. Neil, *Monoclonal Antibodies to the Extracellular Domain of Prostate-specific Membrane Antigen Also React with Tumor Vascular Endothelium.* Cancer Research, 1997: p. 3629-3634.

168. Silver, D.A., et al., *Prostate-specific membrane antigen expression in normal and malignant human tissues.* Clinical Cancer Research, 1997. **3**: p. 81-85.

169. Stevens, J., Croix, St. Brad, *Tumor Endothelial Markers*, in *Angiogenesis*, W.D. Figg, Folkman, Judah, Editor. 2008, Springer: New York. p. 333-342.

170. Yoa, V., Bacich, Dean J., *Prostate SpecificMembraneAntigen (PSMA) Expression Gives Prostate Cancer Cells a Growth Advantage in a Physiologically Relevant Folate Environment In Vitro.* The Prostate, 2006. **66**: p. 867-875.

171. Horoszewicz JS, K.E., Murphy GP., *Monoclonal antibodies to a new antigenic marker in epithelial prostatic cells and serum of prostatic cancer patients.* Anticancer Research, 1987. **7**(5B): p. 927-35.

172. Smith-Jones, P.M., Vallabahajosula, Shankar, Goldsmith, J Stanley, et al., *In vitro characterization of radiolabeled monoclonal antibodies specific for the extracellular domain of prostate-specific membrane antigen.* Cancer Research, 2000. **60**: p. 5237-5243.

173. Gong, M.C., Chang, Sam S., Sadelain, Michel, Bander, Neil H., and Heston, Warren D. W. , *Prostate-specific membrane antigen (PSMA)-specific monoclonal antibodies in the treatment of prostate and other cancers.* Cancer and Metastasis Reviews, 1999. **18**: p. 483-490.

174. Bander, N.H., Nanus, D.M., Milowsky, M.I., Kostakoglu, L., Vallabhajosula, S., Goldsmith, S.J., *Targeted Systemic Therapy of Prostate Cancer with a Monoclonal Antibody to Prostate-Specific Membrane Antigen.* Seminars in Oncology, 2003. **30**(5): p. 667-677.

175. Christiansen, J.J.R., S.A.; Inge, L.; Cheng, L.; Anilkumar, G.; Bander, N. Rajasekaran, A.K., *N-glycosylation and microtubule integrity are involved in*

apical targeting of prostate-specific membrane antigen: implications for immunotherapy. Molecular Cancer Therapeutics, 2005. **4**: p. 704-714.

176. Morris, M.J., Divgi, C.R., Taskar, N.P., Batraki, M., Warren, N., Nacca, A., Smith-Jones, P., Schwartz, L., Kelly, W.K., Slovin, S., Solit, D., Halpern, J., Delacruz, A., Curley, T., Finn, R., O'Donoghue, J.A., Livingston P., Larson, S., Scher, H.I., *Pilot Trial of Unlabeled and Indium-111-Labeled Anti-Prostate-Specific Membrane Antigen Antibody J591 for Castrate Metastatic Prostate Cancer.* Clinical Cancer Research, 2005. **11**(20).

177. Bander, N.H., Trabulsi, E.J., Kostakoglu, L., *Targeting Metastatic Prostate Cancer With Radiolabeled Monoclonal Antibody J591 to the Extracellular Domain of Prostate Specific Membrane Antigen.* The Journal of Urology, 2003. **170**(5): p. 1717-1721.

178. Bander, N.H., Milowsky, Matthew I., Nanus, David M., Kostakoglu, Lale, Vallabhajosula, Shankar, and Goldsmith, Stanley J., *Phase I Trial of 177Lutetium-Labeled J591, a Monoclonal Antibody to Prostate-Specific Membrane Antigen, in Patients With Androgen-Independent Prostate Cancer* Journal of Clinical Oncology, 2005. **23**(21): p. 4591-4601.

179. Kraaij, R., van Rijswijk, A.L.C.T., Oomen, M.H.A., Haisma, H.J., and Bangma, C.H., *Prostate Specific Membrane Antigen (PSMA) Is a Tissue-Specific Target for Adenoviral Transduction of Prostate Cancer In Vitro.* The Prostate, 2005. **62**: p. 253-259.

180. Liu, C., Hasegawa, Kosei, Russell, Stephen J., Sadelain, Michel, Peng, Kah-Whye *Prostate-specific Membrane Antigen Retargeted Measles Virotherapy for the Treatment of Prostate Cancer.* The Prostate, 2009. **69**(19): p. 1128-1141.

181. Stubbe, J.a.T., Jiamin, *Polyhydroxyalkanoate (PHA) homeostasis: the role of PHA synthase.* National Product Reports, 2003. **20**: p. 445-457.

182. Lee, S.Y., *Review Bacterial Polyhydroxyalkanoates.* Biotechnology and Engineering, 1995. **49**: p. 1-14.

183. Steinbüchel, A., in *Biomaterials: novel materials from biological sources*, D. Byrom, Editor. 1991, Palgrave Macmillan Limited. p. 123.

184. Shishatskaya, E.I., et al. , *Biocompatibility of polyhydroxybutyrate microspheres: in vitro and in vivo evaluation.* Journal of Material Science: Materials in Medicine, 2008. **19**: p. 2493-2502.

185. Chena, G.-Q., Wu, Qiong *The application of polyhydroxyalkanoates as tissue engineering materials.* Biomaterials, 2005. **26**: p. 6565-6578.

186. Kassab, A.C., Piskin, E., Bilgiç, S., Denkbas, E. B., and Xu, K., *Embolization with Polyhydroxybutyrate (PHB) Microspheres: In-Vivo Studies.* Journal of Bioactive and Compatible Polymers, 1999. **14**: p. 291-303.

187. Freier, T., Kunze, G, Nischan, C, Kramer, S, Sternberg, K, SaX, M, Hopt, U. T., Schmitz, KP., *In vitro and in vivo degradation studies for development of a biodegradable patch based on poly(3-hydroxybutyrate).* Biomaterials, 2002. **23**: p. 2649-2657.

188. Verlinden, R.A.J., et al., *Bacterial synthesis of biodegradable polyhydroxyalkanoates.* Journal of Applied Microbiology, 2007. **107**: p. 1437-1449.

189. Mittendorf, V., et al. , *Synthesis of medium-chain-length polhydroxyalkanoates in Arabidopsis thaliana using intermediates of peroxisomal fatty acid β-oxidation.* Proceedings of National Academy if Science, 1998. **95**: p. 13397-13402.

190. Peter, V., Becher, Dorit, and Rehm, Bernd H.A. , *The inherent property of polyhydroxyalkanoate synthase to form spherical PHA granules at the cell poles: The core region is required for polar localization.* Journal of Biotechnology, 2007. **132**(238-245).

191. Song, J.J., et al., *In vitro polymerization and copolymerization of 3-hydroxypropionyl-CoA with the PHB synthanse from rastonia eutropha.* Biomacromolecules, 2000. **1**(3): p. 433-439.

192. Kim, Y.P., H.; Ober, C. K.; Coates, G. W.; Batt, C. A., *Enzymatic surface-initiated polymerization: A novel approach for the in situ solid-phase synthesis of biocompatible polymer poly(3-hydroxybutyrate).* Biomacromolecules, 2004. **5**: p. 889-894.

193. Niamsiri, N., Bergkvist, Magnus, Delamarre, Soazig C., Cady, Nathan C., Coates, Geoffrey W., Ober, Christopher K., and Batt, Carl A., *Insight in the role of bovine serum albumin for promoting the in situ surface growth of polyhydroxybutyrate (PHB) on patterned surfaces via enzymatic surface-initiated polymerization.* Colloids and Surfaces B: Biointerfaces, 2007. **60**: p. 68-79.

194. Jossek, R., et al. , *In vitro biosynthesis of poly(3-hydroxybutyric acid) by using purified poly(hydroxyalkanoic acid) synthase of Chromatium vinosum.* Applied Microbiology Biotechnology, 1998. **49**: p. 258-266.

195. Chan, A.C., P.J., Carter, *Therapeutic antibodies for autoimmunity and inflammation.* Nat Rev Immunol, 2010. **10**(5): p. 301-316.

196. Bander, N.H., D.M. Nanus, M.I. Milowsky, L. Kostakoglu, S. Vallabhajosula, S.J.Goldsmith, *Targeted Systemic Therapy of Prostate Cancer with a Monoclonal Antibody to Prostate-Specific Membrane Antigen.* Semin Oncol, 2003. **30**(5): p. 667-677.

197. Morris, M.J., et al., *Pilot Trial of Unlabeled and Indium-111-Labeled Anti-Prostate-Specific Membrane Antigen Antibody J591 for Castrate Metastatic Prostate Cancer.* Clin Cancer Res, 2005. **11**(20).

198. Christiansen, J.J., S.A. Rajasekaran, L. Inge, L. Cheng, G. Anilkumar, N.H. Bander, A.K. Rajasekaran, *N-glycosylation and microtubule integrity are involved in apical targeting of prostate-specific membrane antigen: implications for immunotherapy.* Mol Cancer Ther, 2005. **4**: p. 704-714.

199. Silver, D.A., et al., *Prostate-specific membrane antigen expression in normal and malignant human tissues.* Clin Cancer Res, 1997. **3**: p. 81-85.

200. Kularatne, S.A., et al., *Prostate-specific membrane antigen targeted imaging and therapy of prostate cancer using a psma inhibitor as a homing ligand.* Mol Pharm, 2009. **6**(3): p. 780-789.

201. Milowsky, M.I., D. Nanus, L. Kostakoglu, C. E. Sheehan, S. Vallabhajosula, Shankar, S. J. Goldsmith, J. S. Ross , N. H.Bander, *Vascular Targeted Therapy*

With Anti–Prostate Specific Membrane Antigen Monoclonal Antibody J591 in Advanced Solid Tumors. J Clin Oncol, 2007. **25**(5): p. 540-547.

202. Haffner, M.C., et al., *Prostate-specific membrane antigen expression in the nevasculature of gastric and colorectal cancers.* Hum Pathol, 2009. **40**: p. 1754-1761.

203. Chang, S.S., *Five different anti-prostate-specific membrane antigen (psma) antibodies confirm psma expression in tumor-associated neovasculature.* Cancer Res, 1999. **59**: p. 3192-3198.

204. Liu, H., P. Moy,S. Kim, Sae,Y. Xi, A. Rajasekaran, V. Navarro, and N. H. Bander, *Monoclonal Antibodies to the Extracellular Domain of Prostate-specific Membrane Antigen Also React with Tumor Vascular Endothelium.* Cancer Res, 1997: p. 3629-3634.

205. Kraaij, R., A. L. van Rijswijk, M. H. A. Oomen, H. J. Haisma, C. H. Bangma, *Prostate Specific Membrane Antigen (PSMA) Is a Tissue-Specific Target for Adenoviral Transduction of Prostate Cancer In Vitro.* Prostate, 2005. **62**: p. 253-259.

206. Liu, C., K. Hasegawa, S. J. Russell, M. Sadelain, K. Peng, *Prostate-specific Membrane Antigen Retargeted Measles Virotherapy for the Treatment of Prostate Cancer.* Prostate, 2009. **69**(19): p. 1128-1141.

207. Bander, N.H., E.J. Trabulsi, L. Kostakoglu, *Targeting Metastatic Prostate Cancer With Radiolabeled Monoclonal Antibody J591 to the Extracellular Domain of Prostate Specific Membrane Antigen.* J Urol, 2003. **170**(5): p. 1717-1721.

208. Bander, N.H., M.I. Milowsky, D.M. Nanus, L. Kostakoglu, S. Vallabhajosula, S.J. Goldsmith, *Phase I Trial of 177Lutetium-Labeled J591, a Monoclonal Antibody to Prostate-Specific Membrane Antigen, in Patients With Androgen-Independent Prostate Cancer.* J Clin Oncol, 2005. **23**(21): p. 4591-4601.

209. Saerens, D., G. H. Ghassabeh, S. Muyldermans, *Single-domain antibodies as building blocks for novel therapeutics.* Curr Opin Pharmacol, 2008. **8**: p. 600-608.

210. Ahmad, Z.A., et. al., *scFv Antibody: Principles and Clinical Application.* Clin Dev Immunol, 2012.

211. Ritter, G., L. S. Cohen, C. Williams, E. Richards, L. J. Old, S. Welt, *Serological analysis of human anti-human antibody responses in colon cancer patients treated with repeated doses of humanized monoclonal antibody A33.* Cancer Res, 2001. **61**: p. 6851-6859.

212. Brischwein, K., et al., *MT110: a novel bispecific single-chain antibody construct with high efficacy in eradicating established tumors.* Mol Immunol, 2006. **43**: p. 1129-1143.

213. Wolf, E., R. Hofmeister, P. Kufer, B. Schlereth, P.A. Baeuerle, *BiTEs: bispecific antibody constructs with unique anti-tumor activity.* Drug Discov Today, 2005. **10**: p. 1237-1244.

214. Weiner, L.M., R. Surana, S. Wang, *Monoclonal antibodies: versatile platforms for cancer immontherapy.* Nat Rev Immunol, 2010. **10**: p. 301-316.

215. Powers, D.B., P. Amersdorfer, M. Poul, U.B. Nielsen, M.R. Shalaby, G.P. Adams, L.M. Weiner, J.D. Marks, *Expression of single chain Fv-Fc fusions in Pichia pastoris* J Immunol Methods, 2001. **251**: p. 123-135.

216. Begent, R.H., M.J. Verhaar, K.A. Chester, J.L. Casey, A.J. Green, M.P. Napier, L.D. Hope-Stone, N. Cushen, P.A. Keep, C.J. Johnson, R.E. Hawkins, A.J. Hilson, L Robson, *Clinical evidence of effcient tumor targeting based on single-chain Fv antibody selected from a combinatorial library.* Nat Med, 1996. **2**: p. 979-984.

217. Kaiermo, K.J.A., *Radioimmunotherapy of solid cancers.* Acta Oncol, 1996. **35**: p. 343-355.

218. Lin-Cereghino, J., W.W. Wong, S. Xiong, W. Giang, L.T. Luong, J. Vu, S.D. Johnson, G.P. Lin-Cereghino, *Condensed protocol for competent cell preparation and transformation of the methylotrophic yeast Pichia pastoris.* BioTechniques 2005. **38**: p. 44-48.

219. Rader, C., G. Ritter, S. Nathan, M. Elia, I. Gout, A.A. Jungbluth, L.S. Cohen, S. Welt, L.J. Old, C.F. Barbas, *The rabbit antibody repertoire as a novel source for the generation of therapeutic human antibodies.* J Biol Chem, 2000. **275**: p. 13668–13676.

220. Damasceno, L., et al., *An optimized fermentation process for high-level production of a single-chain Fv antibody fragment in Pichia pastoris.* Protein Expr Purif, 2004. **37**: p. 18 - 26.

221. Brady, C.P., R.L. Shimp, A.P. Miles, M. Whitmore, A.W. Stowers *High-level production and puriWcation of P30P2MSP119, an important vaccine antigen for malaria, expressed in the methylotropic yeast Pichia pastoris.* Protein Expr Purif, 2001. **23**: p. 468-475.

222. auley-Patrick, S., M.L. Fazenda, B. McNeil, L.M. Harvey, *Heterologous protein production using the Pichia pastoris expression system.* Yeast, 2005. **22**: p. 249-270.

223. Jahic, M., J. Knoblechner, T. Charoenrat, S.O. Enfors, A. Veide, *Interfacing Pichia pastoris cultivation with expanded bed adsorption.* Biotechnol Bioeng, 2006. **93**: p. 1040-1049.

224. Sreekrishna, K., R.G. Brankamp, K.E. Kropp, D.T. Blankenship, J.T. Tsay, P.L. Smith, J.D. Wierschke, A. Subramaniam, L.A. Birkenberger, *Strategies for optimal synthesis and secretion of heterologous proteins in the methylotrophic yeast Pichia pastoris.* Gene, 1997. **190**: p. 55-62.

225. Hu, S., J. Qiao, Y. Guo, L. Cheng, J. Liu, *Codon optimization, expression, and characterization of an internalizing anti-ErbB2 single-chain antibody in Pichia pastoris.* Protein Expr Purif, 2005. **47**(1): p. 249-257.

226. Sinclair, G., F.Y.M. Choy, *Synonymous codon usage bias and the expression of human glucocerebrosidase in the methylotrophic yeast Pichia pastoris.* Protein Expr Purif, 2002. **26**: p. 96-105.

227. Fuhrmann, M., A. Hausherr, L. Ferbitz, T. Schödl, M. Heitzer, P. Hegemann, *Monitoring dynamic expression of nuclear genes in Chlamydomonas reinhardtii by using a synthetic luciferase reporter gene.* Plant Mol Bio, 2004. **55**(6): p. 869-81.

228. Griffiths, J.R., *A more general definition of Km [proceedings]*. Biochem Soc Trans, 1978. **6**(1): p. 258-60.

229. Straus, O.H., A. Goldstein, and L.P. With the Technical Assistance of Frank, *ZONE BEHAVIOR OF ENZYMES : ILLUSTRATED BY THE EFFECT OF DISSOCIATION CONSTANT AND DILUTION ON THE SYSTEM CHOLINESTERASE-PHYSOSTIGMINE.* The Journal of General Physiology, 1943. **26**(6): p. 559-585.

230. Thorpe, P.E., *Vascular Targeting Agents as Cancer Therapeutics.* Clinical Cancer Research, 2004. **10**: p. 415-427.

231. Hajitou, A., Pasqualini, Renata, and Arap, Wadih, *Vascular targeting: recent advances and therapeutic perspectives.* Trends Cardiovascular Medicine, 2006. **16**(3): p. 80-88.

232. Neri, D., Bicknell, Roy, *Tumor Vascular Targeting.* Nature Reviews, 2005. **5**: p. 436-446.

233. Hoffmann, R.T., Paprottka, P, Jakobs, T.F, Trumm, C. G., Reiser, M. F., *Arterial therapies of non-colorectal cancer metastases to the liver (from chemoembolization to radioembolization).* Abdominal Imaging, 2011. **36**: p. 671-676.

234. Lepor, H., *Vascular Targeted Photodynamic Therapy for Localized Prostate Cancer.* MedReviews, 2008. **10**(4): p. 254-261.

235. Peoples, O.P. and A.J. Sinskey, *Poly-beta-hydroxybutyrate (PHB) biosynthesis in Alcaligenes eutrophus H16. Identification and characterization of the PHB polymerase gene (phbC).* J Biol Chem, 1989. **264**(26): p. 15298-303.

236. Daly, R. and M.T. Hearn, *Expression of heterologous proteins in Pichia pastoris: a useful experimental tool in protein engineering and production.* J Mol Recognit, 2005. **18**(2): p. 119-38.

237. Cregg, J.M., *Distinctions Between Pichia pastoris and Other Expression Systems Introduction*, in *Pichia Protocols, Second Edition*, J.M. Cregg, Editor. 2007, Humana Press Inc, 999 Riverview Dr, Ste 208, Totowa, Nj 07512-1165 USA. p. 1-10.

238. Yu, Y., et al., *High-yield production of the human lysozyme by Pichia pastoris SMD1168 using response surface methodology and high-cell-density fermentation.* Electronic Journal of Biotechnology, 2014. **17**(6): p. 311-316.

239. Yang, Y.F., et al., *Efficient Expression, Purification, and Characterization of a Novel FAD-Dependent Glucose Dehydrogenase from Aspergillus terreus in Pichia pastoris.* Journal of Microbiology and Biotechnology, 2014. **24**(11): p. 1516-1524.

240. Neves, A., Brindle, K. M. , *A Paramagnetic Nanoprobe to Detect Tumor Cell Death Using Magnetic Resonance Imaging.* J. Am. Chem. Soc., 2007. **7**: p. 1419-1423.

241. Mornet, S., Vasseur, S. and Duguet, E. , *Magnetic nanopaticle for medical diagnosis and therapy.* J. Materials Chem, 2004: p. 2161-2175.

242. Lin-Cereghino, J., Wong, William W., Xiong, See, Giang, William, Luong, Linda T., Vu, Jane, Johnson, Sabrina D., Lin-Cereghino, Geoff P., *Condensed protocol for competent cell preparation and transformation of the methylotrophic yeast Pichia pastoris.* BioTechniques, 2005. **38**: p. 44-48.

243. Simon, E.J. and D. Shemin, *THE PREPARATION OF S-SUCCINYL COENZYME-A.* Journal of the American Chemical Society, 1953. **75**(10): p. 2520-2520.

244. Song, J.J., et al., *In vitro polymerization and copolymerization of 3-hydroxypropionyl-CoA with the PHB synthase from Ralstonia eutropha.* Biomacromolecules, 2000. **1**(3): p. 433-439.

245. Kim, Y.R., et al., *Real-time analysis of enzymatic surface-initiated polymerization using surface plasmon resonance (SPR).* Macromolecular Bioscience, 2006. **6**(2): p. 145-152.

246. Yan, L., et al., *Formation and Reaction of Interchain Carboxylic Anhydride Groups on Self-Assembled Monolayers on Gold.* Langmuir, 1997. **13**(25): p. 6704-6712.

247. Sun, S., Zeng, H., *Size-controlled Synthesis of Magnetite Nanoparticles.* J Am Chem Soc, 2002. **124**: p. 8204-8205.

248. Rey, D.A., Strickland, Aaron D, Kirui, Dickson, Niamsiri, Nuttawee, and Batt, Carl A., *In vitro self-assembly of gold nanoparticle-coated poly(3-hydroxybutyrate) granules exhibiting plasmon-induced thermo-optical enhancements.* ACS applied materials interfaces, 2010. **2**(7): p. 1804-1810.

249. Nelson, M.D., Fitch, David H. A., *Overlap extension PCR: an efficient method for transgene construction.* Molecular Methods For Evolutionary Genetics 2011. **772**(6): p. 459-470.

250. Ho, S.N., el. al., *Site-Directed mutagenesis by overlap extension using the polymerase chain reaction.* Gene, 1989. **77**: p. 51-59.

251. Grage, K. and B.H.A. Rehm, *In Vivo Production of scFv-Displaying Biopolymer Beads Using a Self-Assembly-Promoting Fusion Partner.* Bioconjugate Chemistry, 2007. **19**(1): p. 254-262.

252. Hu, S., Li, Liangwei, Qiao, Jingjuan, Guo, Yujie, Cheng, Liansheng, Lui, Jing *Codon optimization, expression, and characterization of an internalizing anti-ErbB2 single-chain antibody in Pichia pastoris.* 2005. **47**(1): p. 249-257.

253. Huston, J.S., et al., *Protein engineering of antibody binding sites: recovery of specific activity in an anti-digoxin single-chain Fv analogue produced in Escherichia coli.* Proceedings of the National Academy of Sciences of the United States of America, 1988. **85**(16): p. 5879-5883.

254. Todorovska, A., et al., *Design and application of diabodies, triabodies and tetrabodies for cancer targeting.* Journal of Immunological Methods, 2001. **248**(1–2): p. 47-66.

255. Wen, D., et al., *Discovery and investigation of O-xylosylation in engineered proteins containing a (GGGGS)n linker.* Anal Chem, 2013. **85**(9): p. 4805-12.

256. Feng, Y., R. Gong, and D.S. Dimitrov, *Design, expression and characterization of a soluble single-chain functional human neonatal Fc receptor.* Protein Expression and Purification, 2011. **79**(1): p. 66-71.

257. Trinh, R., et al., *Optimization of codon pair use within the (GGGGS)3 linker sequence results in enhanced protein expression.* Molecular Immunology, 2004. **40**(10): p. 717-722.

258. Argos, P., *An investigation of oligopeptides linking domains in protein tertiary structures and possible candidates for general gene fusion.* Journal of Molecular Biology, 1990. **211**(4): p. 943-958.

259. Mack, M., G. Riethmuller, and P. Kufer, *A small bispecific antibody construct expressed as a functional single-chain molecule with high tumor cell cytotoxicity.* Proc Natl Acad Sci U S A, 1995. **92**(15): p. 7021-5.

260. Lum, L.G. and A. Thakur, *Targeting T Cells with Bispecific Antibodies for Cancer Therapy.* BioDrugs : clinical immunotherapeutics, biopharmaceuticals and gene therapy, 2011. **25**(6): p. 365-379.

261. Kwon, H.S., et al., *A multi-functional polyhydroxybutyrate nanoparticle for theranostic applications.* Journal of Materials Chemistry B, 2014. **2**(25): p. 3965-3971.

262. Fung, Y.C., *Biomechanic: Circulation*. 2nd ed. 1997, Springer, New York.

263. McDonald, J.C., et al., *Fabrication of microfluidic systems in poly(dimethylsilloxane).* Electrophoresis, 2000. **21**: p. 27-40.

264. Myers, D.R., et al., *Endothelialized Microfluidics for Studying Microvascular Interactions in Hematologic Diseases.* 2012(64): p. e3958.

265. Chackerian, B., et al., *Determinants of autoantibody induction by conjugated papillomavirus virus-like particles.* J Immunol, 2002. **169**(11): p. 6120-6.

266. Cubas, R., et al., *Virus-like particle (VLP) Lymphatic Trafficking and Immune Response Generation after Immunization by Different Routes.* Journal of immunotherapy (Hagerstown, Md. : 1997), 2009. **32**(2): p. 118-128.

267. Michel, M.L. and P. Tiollais, *Hepatitis B vaccines: protective efficacy and therapeutic potential.* Pathol Biol (Paris), 2010. **58**(4): p. 288-95.

268. Frazer, I.H., *Prevention of cervical cancer through papillomavirus vaccination.* Nat Rev Immunol, 2004. **4**(1): p. 46-54.

269. Zhou, J., et al., *Expression of vaccinia recombinant HPV 16 L1 and L2 ORF proteins in epithelial cells is sufficient for assembly of HPV virion-like particles.* Virology, 1991. **185**(1): p. 251-7.

270. Rodriguez-Limas, W.A., K. Sekar, and K.E. Tyo, *Virus-like particles: the future of microbial factories and cell-free systems as platforms for vaccine development.* Curr Opin Biotechnol, 2013. **24**(6): p. 1089-93.

271. Li, K., et al., *Antigen incorporated in virus-like particles is delivered to specific dendritic cell subsets that induce an effective antitumor immune response in vivo.* J Immunother, 2013. **36**(1): p. 11-9.

272. Roldao, A., et al., *Virus-like particles in vaccine development.* Expert Rev Vaccines, 2010. **9**(10): p. 1149-76.

273. Villa, L.L., et al., *Immunologic responses following administration of a vaccine targeting human papillomavirus Types 6, 11, 16, and 18.* Vaccine, 2006. **24**(27-28): p. 5571-83.

274. Al-Barwani, F., et al., *Mannosylation of Virus-Like Particles Enhances Internalization by Antigen Presenting Cells.* PLoS ONE, 2014. **9**(8): p. e104523.

275. McKee, S.J., et al., *Virus-like particles and alpha-galactosylceramide form a self-adjuvanting composite particle that elicits anti-tumor responses.* J Control Release, 2012. **159**(3): p. 338-45.

276. Middelberg, A.P., et al., *A microbial platform for rapid and low-cost virus-like particle and capsomere vaccines.* Vaccine, 2011. **29**(41): p. 7154-62.

277. Meehl, M.A. and T.A. Stadheim, *Biopharmaceutical discovery and production in yeast.* Current Opinion in Biotechnology, 2014. **30**(0): p. 120-127.

278. Macauley-Patrick, S., et al., *Heterologous protein production using the Pichia pastoris expression system.* Yeast, 2005. **22**(4): p. 249-70.

279. Lei, J., et al., *Expression, purification and characterization of recombinant human interleukin-2-serum albumin (rhIL-2-HSA) fusion protein in Pichia pastoris.* Protein Expression and Purification, 2012. **84**(1): p. 154-160.

280. Cereghino, G.P.L., et al., *Production of recombinant proteins in fermenter cultures of the yeast Pichia pastoris.* Current Opinion in Biotechnology, 2002. **13**(4): p. 329-332.

281. Damasceno, L.M., C.J. Huang, and C.A. Batt, *Protein secretion in Pichia pastoris and advances in protein production.* Appl Microbiol Biotechnol, 2012. **93**(1): p. 31-9.

282. Vogl, T., F.S. Hartner, and A. Glieder, *New opportunities by synthetic biology for biopharmaceutical production in Pichia pastoris.* Current Opinion in Biotechnology, 2013. **24**(6): p. 1094-1101.

283. Lin-Cereghino, G., et al., *The effect of alpha-mating factor secretion signal mutations on recombinant protein expression in Pichia pastoris.* Gene, 2013. **519**: p. 311 - 317.

284. Cereghino, J.L. and J.M. Cregg, *Heterologous protein expression in the methylotrophic yeast Pichia pastoris.* FEMS Microbiology Reviews, 2000. **24**(1): p. 45-66.

285. Heyland, J., et al., *Quantitative physiology of Pichia pastoris during glucose-limited high-cell density fed-batch cultivation for recombinant protein production.* Biotechnol Bioeng, 2010. **107**(2): p. 357-68.

286. Zhou, X., et al., *Production of LYZL6, a novel human c-type lysozyme, in recombinant Pichia pastoris employing high cell density fed-batch fermentation.* Journal of Bioscience and Bioengineering, 2014. **118**(4): p. 420-425.

287. Tome-Amat, J., et al., *Secreted production of assembled Norovirus virus-like particles from Pichia pastoris.* Microbial Cell Factories, 2014. **13**(1): p. 134.

288. Valmori, D., et al., *Vaccination with NY-ESO-1 protein and CpG in Montanide induces integrated antibody/Th1 responses and CD8 T cells through cross-priming.* Proc Natl Acad Sci U S A, 2007. **104**(21): p. 8947-52.

289. Sugita, Y., et al., *NY-ESO-1 expression and immunogenicity in malignant and benign breast tumors.* Cancer Res, 2004. **64**(6): p. 2199-204.

290. Long, Y.Y., et al., *Measurement of serum antibodies against NY-ESO-1 by ELISA: A guide for the treatment of specific immunotherapy for patients with advanced colorectal cancer.* Experimental and Therapeutic Medicine, 2014. **8**(4): p. 1279-1284.

291. Li, M., et al., *Effective inhibition of melanoma tumorigenesis and growth via a new complex vaccine based on NY-ESO-1-alum-polysaccharide-HH2.* Mol Cancer, 2014. **13**: p. 179.

292. Chen, J.-L., et al., *NY-ESO-1 specific antibody and cellular responses in melanoma patients primed with NY-ESO-1 protein in ISCOMATRIX and boosted with recombinant NY-ESO-1 fowlpox virus.* International Journal of Cancer, 2015. **136**(6): p. E590-E601.

293. Goldfeld, M., et al., *Advanced near-infrared monitor for stable real-time measurement and control of Pichia pastoris bioprocesses.* Biotechnology Progress, 2014. **30**(3): p. 749-759.

294. Kim, S., et al., *Real-time monitoring of glycerol and methanol to enhance antibody production in industrial Pichia pastoris bioprocesses.* Biochemical Engineering Journal, 2015. **94**(0): p. 115-124.

295. Clayton, D.A. and G.S. Shadel, *Purification of mitochondria by sucrose step density gradient centrifugation.* Cold Spring Harb Protoc, 2014. **2014**(10): p. pdb prot080028.

296. Pokorski, J.K., M.L. Hovlid, and M.G. Finn, *Cell Targeting with Hybrid Qβ Virus-Like Particles Displaying Epidermal Growth Factor.* Chembiochem : a European journal of chemical biology, 2011. **12**(16): p. 2441-2447.

297. Walker, J.M., *The proteomics protocols handbook*, 2005, Humana Press: Totowa, N.J. :.

298. Artimo, P., et al., *ExPASy: SIB bioinformatics resource portal.* Nucleic Acids Res, 2012. **40**(Web Server issue): p. W597-603.

299. Hong, F., N.Q. Meinander, and L.J. Jonsson, *Fermentation strategies for improved heterologous expression of laccase in Pichia pastoris.* Biotechnology and Bioengineering, 2002. **79**(4): p. 438-449.

300. Higgins, D.R. and J.M. Cregg, *Pichia protocols*, 1998, Humana Press: Totowa, N.J. :.

301. Izutsu, K., et al., *Near-infrared analysis of hydrogen-bonding in glass- and rubber-state amorphous saccharide solids.* AAPS PharmSciTech, 2009. **10**(2): p. 524-9.

302. Workman, J., *Practical guide to interpretive near-infrared spectroscopy*, L. Weyer, Editor 2008, CRC Press: Boca Raton :.

303. Stratton, J., V. Chiruvolu, and M. Meagher, *High cell-density fermentation.* Methods Mol Biol, 1998. **103**: p. 107-20.

304. Khatri, N.K. and F. Hoffmann, *Impact of methanol concentration on secreted protein production in oxygen-limited cultures of recombinant Pichia pastoris.* Biotechnology and Bioengineering, 2006. **93**(5): p. 871-879.

305. Guarna, M.M., et al., *On-line monitoring and control of methanol concentration in shake-flask cultures of Pichia pastoris.* Biotechnology and Bioengineering, 1997. **56**(3): p. 279-286.

306. Yurimoto, H., M. Oku, and Y. Sakai, *Yeast methylotrophy: metabolism, gene regulation and peroxisome homeostasis.* International journal of microbiology, 2011. **2011**: p. 101298-101298.

307. Jungo, C., I. Marison, and U. von Stockar, *Mixed feeds of glycerol and methanol can improve the performance of Pichia pastoris cultures: A quantitative study based on concentration gradients in transient continuous cultures.* Journal of Biotechnology, 2007. **128**(4): p. 824-837.

308. Hoseki, J., R. Ushioda, and K. Nagata, *Mechanism and components of endoplasmic reticulum-associated degradation.* J Biochem, 2010. **147**(1): p. 19-25.

309. Puxbaum, V., D. Mattanovich, and B. Gasser, *Quo vadis? The challenges of recombinant protein folding and secretion in Pichia pastoris.* Appl Microbiol Biotechnol, 2015. **99**(7): p. 2925-38.

310. Loewen, M.C., et al., *Biosynthetic production of type II fish antifreeze protein: fermentation by Pichia pastoris.* Applied Microbiology and Biotechnology, 1997. **48**(4): p. 480-486.

311. Zhang, W., et al., *Pichia pastoris fermentation with mixed-feeds of glycerol and methanol: growth kinetics and production improvement.* J Ind Microbiol Biotechnol, 2003. **30**(4): p. 210-5.

312. Minning, S., et al., *Optimization of the high-level production of Rhizopus oryzae lipase in Pichia pastoris.* Journal of Biotechnology, 2001. **86**(1): p. 59-70.

313. Li, P., et al., *Expression of recombinant proteins in Pichia pastoris.* Appl Biochem Biotechnol, 2007. **142**(2): p. 105-24.

314. Ramon, R., et al., *Improving the monitoring of methanol concentration during high cell density fermentation of Pichia pastoris.* Biotechnol Lett, 2004. **26**(18): p. 1447-52.

315. Fernandez, E., et al., *Conformational and Thermal Stability Improvements for the Large-Scale Production of Yeast-Derived Rabbit Hemorrhagic Disease Virus-Like Particles as Multipurpose Vaccine.* Plos One, 2013. **8**(2).